UNIVERSITEIT•STELLENBOSCH•UNIVERSITY
jou kennisvennoot • your knowledge partner

# An Investigation of Coupling Mechanisms in Narrowband Microwave Filters

by

Esti Mari Hansmann

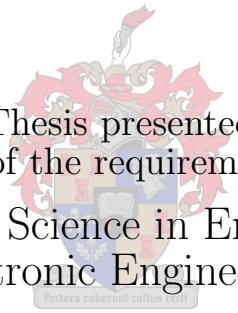

Thesis presented
in partial fulfilment of the requirements for the degree of

Master of Science in Engineering
(Electronic Engineering)

at the

University of Stellenbosch

Department of Electrical and Electronic Engineering,
University of Stellenbosch,
Private Bag X1, 7602 Matieland, South Africa.

Supervisor: Prof P Meyer

December 2008

# Declaration

I, the undersigned, hereby declare that the work contained in this thesis is my own original work and that I have not previously in its entirety or in part submitted it at any university for a degree.

Signature: .....
E M Hansmann

Date: .....

# Abstract

*Keywords* - Coaxial Coupled Diplexer, Inverter, Circuit Model, Coupling Coefficient, Post, Iris, Waveguide Filter

The design of an aperture-coupled coaxial diplexer for R-band, is presented. To improve the ease of tuning, a tuning procedure for the diplexer with the aid of a MATLAB application with graphical user interface, is developed. Final experimental results show good agreement between the circuit model and the physical structure. Final measurements of the diplexer structure achieved 18.83 dB and 21.52 dB return loss in the lower and upper frequency band respectively and insertion loss of 0.58 dB and 0.61 dB was measured for the two frequency bands. Isolation were measured as 74 dB at 2.01 GHz and 84 dB at 2.17 GHz

The accuracy of two techniques for determining coupling coefficients in coaxial and waveguide resonators are investigated. One method is the Eigenmode Method for determining the coupling coefficients in a physical resonator and the other the circuit model representation, utilising inverters to represent the coupling between resonators. Results showed that marked differences occur when using the three different inverter configurations to enable filter dimensioning for a given coupling coefficient.

Four waveguide filters, utilising posts and irises respectively, are designed using dimensions obtained from the three inverter configurations as well as the Eigenmode method for a certain coupling coefficient.

# Opsomming

*Sleutelwoorde* - Koaksiale Gekoppelde Diplekser, Omkeerder, Stroombaan Model, Koppelfaktor, Stafie, Iris, Golfleier Filter

Die ontwerp van 'n gleuf-gekoppelde koaksiale diplekser vir R-band word aangebied. Om die verstelling van die diplekser te vergemaklik, is 'n MATLAB verstellings aanwending met 'n grafiese gebruikers koppelvlak, ge-ontwerp. Die finale diplekser struktuur het weerkaatsings van onderskeidelik 18.83 dB en 21.52 dB vermag. Insetverliese van 0.58 dB en 0.61 dB is gemeet vir die twee frekwensie bande. Isolasie is gemeet as 74 dB by 2.01 GHz en 84 dB by 2.17 GHz.

Die akkuraatheid van twee tegnieke vir die bepaling van die koppelfaktor vir koaksiale en golfleier word bestudeer. Die een tegniek waarvan gebruik gemaak word is die Eiewaarde metode om die koppelfaktor tussen fisiese resoneerders te bepaal. Die tweede tegniek is om gebruik te maak van omkeerders in 'n stroombaan model om die koppeling tussen resoneerders voor te stel. Die resultate het duidelike verskille aangetoon in die gebruik van die drie omkeerder konfigurasies om afmetings vir 'n filter te bepaal vir 'n gegewe koppelfaktor.

Vier golfleier filters wat onderskeidelik gebruik maak van stafies en gleuwe, is ontwerp deur afmetings wat bepaal is deur die drie verskillende omkeerder konfigurasies en die Eiewaarde metode vir 'n voorafbepaalde koppelfaktor.

# Acknowledgement

I am indebted to Prof. Petrie Meyer for his patience, support and guidance. It was indeed a privilege to complete my masters study with him as my supervisor.

Dr. Wolhuter for financial support.

For the precise manufacturing of the diplexer, I would like to sincerely thank Wessel Croukamp and Lincoln Saunders. Without their attention to detail, my final diplexer measurements would not have been possible.

Thank you to my friends and E211A colleagues namely, Eugene, Dave, JP, John, Johan, Johan, Jonathan, Leroux, and Migael for your advice and interesting conversations.

A special thanks to John-Phillip and Riana for proofreading the thesis.

Thank you, to my family, for your loving support.

# Contents

**Declaration** i

**Abstract** iii

**Opsomming** iv

**Acknowledgement** v

**Contents** vi

**List of Figures** ix

**List of Tables** xii

**1 Introduction** 1
- 1.1 Historical Perspective . . . 1
- 1.2 About the Thesis . . . 2
- 1.3 Layout of Thesis . . . 3

**2 Circuit Model for a Narrowband Diplexer** 5
- 2.1 Introduction . . . 5
- 2.2 Narrowband Coupled Resonators . . . 5
- 2.3 Diplexer Synthesis . . . 8
  - 2.3.1 Specifications for Diplexer . . . 8
- 2.4 Concise Design Procedure for Circuit Element Model . . . 9
- 2.5 Detailed Design Procedure . . . 10
  - 2.5.1 Filter Type and Minimum Order . . . 10
  - 2.5.2 Design of Resonator . . . 12
  - 2.5.3 Determination of Capacitance for Resonance . . . 12
  - 2.5.4 Impedance and Admittance Inverters . . . 14
- 2.6 An Equivalent Circuit for Magnetically Coupled Coils . . . 18
- 2.7 k and q values . . . 19
  - 2.7.1 Calculation of an Admittance Inverter . . . 22
- 2.8 Unloaded Q of Resonator . . . 24

2.8.1 Resistor value for practical $Q_u$-values . . . 25
2.9 Final Diplexer Implementation . . . 26
2.10 Conclusion . . . 35

**3 Physical Realisation of a Coaxial Cavity Diplexer 36**
3.1 Introduction . . . 36
3.2 Diplexer Realisation Media . . . 37
3.3 Configurations Available for Implementation . . . 39
3.3.1 Interdigital Filter . . . 39
3.3.2 Combline Filter . . . 39
3.3.3 Coupled Coaxial Resonators . . . 40
3.4 Physical Implementation of Circuit Model . . . 41
3.5 Concise Design Procedure for Physical Dimensions of Diplexer . . . 42
3.5.1 Final Implementation of Diplexer . . . 43
3.6 Physical Dimensions of Resonators . . . 44
3.6.1 Resonator Dimensions . . . 44
3.6.2 Determining the Length of Resonator . . . 47
3.7 Unloaded Q of Resonator . . . 50
3.8 Input/Output Q-factors . . . 52
3.8.1 Group Delay . . . 52
3.8.2 Computing $Q_l$ from Group Delay . . . 52
3.9 Coupling Coefficients . . . 56
3.9.1 Eigenmode Method for Determining Coupling . . . 57
3.9.2 Physical Realisation of $k_{12}$, $k_{23}$ and $k_{34}$ for Filter . . . 58
3.9.3 Field Distribution in Resonators . . . 59
3.10 Diplexer Prototype . . . 63
3.10.1 Physical Realisation of Common Port Coupling for Diplexer . . . 63
3.11 Tuning Procedure of Diplexer . . . 64
3.11.1 Tuning by means of MWO and CST . . . 64
3.12 Final Diplexer Prototype . . . 69
3.13 Modification of Prototype for Manufacturing Purposes . . . 71
3.14 Measurement Procedure . . . 75
3.14.1 Measurement Configuration . . . 75
3.14.2 Results . . . 76
3.14.3 Graphical User Interface . . . 77
3.15 Conclusion . . . 81

**4 Coupling Mechanisms in Coaxial and Waveguide Filters 82**
4.1 Introduction . . . 82
4.2 Coaxial Implementation . . . 83
4.2.1 Design Procedure and Parameter Extraction . . . 85
4.2.2 Results . . . 85
4.3 Waveguide Implementation . . . 89

4.3.1 Concise Design Procedure For Comparison of Coupling Mechanism . . . 89
4.4 Inverter Topologies Under Consideration . . . 91
4.4.1 Frequency at which Coupling is Calculated . . . 91
4.4.2 Configuration 1 . . . 93
4.4.3 Configuration 2 . . . 96
4.4.4 Configuration 3 . . . 97
4.4.5 Computational Results . . . 98
4.5 Implementation of Coupling Mechanisms in a Filter . . . 102
4.5.1 Post . . . 104
4.5.2 Computational Results . . . 105
4.5.3 Iris . . . 107
4.5.4 Computational Results . . . 108
4.6 Conclusion . . . 110

**5 Conclusion 111**

**Bibliography 114**

**A Diplexer Tuning Procedure 117**
A.1 Tuning of Section 4 . . . 118
A.2 Tuning of Section 5 . . . 121
A.3 Tuning of Section 1 . . . 123
A.4 Tuning of Section 2 . . . 124
A.5 Tuning of Section 3 . . . 125
A.6 Tuning of Section 6 . . . 126
A.7 Tuning of Section 7 . . . 127
A.8 Tuning of Section 8 . . . 128
A.9 Final Tuned Diplexer . . . 129

**B Derivation of Equations for Configuration 3 130**

# List of Figures


2.1 A general two-port network composed of tuned coupled cavities . . . . 6
2.2 Block diagram of diplexer . . . . . 9
2.3 Fourth order filter response ($S_{21}$) . . . . . 10
2.4 Resonator consisting of a shunt capacitor, transmission line and resistor 12
2.5 $S_{21}$ and $S_{11}$ of a shunt resonator . . . . . 14
2.6 Input impedance and admittance of inverter and load . . . . . 15
2.7 Series topology for implementation of inverter . . . . . 16
2.8 Shunt topology for implementation of inverter . . . . . 17
2.9 Impedance and admittance inverters . . . . . 17
2.10 Equivalent circuit for magnetically coupled coils . . . . . 18
2.11 The T-equivalent circuit for the magnetically coupled coils . . . . . 18
2.12 Inductance $L_1$ grouped together with series resonator . . . . . 19
2.13 An ideal impedance inverter placed between series resonators . . . . . 19
2.14 Effect of different $Q_u$ on $S_{21}$ . . . . . 25
2.15 The input impedance versus frequency of a resonator . . . . . 26
2.16 Input reactance of filter 2 due to incoming signal in passband of filter 1 27
2.17 General topology of fourth order Chebyshev bandpass diplexer model . 28
2.18 Filter response of Filter 1 and 2 . . . . . 29
2.19 Schematic of Filter, centre frequency 1.995 GHz . . . . . 30
2.20 Schematic of Filter, centre frequency 2.185 GHz . . . . . 31
2.21 Schematic of Diplexer . . . . . 32
2.22 The S-parameters, $S_{21}$, $S_{31}$ and $S_{11}$, of the diplexer circuit model . . . . 35

3.1 Flowchart of available options for filter implementations. . . . . 37
3.2 Configuration of interdigital and combline filters in strip-line. . . . . 40
3.3 Coupled coaxial resonator . . . . . 40
3.4 Sectional front view of the diplexer as a combline configuration . . . . . 41
3.5 Resonator consisting of a shunt capacitor, transmission line and resistor 42
3.6 Top and front view of coaxial resonator . . . . . 45
3.7 Characteristic impedance as function of parameter $A$ . . . . . 45
3.8 Determining impedance of coaxial resonator . . . . . 46
3.9 Frequency response of mode 1 as a function of parameters $V$ and $H$ . . 49
3.10 Unloaded quality factor as a result of parameter $A$ . . . . . 50

3.11 Definition of parameters for CST model . . . 51
3.12 Unloaded quality factor as a function of parameter $L$ . . . 51
3.13 Dimensions for computing loaded quality factor . . . 54
3.14 Effect of parameter $D$ on the loaded quality factor . . . 55
3.15 Effect of parameter $L$ on the loaded quality . . . 55
3.16 Parameter definition for implementation of coupling coefficient . . . 56
3.17 Coupling coefficient as a function of parameter $T$ . . . 58
3.18 Coupling coefficient as a function of parameter $W$ . . . 59
3.19 Field distribution in two adjacent resonators . . . 60
3.20 Definition of curve location for field distribution . . . 61
3.21 The absolute value of the electric field, mode 1 on surface of iris . . . 61
3.22 Magnitude of the electric field distribution on iris . . . 62
3.23 The absolute value of the magnetic field, mode 1 on surface of iris . . . 62
3.24 Magnitude of the magnetic field distribution on iris . . . 63
3.25 Parameter definition of CST physical model . . . 65
3.26 Front and top view of diplexer, prototype one . . . 70
3.27 Top view of diplexer prototype 2 with roof and tuning screws removed . 71
3.28 Top view of diplexer prototype 2 . . . 73
3.29 Front section view of diplexer prototype 2 . . . 74
3.30 Measurement configuration . . . 75
3.31 Measured s-parameters of diplexer . . . 76
3.32 Measured s-parameters of diplexer . . . 77
3.33 Determining $Y_{total}$ for the centre sections of diplexer . . . 78
3.34 Screen shot of GUI application . . . 79
3.35 Screen shot from GUI application . . . 79
3.36 The final $S_{21}$ and $S_{11}$ . . . 80

4.1 Parameter definition for coaxial resonator in CST. . . . 84
4.2 MWO schematic of two coupled resonators in coaxial media. . . . 84
4.3 Coupling coefficient is proportional to the bandwidth . . . 87
4.4 Shunt discontinuities . . . 91
4.5 MWO schematic of *Configuration* 1 . . . 95
4.6 MWO schematic of *Configuration 2* . . . 96
4.7 MWO schematic of *Configuration* 3 . . . 98
4.8 Dimensions for a post in a waveguide . . . 99
4.9 Dimensions for an iris in a waveguide . . . 100
4.10 Comparison of coupling coefficients for a post . . . 101
4.11 Comparison of coupling coefficients for an iris . . . 101
4.12 Comparison of coupling coefficients for a post and iris . . . 103
4.13 Dimensions for CST model with post as coupling structure . . . 105
4.14 $S_{11}$ of rectangular waveguide filter with inductive post. . . . 106
4.15 $S_{21}$ of rectangular waveguide filter with inductive post. . . . 106
4.16 Dimensions for CST model with an iris as coupling structure . . . 107

4.17 $S_{11}$ of rectangular waveguide filter with an iris. . . . . 109
4.18 $S_{21}$ of rectangular waveguide filter with an iris. . . . . 109

A.1 Definition of the various designated sections . . . . . 117
A.2 Tuning of Section 4 . . . . . 118
A.3 Screenshots from MATLAB application . . . . . 119
A.4 Screenshots from MATLAB application . . . . . 120
A.5 Diplexer tuning of Section 5 . . . . . 122
A.6 Diplexer tuning of Section 1 . . . . . 123
A.7 Diplexer tuning of lower frequency band, part 2 . . . . . 124
A.8 Diplexer tuning of lower frequency band, part 3 . . . . . 125
A.9 Diplexer tuning of upper frequency band, part 6 . . . . . 126
A.10 Diplexer tuning of upper frequency band, part 7 . . . . . 127
A.11 Diplexer tuning of upper frequency band, part 8 . . . . . 128
A.12 Final tuning of diplexer . . . . . 129

B.1 Inverter model (*Configuration* 3) . . . . . 130

# List of Tables


2-I The desired frequency bands of the diplexer . . . . . 8
2-II Normalised k- and q values for a low-pass filter prototype . . . . . 21
2-III The final and tuned k and q values . . . . . 33
2-IV The final and tuned k and q values . . . . . 33
2-V The optimised loaded quality factor . . . . . 34
2-VI The optimised coupling coefficient . . . . . 34

3-I Characteristics of various filter realisation media . . . . . 38
3-II The optimised normalised loaded quality factor . . . . . 53
3-III The optimised normalised loaded quality factor . . . . . 53
3-IV The bandwidth transforming of the coupling coefficient . . . . . 58
3-V The 18 variables of the diplexer in the MWO- and CST model . . . . . 65
3-VI Result of parameter extraction on CST dimensions . . . . . 66
3-VII Centre sections of the CST model for the fine tuning of diplexer . . . . 67
3-VIII Sections of the CST model for the fine tuning of the diplexer . . . . . 68
3-IX Comparison of final optimised extracted parameters . . . . . 81

4-I Values of parameter $I$ and $W$ . . . . . 85
4-II Values of parameter $I$ and $W$ . . . . . 86
4-III Validation of coupling coefficients for changing height of iris . . . . . 88
4-IV Validation of coupling coefficients for changing width of iris . . . . . 88
4-V Inverter topologies under consideration . . . . . 92
4-VI The normalised k and q values for a third order Chebyshev filter . . . . 102
4-VII Dimensions computed for a post and an iris . . . . . 104
4-VIII Dimensions obtained for the post representation of inverter . . . . . 105
4-IX Dimensions obtained for the iris representation of inverter . . . . . 108

A-I Comparison of the final optimised extracted multipliers: Section 4 . . . 121
A-II Comparison of the final optimised extracted multipliers: Section 5 . . . 122
A-III Comparison of the final optimised extracted multipliers: Section 1 . . . 123
A-IV Comparison of the final optimised extracted multipliers: Section 2 . . . 124
A-V Comparison of the final optimised extracted multipliers: Section 3 . . . 125
A-VI Comparison of the final optimised extracted multipliers: Section 6 . . . 126

A-VII Comparison of the final optimised extracted multipliers: Section 7 . . . 127
A-VIIIComparison of the final optimised extracted multipliers: Section 8 . . . 128

# Chapter 1

# Introduction

## 1.1 Historical Perspective

The history of filter design and media used to implement microwave filters, span over a century of development. Progressing from the waveguide as a conceptual idea to the filters and multiplexers orbiting earth in modern communication satellites, the path of discovering filters is remarkable and contains interesting cases of multiple rediscoveries.

In 1897, Lord Raleigh showed for the first time that waves could propagate within hollow conducting cylinders [1]. He concluded that there is a lower frequency limit that must be exceeded to allow wave propagation in a waveguide. This lower limit is determined by the cross-sectional dimensions of the cylinder as well as the mode number of the propagating wave [1]. In 1902, R. H. Weber proposed a physical interpretation for as to why the wave velocity of the wave is lower than the velocity of light in a waveguide medium. He contributed this effect to a plane wave travelling in a zig-zag path as it is reflected from the walls of the tube [1]. After this, waveguides seemed to disappear from technical literature for the next three decades [1]. Almost four decades later, in 1936, the waveguide was rediscovered by G. C. Southworth from Bell Telephone Laboratories (BTL) and W. L. Barrow from Massachusetts Institute of Technology (M.I.T). The announcement of their discoveries was made public on successive days. As their research did not extend beyond the people affiliated with the project at their respective institutions, neither of them was aware of the other's research.

The first concept of a filter was independently proposed in 1915 by Wagner (Germany) and Campbell (United States) [2]. In 1923 at Bell Laboratories, Zobel published the Image parameter technique for designing passive lumped filters [3]. For decades his method was the only practical filter design method used by filter designers [2]. Later in the 1940's, Darling and Cauer synthesised networks to prescribed transfer functions [2]. At that time, the extreme computations required was impractical: it was only of academic interest until the arrival of the personal computer. It was only in 1954 that formulas were derived for lowpass prototype element values [4]. From these advances, other filter structures could be derived and the lowpass prototype values were tabulated. This is referred to as the Modern filter theory [2]. In 1962, G. Matthaei published the theory and realisation of interdigital filters. The next year he published his theory on combline filters [4]. Research done by Matthaei and Cristal on multiplexers, also showed that filters could be connected in series or parallel. An additional network was then required at the common junction for the resulting mismatched immittance.

The coming of the Intelsat satellites in the 1960's resulted in the start of exponential growth in communication systems. In these systems, filters are required to divide a frequency band into a number of channels. The division of the channels and recombination of the channels are done by means of input and output multiplexers. These multiplexers consist of narrowband filters with bandwidths ranging typically from 0.2 % to 2% [5]. Over the last three decades, advances were made in designing new filter topologies, reducing mass and volume. In the 1990s and 2000s, industrial applications have led to drastic reductions in manufacturing costs and development time of filters [5].

## 1.2 About the Thesis

This thesis presents the design of an aperture-coupled coaxial diplexer for R-band, using a circuit model consisting of ideal inverters placed between TM-line resonators. A tuning procedure is developed which combines a GUI (graphical user interface) based MATLAB procedure with the measured response of the physical structure in an iterative fashion. Measured results show the diplexer to perform very well,

achieving better than -15dB over both pass-bands, and better than 74 dB isolation between bands.

In addition, the accuracy of two techniques for determining coupling coefficients in coaxial and waveguide resonators is investigated. One method uses the Eigenmode Method for determining the coupling coefficients in a physical resonator, and the second a circuit model representation utilising inverters to represent the coupling between resonators. Originally, Marcuvitz [6] presented circuit equivalent structure for capacitive and inductive discontinuities used to couple cavities in waveguide. As there are various circuit models, ranging from ideal, frequency independent reactances to models using inductor/capacitor combinations, it is not always clear which is the best model to use for a design. In recent times, modern CEM (Computational Electromagnetics) capabilities have also made it possible to calculate coupling factors directly from Eigenmode analysis of the physical structure. These methods are compared against each other for three coupling problems: that of aperture-coupled coaxial resonators, inductive post coupled waveguide resonators and inductive iris coupled waveguide resonators. In each case, the coupling coefficient calculated from the direct Eigenmode solution, is compared to that calculated from various equivalent circuits which had been fitted onto CST (Computer Simulation Technology) s-parameters of the physical structures. It is shown that the different techniques give different results for the two waveguide problems, but exactly the same results for the coaxial problem.

## 1.3 Layout of Thesis

Chapter 2 introduces the theory and implementation of a circuit model for an aperture-coupled coaxial diplexer as an application of inverters. Specifications for this diplexer, are also presented. A circuit model is realised in Microwave Office (MWO) and consists of distributed elements and admittance inverters. An in-depth discussion of coupling coefficients, unloaded and loaded quality factors, is given. Calculation and implementation of admittance inverters [7], are shown. The final diplexer response is presented.

Chapter 3 presents the available diplexer implementations and configurations. A concise design procedure for the physical realisation of a diplexer in Computer Simulation Technology Design Studio (CST) is discussed. The effect of dimensions on the three main variables i.e. the couplings between resonators, external loaded quality factor and the tuning frequency of the resonators, are investigated. The determination of the coupling coefficient and the resonant frequency between two resonators, are discussed. A final diplexer prototype is obtained and manufactured. A brief overview of the manufacturing procedure that was followed, is given. The tuning procedure as proposed by Ness [8], is discussed for the diplexer. A detailed graphical illustration of this procedure, together with a MATLAB application with a graphical user interface (GUI) created for aiding in fine-tuning the diplexer, are presented in Appendix A.

In Chapter 4 the coupling mechanisms employing coaxial and waveguide media are addressed. A comprehensive study is done in regards to the accurate representation of coupling coefficients in various inverter configurations in a circuit model. Numerical results of the inverter models are compared to coupling coefficients obtained by the Eigenmode method (implemented in CST). Physical dimensions resulting from the three inverter models under investigation, are then implemented as a third order Chebyshev filter. The results of the final filters are shown. The deviation of the three inverter configurations from the Eigenmode Method, is addressed.

# Chapter 2

# Circuit Model for a Narrowband Diplexer

## 2.1 Introduction

As a first step in the design of an aperture coupled coaxial cavity diplexer, a distributed-element circuit, utilising the ideal admittance inverter, is designed. For the purposes of this thesis, filters will not be designed from first principles, such as the methods by Foster and Cauer [9]. Rather, normalised k- and q values, see section 2.7, are obtained from low-pass filter prototypes as in [10].

The matters relating to the circuit model design such as impedance/admittance inverters, normalised k-and q values, implementation of diplexer by means of inverters, are addressed. Lastly, the final implementation of the diplexer is presented. The final schematic of the diplexer in Microwave Office (MWO) is included. The final k- and q values as well as the resulting s-parameters are shown. This circuit model of the diplexer will form the foundation for comparison with the physical realisation of the diplexer, developed in Chapter 3.

## 2.2 Narrowband Coupled Resonators

Bandpass filters can be constructed from interconnections of identical high-quality factor cavity resonators [11]. According to Atia [11], when these identical cavity resonators are placed in cascade, it produces an all-pole insertion loss function.

This restriction is placed on the design due to the transforming of the optimum low-pass ladder network to a coupled-cavity structure [12].

As the diplexer to be designed contains no cross couplings, normalised k- and q values obtained from [10] could be used to determine the coupling coefficient between the resonators. For filters with cross-couplings, the normalised coupling coefficients can be obtained from the coupling matrix. Due to the cross-couplings not being applicable to this diplexer design, the coupling matrix will be addressed briefly. For a more comprehensive investigation into the coupling matrix synthesis and similarity transforms, the reader is referred to [12], [11], [13] and [14].

An equivalent circuit for multiple-coupled and identically tuned cavities is presented in Fig. 2.1. The identical cavities are tuned to a normalised resonant frequency of $\omega_o = \frac{1}{\sqrt{LC}} = 1$ rad.s$^{-1}$, where $L$ equals 1 Henry and $C$ is equal to 1 Farad [11]. Characteristic impedance of the general two-port network, $Z_o$ equals $\sqrt{L/C}$ [11].

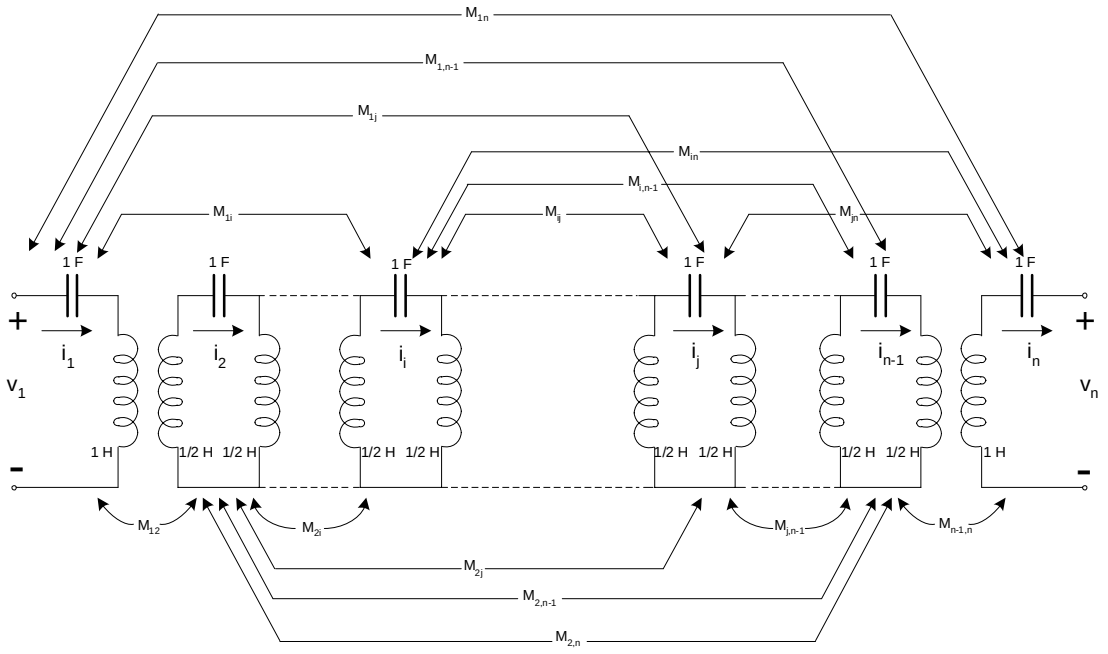


Figure 2.1: A general two-port network composed of tuned coupled cavities. Adapted from [11].

By assuming narrow-bandwidths ($\omega = \omega_o = 1$), the symmetric coupling impedance matrix, $\jmath$M, can be defined as in Eq. 2.1 by means of a loop equation for the network.

$$\begin{bmatrix} v_1 \\ 0 \\ 0 \\ \cdot \\ \cdot \\ \cdot \\ -v_n \end{bmatrix} = \begin{bmatrix} S & -\jmath M_{12} & -\jmath M_{13} & \cdot\cdot & \cdot & -\jmath M_{1n} \\ -\jmath M_{12} & S & -\jmath M_{23} & \cdot\cdot & \cdot & \cdot \\ -\jmath M_{13} & \jmath & S & \cdot\cdot & \cdot & \cdot \\ \cdot & \cdot & \cdot & \cdot\cdot & \cdot & \cdot \\ \cdot & \cdot & \cdot & \cdot\cdot & \cdot & \cdot \\ \cdot & \cdot & \cdot & \cdot\cdot & S & -\jmath M_{n-1,n} \\ -\jmath M_{1n} & \cdot & \cdot & \cdot\cdot & -\jmath M_{n-1,n} & S \end{bmatrix} \begin{bmatrix} i_1 \\ i_2 \\ i_3 \\ \cdot \\ \cdot \\ i_{n-1} \\ i_n \end{bmatrix} \tag{2.1}$$

In Eq. 2.1 a temporary variable, $S$ is defined where

$$S = \jmath\omega L + \frac{1}{\jmath\omega C}|_{L=C=1} \tag{2.2}$$

The matrix form of Eq. 2.1 is given in Eq. 2.3

$$\mathbf{V} = \mathbf{ZI} \tag{2.3}$$

where $\mathbf{V}$ and $\mathbf{I}$ are the voltage- and current matrices respectively. The impedance matrix can be defined as in Eq. 2.4

$$\mathbf{Z} = S\mathbf{I} - \jmath\mathbf{M} \tag{2.4}$$

where $\mathbf{I}$ is the identity matrix and $\mathbf{M}$ the coupling matrix, $M_{ij}$ for $i \neq j$ and $M_{ij} = 0$ for $i = j$.

The general coupling matrix can be manipulated to realise various inter-couplings between resonators. Consequently, various filter configurations can be realised (cross couplings) and not only limited to cascaded connections of resonators cavities.

## 2.3 Diplexer Synthesis

The definition of a multiplexer is given by [2] as a device with a common port which directs energy to a number of ports based on the frequency band of the directed energy. A diplexer is defined as a multiplexer with a common port and two frequency diversified ports [2].

### 2.3.1 Specifications for Diplexer

A diplexer is to be designed to filter out two predesignated filter bands in a communication link in a satellite. The frequency range of this diplexer is shown in Table 2-I

Table 2-I: The desired frequency bands of the diplexer

| **Band** | **Frequency$_{\text{lower}}$ [GHz]** | **Frequency$_{\text{higher}}$ [GHz]** |
|---|---|---|
| 1 | 1.980 | 2.01 |
| 2 | 2.170 | 2.2 |

The following specifications are a requirement for the satellite project:

- Ports 1, 2 and 3 are Input, Band 2 and Band 1 respectively. This is illustrated in Fig. 2.2.
- Transmission ($S_{21}$, $S_{31}$) > -3 dB in both passbands
- Reflection ($S_{11}$) < -20 dB in both passbands
- Isolation between the two frequency bands should be greater than 60 dB.

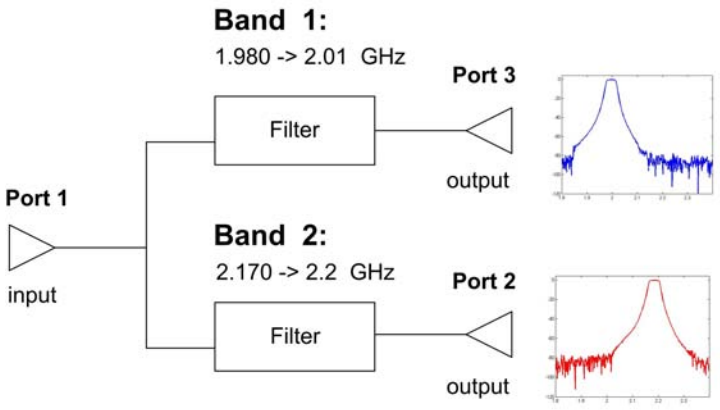


Figure 2.2: Block diagram of diplexer showing port 1, 2 and 3. They are respectively input, band 2 and band 1.

## 2.4 Concise Design Procedure for Circuit Element Model

Two bandpass filters are designed for the two specified frequency bands. These two filters are then to be connected such that port 1 becomes a port common to both filters as shown in 2.5. An extra tuning of the k- and q values will be required for the final diplexer prototype [7], [15]. This is essential to compensate for the mutual loading effects that occur when the two filters share a common port. The detailed design procedure of the two filters as well as the diplexer will be given in section 2.5.

Design specifications will ultimately be the decisive factor that will govern the order and type of filter used. A circuit model representation of a coaxially coupled resonator is implemented in Microwave Office. The rationale for the use of these circuit elements is discussed in Chapter 3.

For a resonance to occur at the required frequency, the values for the circuit elements must be calculated. The corresponding k- and q values can be found in filter design handbooks such as [10]. The normalised k- and q values [10] must be scaled in accordance to the desired bandwidth [16]. After the input impedance is calculated, the parameters for the inverters can be computed.

The final filter is implemented by placing the inverters and their corresponding resonators in cascade. This is graphically illustrated in Fig. 2.7 and 2.8. The inputs of the two filters are connected such that port 1 is common to both the filters.

## 2.5 Detailed Design Procedure

### 2.5.1 Filter Type and Minimum Order

The following filters were considered for the diplexer design: Butterworth, Chebyshev and Maximally flat delay filters. In Fig 2.3, $S_{21}$ of the three filter prototypes are shown. It can be seen that the Chebyshev has the sharpest roll-off of the three, followed by Butterworth and lastly the Maximally flat [17].

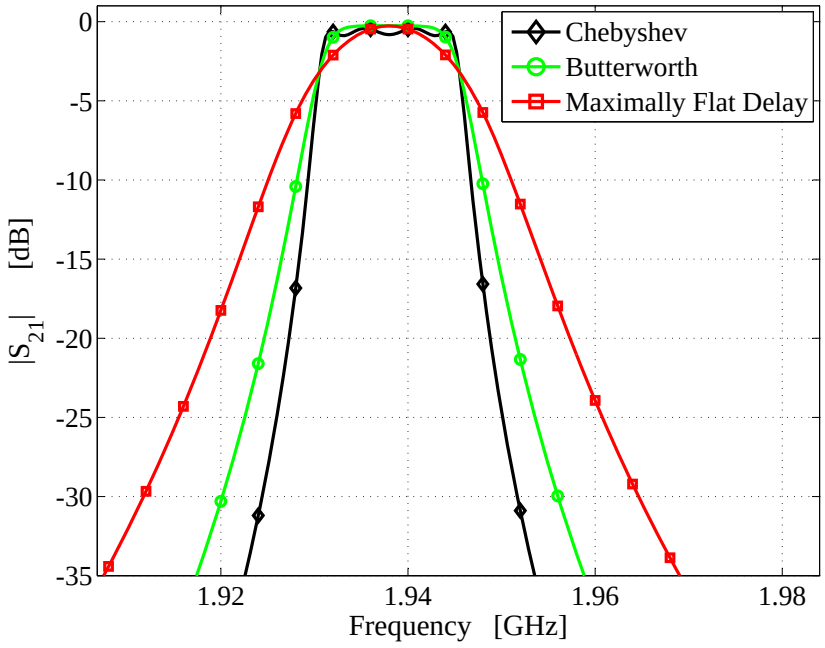


Figure 2.3: Fourth order filter $S_{21}$ response of a Butterworth, Chebyshev with 0.5 dB ripple and a Maximally flat bandpass filter. Note that the Chebyshev has the fastest roll-off of the three. A ripple of 0.5 was used to illustrate the ripple effect on $S_{21}$ in the passband.

Although the Chebyshev has noticeable ripple in the passband, this can be reduced by choosing a Chebyshev low-pass filter prototype with a smaller ripple in the passband.

Either the passband ripple or the reflection in the passband can be specified. For a Chebyshev filter with a ripple of 0.01 dB, the corresponding $S_{21}$ is calculated as in Eq. 2.5.

$$\begin{aligned} |S_{21}|_{min} &= 10^{\frac{-ripple\ \ in\ \ dB}{20}} \\ &= 10^{\frac{-0.01}{20}} \\ &= 0.99888 \qquad [dB] \end{aligned} \tag{2.5}$$

For a lossless system, the unitary condition [18] of Eq. 2.6 holds.

$$\begin{aligned} |S_{11}|^2 + |S_{21}|^2 &= 1 \\ |S_{11}|^2_{max} + |S_{21}|^2_{min} &= 1 \end{aligned} \tag{2.6}$$

$|S_{11}|_{max}$ can be calculated by Eq. 2.7.

$$\begin{aligned} |S_{11}|_{max} &= \sqrt{1 - |S_{21}|^2_{min}} \\ &= \sqrt{1 - 0.9988^2} \\ &= -26.382 \qquad [dB] \end{aligned} \tag{2.7}$$

### 2.5.2 Design of Resonator

The circuit resonator model representing the physical coaxial resonator, consists of a capacitor, a transmission line and resistor in parallel, see Fig. 2.4. As a short circuited transmission line will resonate at a quarter wavelength [17], the choice of length would be 90°. By adding a shunt capacitance, the resonant frequency will decrease. Consequently, the resonating frequency will occur at an electrical length less than 90°.

For very short coaxial resonators (length $<< \frac{\lambda}{10}$), an inductor can be used instead of the transmission line. As the physical length of the resonator was chosen as 80° the resulting phase difference is modelled by the transmission line. The characteristic impedance of the resonator is taken as 77 Ω for minimum power dissipation (a detailed explanation follows in section 3.6.1). The port impedance of the diplexer is 50 Ω.

### 2.5.3 Determination of Capacitance for Resonance

Resonance will occur when $Z_{in}(\omega_o) = 0$ for a series configuration [17]. For the shunt configuration [17], resonance will occur when $Y_{in}(\omega_o) = 0$. This is graphically illustrated in Fig. 2.4.

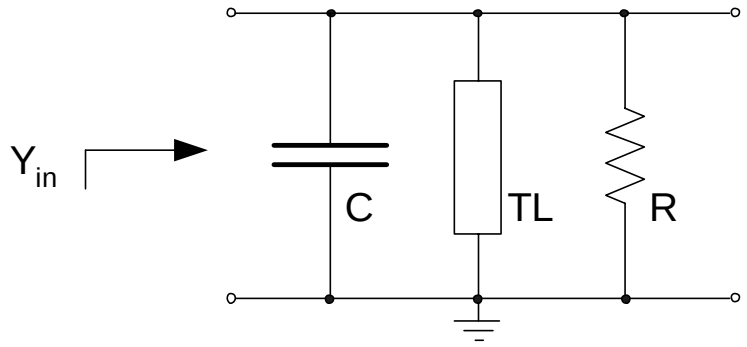


Figure 2.4: Resonator consisting of a capacitor, transmission line and resistor in parallel

For the resonating structure, the total admittance may be found by setting the admittance of the capacitor equal to the input admittance of a short circuited transmission line as in Eq. 2.8.

$$j\omega_o C = jy_o \cot(\beta\ell) \tag{2.8}$$

where $y_o$ denotes the characteristic admittance of the resonator and is equal to $\frac{1}{77}$ Siemens, with $\omega_o$ the resonating frequency (in Hz) and $\theta$ the electrical length of the resonator (with respect to the wavelength) in degrees. The capacitance in the resonator circuit can be expressed as in Eq. 2.9

$$C = \frac{y_o}{\omega_o} \cot(\theta_o) \qquad [\text{F}] \tag{2.9}$$

$\theta_o$ can be written in terms of $\beta$ and the length $\ell$ of the resonator, c denotes the speed of light in a vacuum (c = $3.10^8$ m.s$^{-1}$) and $\ell$ is the length of the transmission line (in m) as shown in Eq. 2.10.

The electrical length ($\theta_o$) can be written as

$$\begin{aligned} \theta_o &= \beta\ell \\ &= \frac{2\pi\ell}{\lambda} \\ &= \frac{2\pi f\ell}{c} \\ &= \omega_o(\frac{\ell}{c}) \end{aligned} \tag{2.10}$$

When the resonator in Fig. 2.4 is placed between a source and a load, the s-parameters in 2.5 are obtained. Note the perfect transmission and zero reflection at $f_o$. This is only valid for loss-less (infinite quality factor) resonators.

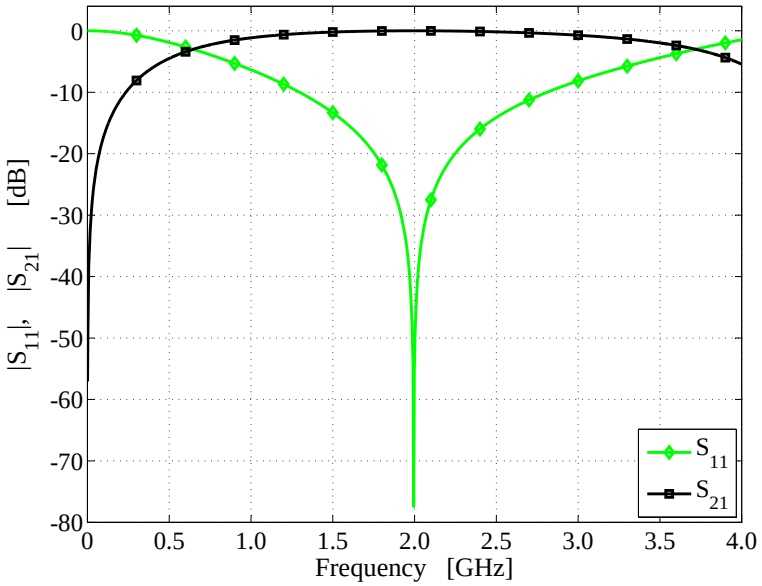


Figure 2.5: $S_{21}$ and $S_{11}$ of a loss-less shunt resonator consisting of a capacitor and transmission line in parallel, placed between a source and a load. Resonance occurs at 1.995 GHz.

### 2.5.4 Impedance and Admittance Inverters

An ideal impedance inverter is a lossless, reciprocal, frequency independent two-port network [18] and can be defined by a transfer matrix, as in Eq. 2.11.

$$\left[\ T\ \right] = \begin{bmatrix} 0 & jK \\ \frac{j}{K} & 0 \end{bmatrix} \tag{2.11}$$

When an inverter is connected to a load impedance, the input impedance will be the inverse of the load impedance. This also holds true for an admittance, ie. the input admittance will be the inverse of the load admittance [17]. This is shown in Eq. 2.12, where $K$ and $J$ are the series and shunt configuration inverters respectively.

$$Z_{in} = \frac{K^2}{Z_L} \qquad [\Omega]$$

$$Y_{in} = \frac{J^2}{Y_L} \qquad [\Omega] \tag{2.12}$$

As a result, a series capacitor/inductor can be transformed to a shunt inductor/capacitor and vice versa. This relation is graphically illustrated in Fig. 2.6a and Fig. 2.6b. Impedance and admittance inverters causes a $\pm$ 90° phase shift or a multiple thereof [2].

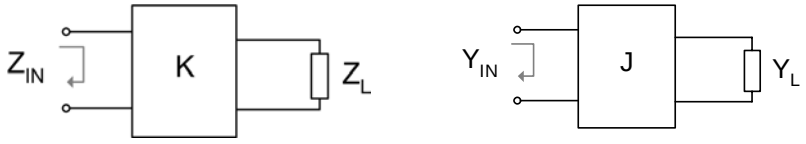


(a) Impedance inverter (b) Admittance inverter

Figure 2.6: Input impedance and admittance of inverter and load [17]

Bandpass filters are often constructed from normalised low-pass filter prototypes found in a filter design handbook [10] and then bandwidth and impedance transformed to obtain the correct bandpass filter. These low-pass filter prototypes normally consist of a ladder network. By using inverters, a bandpass filter can be obtained consisting of resonators in cascade with inverters placed in between. Consequently, the filter only consist of either series or shunt elements [18].

Matthaei et al showed that an unique relationship exists between the coupling factor between two resonators and an inverter performing the same function. For any series or shunt resonator, a reactance or susceptance slope parameter can be defined by Eq. 2.13 and Eq. 2.14 where $\chi$ and $b$ denotes the reactance and susceptance slope parameter of a series and shunt resonating circuit respectively.

$$\chi = \frac{\omega_o}{2}\frac{dX}{d\omega}\Big|_{\omega_o} \qquad [\Omega] \tag{2.13}$$

$$b = \frac{\omega_o}{2}\frac{dB}{d\omega}\Big|_{\omega_o} \qquad [Siemens] \tag{2.14}$$

An inverter for series resonator [16] is defined as follows in Eq. 2.15 and Eq. 2.16 where $K_{01}$ and $K_{n,n+1}$ represents the series configuration inverter for the loaded- $q_o$ and $q_n$ respectively. The loaded- $q_o$ and $q_n$ denotes the bandwidth scaled q - values.

$$K_{01} = \sqrt{Z_o \frac{\chi}{q_o}} \tag{2.15}$$

$$K_{n,n+1} = \sqrt{Z_o \frac{\chi}{q_n}} \tag{2.16}$$

An inverter between resonators $i$ and $j$ is represented by Eq. 2.17, where $k_{ij}$ represents the bandwidth scaled coupling coefficient between the $i^{th}$ and $j^{th}$ resonator. The implementation of above mentioned inverters are shown in Fig. 2.7. The k- and q values will be discussed in detail in section 2.7.

$$K_{ij} = k_{ij} \times \chi \tag{2.17}$$

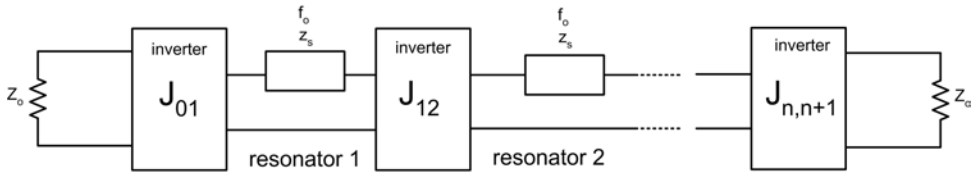


Figure 2.7: Series topology for implementation of inverter [16]

Equations 2.18 to 2.20 holds true for a shunt resonator. The admittance inverter, $J_{01}$ and $J_{n,n+1}$, represents the shunt configuration inverter for the loaded q. This is illustrated in Fig. 2.8.

$$J_{01} = \frac{1}{\sqrt{Z_o \frac{q_o}{b}}} \tag{2.18}$$

$$J_{n,n+1} = \frac{1}{\sqrt{Z_o \frac{q_n}{b}}} \tag{2.19}$$

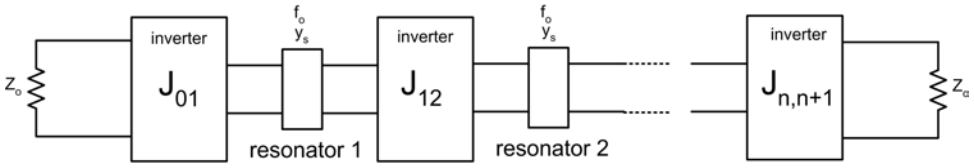


Figure 2.8: Shunt topology for implementation of inverter [16]

$$J_{ij} = k_{ij} \times \mathrm{b} \tag{2.20}$$

In a series topology, an inverter can be represented by a T-impedance network, see Fig 2.9a. For the shunt configuration, a Π-admittance network is used as shown in Fig. 2.9b.

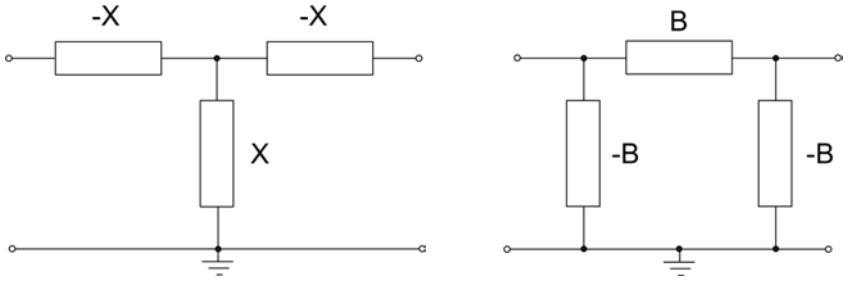


(a) Impedance inverter (b) Admittance inverter

Figure 2.9: Impedance and admittance inverters [16]

Consequently for any given resonator, an inverter exists that will result in the correct coupling between the adjacent resonators, given that the following information is known:

- reactance or susceptance slope parameter

- coupling coefficient between the resonators
- loaded q of the resonator
- characteristic impedance of the resonator

## 2.6 An Equivalent Circuit for Magnetically Coupled Coils

Magnetically coupled coils as given in Fig. 2.10 can be modelled with an equivalent circuit that does not involve magnetic coupling, as illustrated in Fig. 2.11 [19].

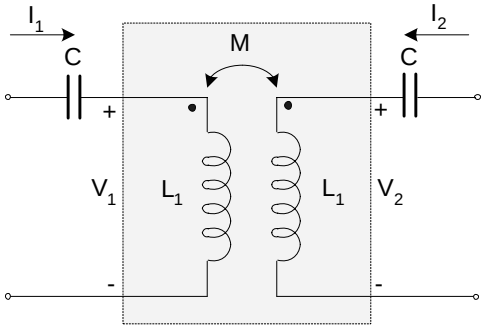


Figure 2.10: The circuit used to develop an equivalent circuit for magnetically coupled coils. Adapted from [19].

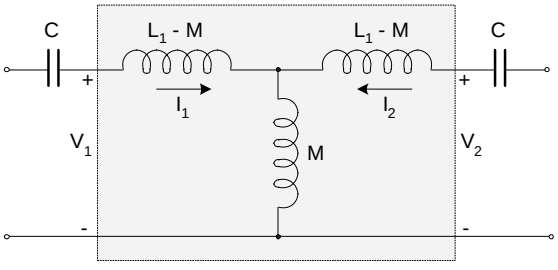


Figure 2.11: The T-equivalent circuit for the magnetically coupled coils of Fig. 2.10. Adapted from [19].

The equivalent T-circuit in Fig. 2.11 can also be represented as in Fig 2.12. Note that the inductance $L_1$ is grouped together with the series resonator consisting of a capacitor, $C$.

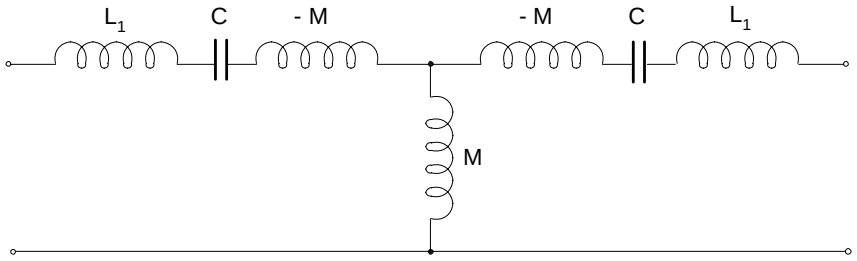


Figure 2.12: Inductance $L_1$ grouped together with series resonator, $C$.

The centre part of the circuit consisting of inductances, $M$, can be replaced with an ideal impedance inverter with reactances, $X$. This is illustrated in Fig. 2.13. Consequently, a coupled network can be represented by an inverter.

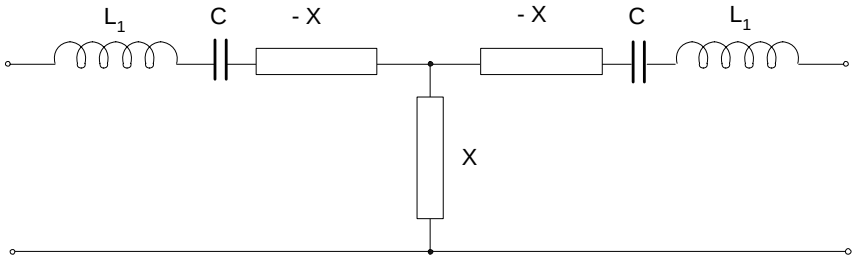


Figure 2.13: An ideal impedance inverter placed between series resonators

## 2.7 k and q values

The coupling coefficient is defined as the normalised coupling coefficient, $k$, between two resonators in the normalised low-pass filter prototype and is defined as in Eq. 2.21, where $g_i$ and $g_j$ are the capacitor and inductor values in the low-pass filter prototype [7].

Bandpass filters can be designed by using normalised low-pass filter prototypes. By using low-pass filter prototypes, the designer can use predefined element values as found in filter design handbooks [10]. Values obtained can then be bandwidth transformed and impedance scaled, resulting in a bandpass filter.

The low-pass filter prototypes consist of ladder networks with elements normally designated with the symbol $g$, which can be either capacitance, inductance, resistance or conductance, depending on the circuit element. These $g$ element values are normalised values calculated with a load impedance of $R_l = 1$ and a cutoff frequency, $w_c = 1$. Values of the elements are numbered chronologically from the generator impedance, denoted by $g_o$ to the load impedance, denoted by $g_{n+1}$ where $N$ is number of reactive elements of the filter [17].

Coupling coefficients can then be defined [20] as in Eq. 2.21.

$$k_{i,i+1} = \frac{BW}{\sqrt{g_i \cdot g_{i+1}}} \quad \text{for i = 1 to (N - 1)} \tag{2.21}$$

The loaded quality factor of the filter, $q_i$ and $q_N$ may be obtained by Eq. 2.22 and Eq. 2.23 [20]. The fractional bandwidth, $BW$ is defined in Eq. 2.24. The centre frequency is denoted by $f_o$ in Hz.

$$q_1 = \frac{g_o \cdot g_1}{BW} \tag{2.22}$$

$$q_N = \frac{g_N \cdot g_{N+1}}{BW} \tag{2.23}$$

$$BW = \frac{\Delta f}{f_o} = \frac{f_{upper} - f_{lower}}{fo} \tag{2.24}$$

The $g$ element values are normalised and can be impedance scaled by Eq. 2.25 as given in [17].

$$\begin{aligned} L' &= R_o L \\ C' &= \frac{C}{R_o} \end{aligned} \tag{2.25}$$

where the primes denote the impedance scaled quantities, $R_o$ the source resistance in Ohm and $L$ and $C$ the non-impedance-scaled inductance and capacitance.

When impedance scaled capacitance and inductance values (computed by means of Eq. 2.25), are used in Eq. 2.21, Eq. 2.22 and Eq. 2.23, it is clear that the k- and q values are independent of this scaling. The normalised k- and q values for a fourth order Chebyshev low-pass filter prototype with 0.01 dB ripple are listed in Table 2-II [10].

Table 2-II: The normalised k- and q values for a fourth order Chebyshev low-pass filter prototype with 0.01 dB for both the frequency bands of the diplexer [10]. $R_l = 1$ and $\Omega = 1$

| **Inverter** | $q_1$, $q_N$, $k_{i,i+N}$ | **Value** |
|---|---|---|
| $\mathbf{J}_{01}$ | $\mathbf{q}_l$ | **1.065** |
| $\mathbf{J}_{12}$ | $\mathbf{k}_{l2}$ | **0.7369** |
| $\mathbf{J}_{23}$ | $\mathbf{k}_{23}$ | **0.5413** |
| $\mathbf{J}_{34}$ | $\mathbf{k}_{34}$ | **0.7369** |
| $\mathbf{J}_N$ | $\mathbf{q}_N$ | **1.046** |

As these values still represent the coupling between the resonators of normalised low-pass filter, the k and q require scaling. Scaled k and q values are obtained by Eq. 2.26 and 2.27.

$$k_{bandwidth\ scaled} = k \times BW \tag{2.26}$$

$$q_{bandwidth\ scaled} = \frac{q}{BW} \tag{2.27}$$

### 2.7.1 Calculation of an Admittance Inverter

The input admittance when looking into the resonator and inverter can be determined as expressed in Eq. 2.28.

$$Y_{in} = \jmath B = \jmath\omega C - \jmath Y_o \cot(\beta\ell) \tag{2.28}$$

As $\theta = \beta\ell$, substitute into Eq. 2.28 to obtain Eq. 2.29.

$$B = \omega C - Y_o \cot(\theta) \tag{2.29}$$

Set $T = \frac{\ell}{c}$ and substitute into Eq. 2.29. By taking the derivative in terms of $\omega$, Eq. 2.30 is obtained.

$$\frac{\partial B}{\partial \omega} = C + TY_o \csc^2(\omega T) \tag{2.30}$$

The susceptance slope parameter can then be defined as in Eq. 2.31.

$$\begin{aligned} b &= \frac{\omega_o}{2}\frac{dB}{d\omega}\Big|_{\omega_o} \\ b &= \frac{\omega_o}{2}\left[C + TY_o \csc^2(\omega_o T)\right] \qquad [\mathrm{S}] \end{aligned} \tag{2.31}$$

In Eq. 2.31, substitute $T$ with $\frac{\ell}{c}$ and from 2.10 it yields Eq. 2.32.

$$\theta_o = \omega T \tag{2.32}$$

Substituting into Eq. 2.31 yields Eq. 2.33.

$$\begin{aligned} b &= \frac{\omega_o C}{2} + \frac{Y_o \omega_o T}{2} \csc^2(\theta_o) \\ b &= \frac{\omega_o C}{2} + \frac{Y_o \theta}{2} \csc^2(\theta_o) \end{aligned} \tag{2.33}$$

All requisites to be able to define an inverter is now known. The inverter for the shunt configuration can be defined as in Eq. 2.18, 2.19 and 2.20.

Inverters, $J_{01}$ and $J_{n,n+1}$ can be calculated by using Eq. 2.34 and 2.35.

$$\begin{aligned} J_{01} &= \frac{1}{\sqrt{Z_o \frac{q_o}{b}}} \\ &= \frac{1}{\sqrt{50 \frac{0.7654}{b}}} \end{aligned} \tag{2.34}$$

$$\begin{aligned} J_{n,n+1} &= \frac{1}{\sqrt{Z_o \frac{q_n}{b}}} \\ &= \frac{1}{\sqrt{50 \frac{0.7654}{b}}} \end{aligned} \tag{2.35}$$

The inverters for $J_{12}$, $J_{23}$ and $J_{34}$ are then defined in terms of the coupling coefficient as in Eq. 2.37 [16].

$$J_{ij} = k_{ij} b \tag{2.36}$$

## 2.8 Unloaded Q of Resonator

Resonators will have energy dissipation due to the inherent resistive nature of non-ideal metals. This resulting energy dissipation will lead to a decrease in the unloaded quality factor. The unloaded quality factor is entirely dependant on the resonator itself in the absence of any external loading effects due to external circuits or coupling [17]. The unloaded Q -factor of the resonator [18] is defined by Eq. 2.37.

$$Q_u = \frac{2\pi \times \text{maximum energy stored in a cycle}}{\text{energy dissipated per cycle}} \tag{2.37}$$

An increase in resistive loss will result in a lower quality factor. The higher the quality factor, the less energy will be dissipated in the resistive element of the resonator [17]. The unloaded Q factor ($Q_u$) of the resonator [2] can be calculated as in Eq. 2.38 where

$$Q_u = \frac{X}{R} \tag{2.38}$$

$$\begin{aligned} \text{X} &= \text{reactance of resonator} \quad [\Omega] \\ \text{R} &= \text{resistance of resistor} \quad [\Omega] \end{aligned}$$

For the resonator model with an resistive element in parallel, the $Q_u$-factor in terms of suceptance is, Eq. 2.39 where

$$Q_u = \text{B} \times \text{R} \tag{2.39}$$

$$\begin{aligned} \text{B} &= \text{susceptance of resonator} \quad [S] \\ \text{R} &= \text{resistance of resistor} \quad [\Omega] \end{aligned}$$

### 2.8.1 Resistor value for practical $Q_u$-values

The effect of the unloaded quality factor on the response of one of the diplexer filters is investigated. In Fig. 2.14 the results of various unloaded quality factors are shown.

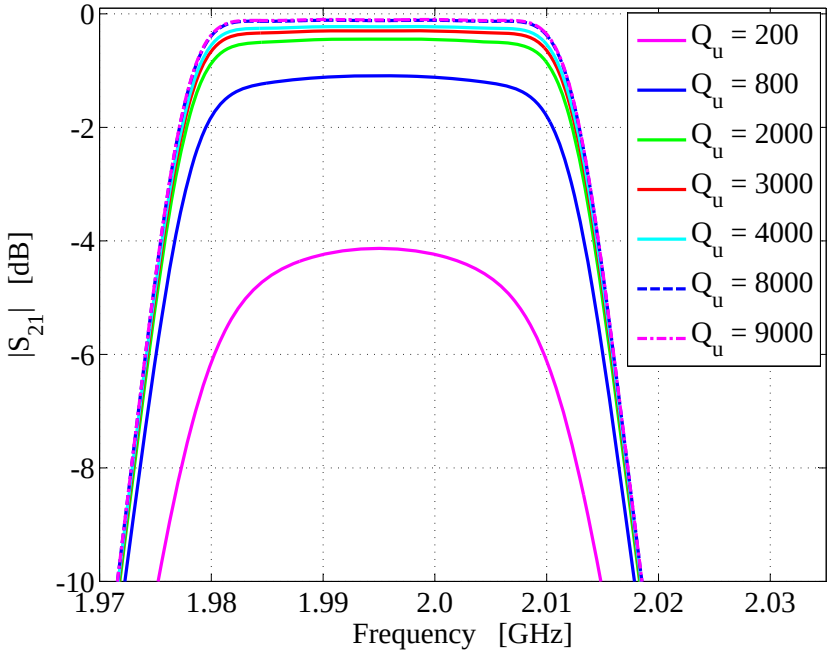


Figure 2.14: Effect of different $Q_u$ on $S_{21}$. $R = \frac{Q_u}{B}$. $Q_u$ is indirectly proportional to the midband insertion loss [18].

From the results, it is clear that $Q_u$ is indirectly proportional to the midband insertion loss [18]. An increase in $Q_u$ will decrease the band-edge loss and subsequently decrease the bandwidth. By decreasing $Q_u$, the band-edge loss increases. To ensure that $S_{21}$ exceeds -3 dB, a $Q_u$ above 600 will be sufficient. A unloaded quality factor is to be selected that will yield the highest possible unloaded quality factor for the allowed space envelope while still maintaining a practical realisable value. For this application, the available space allowed for resonators with an unloaded quality factor of approximately 3000.

## 2.9 Final Diplexer Implementation

The diplexer is formed by the combination of the two filters. As mentioned in section 2.4, this will result in a loading effect on both filters. In Fig. 2.15 the input impedance (real, imaginary and magnitude) versus frequency is shown of the 1.995 GHz resonator. The resonator consists of a capacitor, transmission line and resistor in parallel, Fig. 2.4. At the resonant frequency of 1.995 GHz, the input impedance will be purely resistive and equal to the resistance R and is calculated as $1.8564e5$ Ohm. Away from the resonant frequency, the input resistance deceases rapidly.

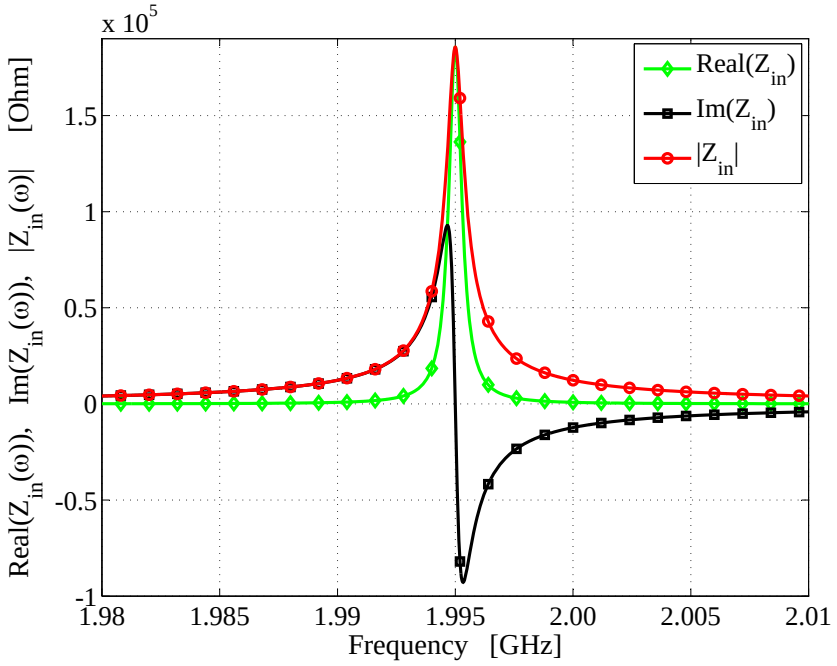


Figure 2.15: The input impedance (real, imaginary and magnitude) versus frequency of a resonator (frequency band 1) consisting of a capacitor, transmission line and resistor in parallel. Resonant frequency is at 1.995 GHz. At resonance, the magnitude of the real impedance equals $1.8564e + 005$ Ohm.

When a signal in the passband of filter 1 (lower frequency filter) is applied to the diplexer, the signal will pass through filter 1. At filter 2 (upper frequency band filter) which is also the stopband of filter 1, the signal will see a very small

reactance at the first resonator. This is in contrast with the large input resistance at resonance. The first inverter of filter 2 will then result in a very large input reactance when looking into filter 2. Ideally, the signal would see an open circuit as a result of the large input impedance of the rejecting filter. As a result, it will appear as an reactance in parallel with the input impedance of the non-rejecting filter 1. This is shown in Fig. 2.16.

The decreasing q-values can be contributed to this additional reactance. The reactance will increase the loading effect and result in an overall lowering of the q-values [17], Tables 2-III, 2-IV. This additional reactance will require an increase in the coupling between the resonators to cancel the effect of the additional loading effect, Tables 2-III, 2-IV.

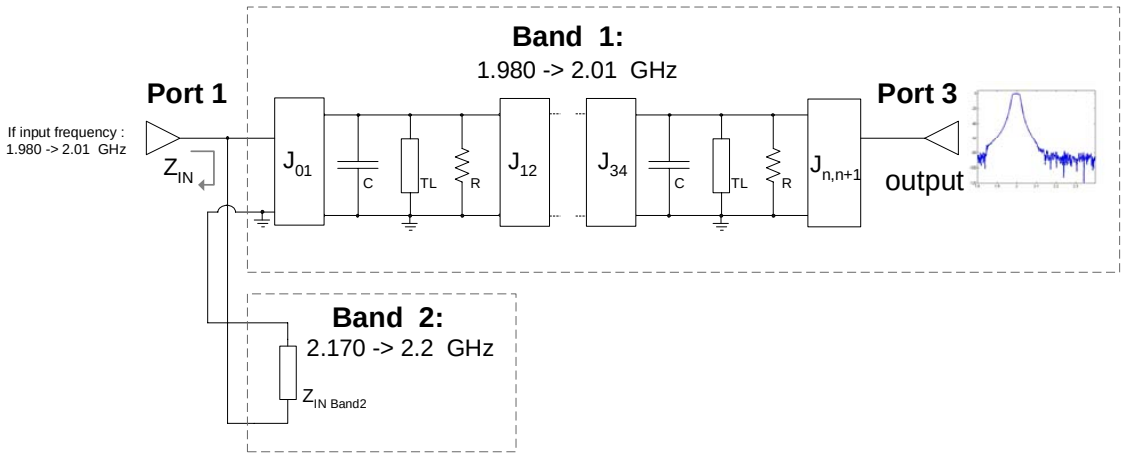


Figure 2.16: Input reactance of filter 2 due to an incoming signal in passband of filter 1. Result is the reactance in parallel with the input impedance of filter 1.

In Fig. 2.17, a schematic of the implementation of the diplexer is shown. The filter is configured by connecting port 1 as the common input to both filters. $J_{01_u}$, $J_{01_l}$, $J_{n_u}$ and $J_{n_u}$ represents the inverters for the loaded quality factor of the diplexer. The $u$ denotes the upper frequency band and the $l$ the lower frequency band.

Output ports are designated as port 2 for the upper frequency band and port 3 for the lower frequency band as specified in section 2.3.1.

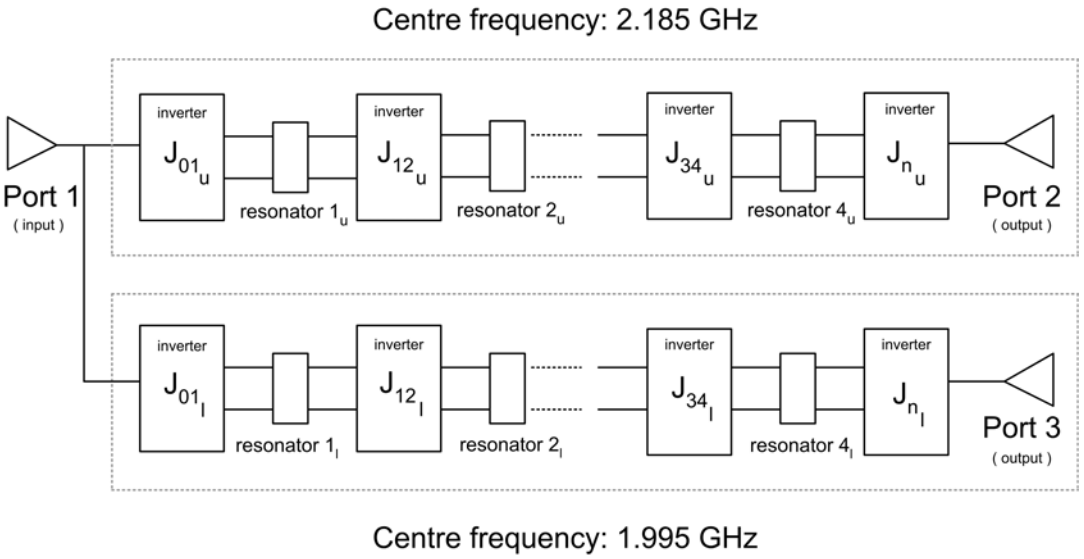


Figure 2.17: General topology of fourth order Chebyshev bandpass diplexer model. $u$ and $l$ denotes the upper and lower frequency band filter.

The filter response of filters 1 and 2 are given in Fig. 2.18b and Fig. 2.18b. The final schematics of filters 1, 2 and diplexer in Microwave Office are shown in Fig. 2.19, Fig. 2.20 and Fig. 2.21.

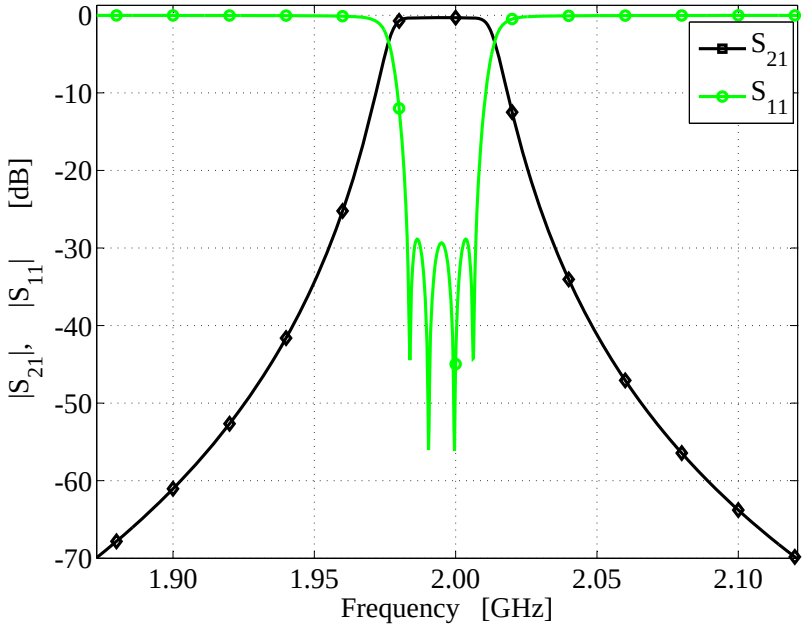


(a) Filter 1 (passband: 1.980 → 2.01 GHz)

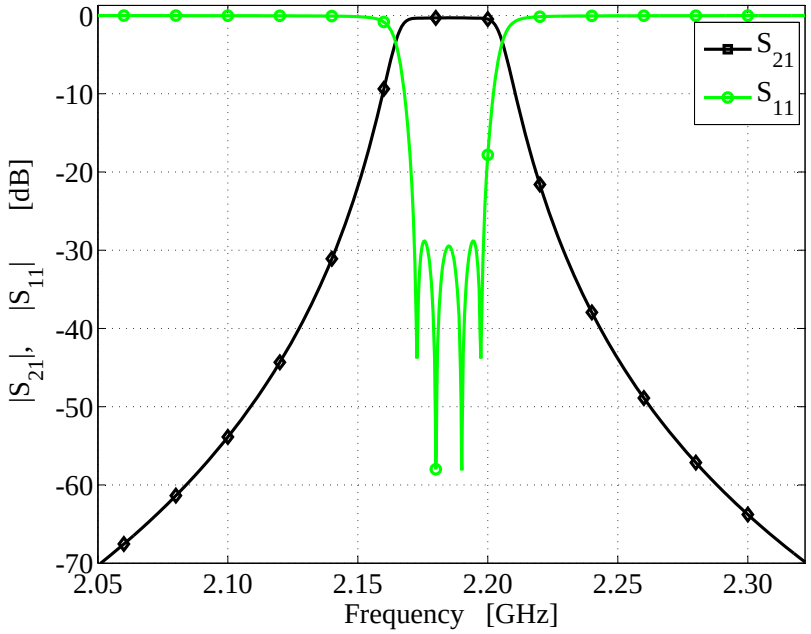


(b) Filter 2 (passband: 2.170 → 2.2 GHz)

Figure 2.18: Response of Filter 1 and 2

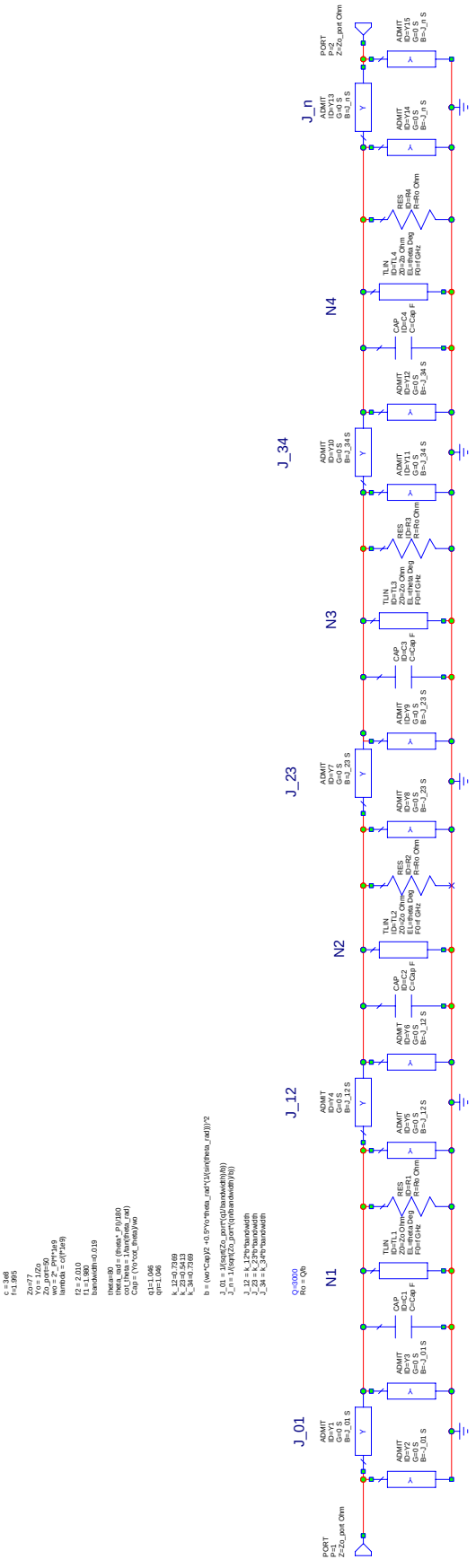


Figure 2.19: Schematic of Filter, centre frequency 1.995 GHz

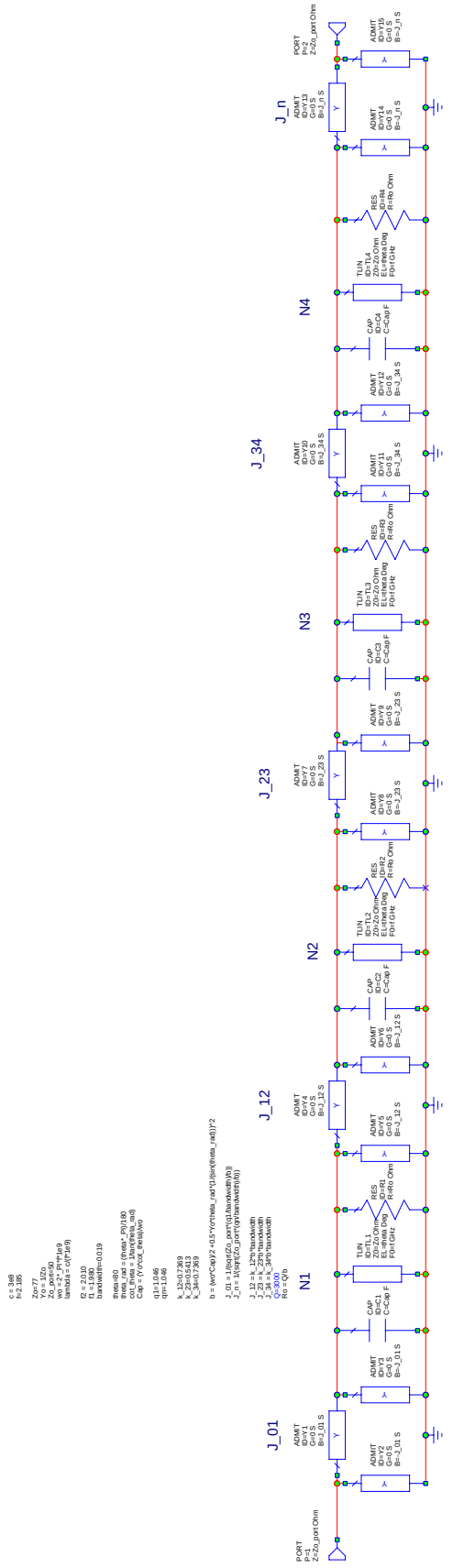


Figure 2.20: Schematic of Filter, centre frequency 2.185 GHz

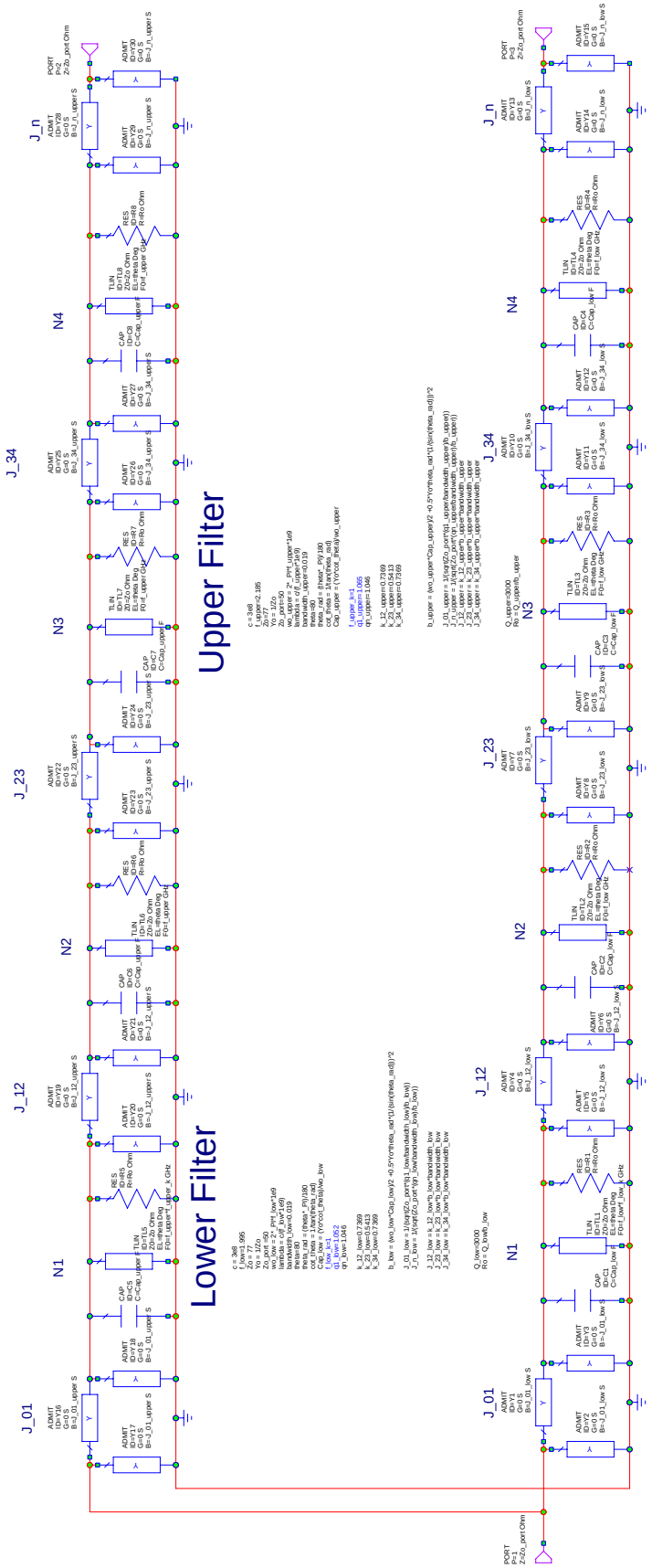


Figure 2.21: Schematic of Diplexer

To compensate for the loading effects, the optimiser in MWO is used to simply adjust the common port k- and q values slightly. These values are listed in tables 2-IV and 2-III.

Table 2-III: The final and tuned k and q values for the frequency band of 1.98 [GHz] to 2.01 [GHz] of the diplexer. Note that the q-values have decreased and the k-values have increased from the values in Table 2-II.

| **Inverter** | $q_1$, $q_N$, $k_{i,i+N}$ | **Value** |
|---|---|---|
| $\mathbf{J}_{01}$ | $\mathbf{q}_l$ | **0.8676** |
| $\mathbf{J}_{12}$ | $\mathbf{k}_{l2}$ | **0.8881** |
| $\mathbf{J}_{23}$ | $\mathbf{k}_{23}$ | **0.6842** |
| $\mathbf{J}_{34}$ | $\mathbf{k}_{34}$ | **1.026** |
| $\mathbf{J}_N$ | $\mathbf{q}_N$ | **0.6832** |

Table 2-IV: The final and tuned k and q values for the frequency band of 2.170 [GHz] to 2.2 [GHz] of the diplexer. Note that the q-values have decreased and the k-values have increased from the values in Table 2-II

| **Inverter** | $q_1$, $q_N$, $k_{i,i+N}$ | **Value** |
|---|---|---|
| $\mathbf{J}_{01}$ | $\mathbf{q}_l$ | **0.8676** |
| $\mathbf{J}_{12}$ | $\mathbf{k}_{l2}$ | **0.8270** |
| $\mathbf{J}_{23}$ | $\mathbf{k}_{23}$ | **0.6228** |
| $\mathbf{J}_{34}$ | $\mathbf{k}_{34}$ | **0.9362** |
| $\mathbf{J}_N$ | $\mathbf{q}_N$ | **0.7499** |

The final optimised loaded quality factors, bandwidth transformed for the final diplexer circuit are shown in Table 2-V.

The bandwidth transformed, final optimised coupling coefficients for the diplexer, are given in Table 2-VI.

Table 2-V: The optimised loaded quality factor, bandwidth transformed for filters 1 and 2

| **Loaded Quality Factor, q** | $\mathbf{q} \times \frac{1}{bandwidth}$ |
|---|---|
| $\mathbf{q}_{l_{lower}}$ | $0.8676 \times \frac{1}{0.019} = 45.66$ |
| $\mathbf{q}_{n_{lower}}$ | $0.6832 \times \frac{1}{0.019} = 35.96$ |
| $\mathbf{q}_{l_{upper}}$ | $0.8676 \times \frac{1}{0.019} = 45.66$ |
| $\mathbf{q}_{n_{upper}}$ | $0.7499 \times \frac{1}{0.019} = 39.47$ |

Table 2-VI: The optimised coupling coefficient, bandwidth transformed for filters 1 and 2

| **Coupling coefficient, k** | $\mathbf{k} \times$ **bandwidth** |
|---|---|
| $\mathbf{k}_{l2_{lower}}$ | $0.8881 \times 0.019 = 0.01687$ |
| $\mathbf{k}_{23_{lower}}$ | $0.6842 \times 0.019 = 0.01299$ |
| $\mathbf{k}_{34_{lower}}$ | $1.026 \times 0.019 = 0.019494$ |
| $\mathbf{k}_{l2_{upper}}$ | $0.8270 \times 0.019 = 0.015713$ |
| $\mathbf{k}_{23_{upper}}$ | $0.6228 \times 0.019 = 0.011833$ |
| $\mathbf{k}_{34_{upper}}$ | $0.9362 \times 0.019 = 0.017788$ |

The final s-parameters of the diplexer is shown in Fig. 2.22. In both the midbands, the reflection loss is smaller than 20 [dB]. A transmission loss in both passbands is greater than 0.4583 [dB]. Isolation between two frequency bands are smaller than 87 [dB].

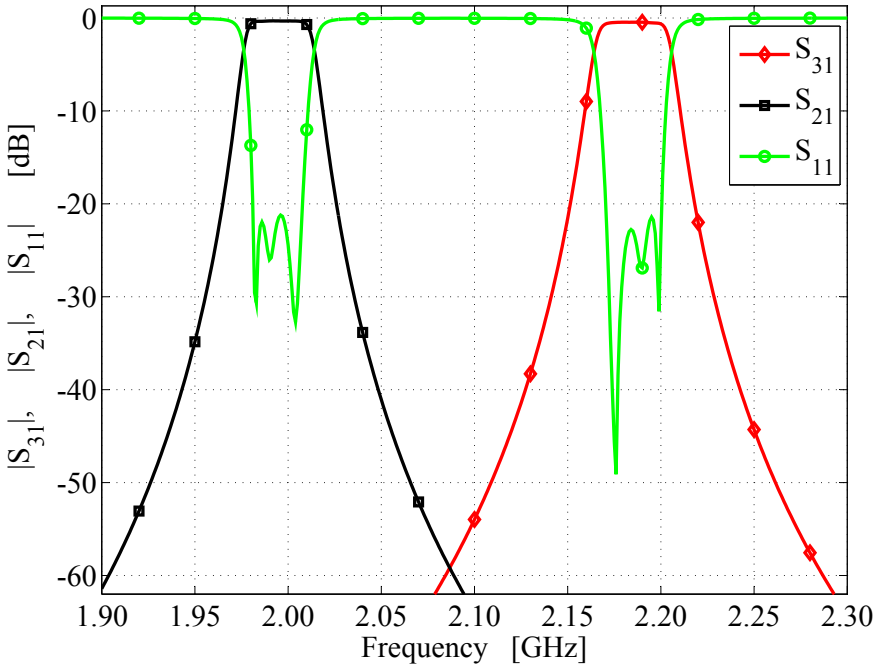


Figure 2.22: The S-parameters, $S_{21}$, $S_{31}$ and $S_{11}$, of the diplexer circuit model

## 2.10 Conclusion

Detailed design procedure is given regarding the design of an fourth order Chebyshev diplexer with a ripple of 0.01 dB. An overview of inverters and their calculation as well as implementation, are shown. Final diplexer results show that specifications are met. In Chapter 3 the physical realisation of this circuit model is reviewed.

# Chapter 3

# Physical Realisation of a Coaxial Cavity Diplexer

## 3.1 Introduction

This chapter describes the physical realisation of an aperture coupled coaxial cavity diplexer. Definitions of a combline and interdigital filter, are presented. A concise comparison of the various types of filter implementations available to the filter designer, as well as their resulting unloaded quality factor are discussed. The reasons for using a coaxial implementation as the preferred choice for implementation of the diplexer, are discussed.

The design approach of breaking the diplexer model into its key building blocks and obtaining preliminary dimensions, is discussed. An investigation into the effect of the dimensions of the diplexer model resulting in minimum power dissipation, resonating frequency of resonators, coupling coefficients and unloaded quality factors, are presented. A tuning method proposed by Ness [8] is presented. The schematic with the final dimensions obtained for the manufacturing stage of the diplexer model, together with the measured response of the diplexer, are presented. A MATLAB application with a graphical user interface (GUI) is presented as part of this thesis, written as a tool to assist in the measurement and tuning of the diplexer.

## 3.2 Diplexer Realisation Media

The diplexer is designed for use in satellite transmit and receive channels. As the space envelope of the diplexer is limited, the size and weight play an integral role in the choice of filter implementation. In Fig. 3.1 the various filter implementations available for realisation, are shown.

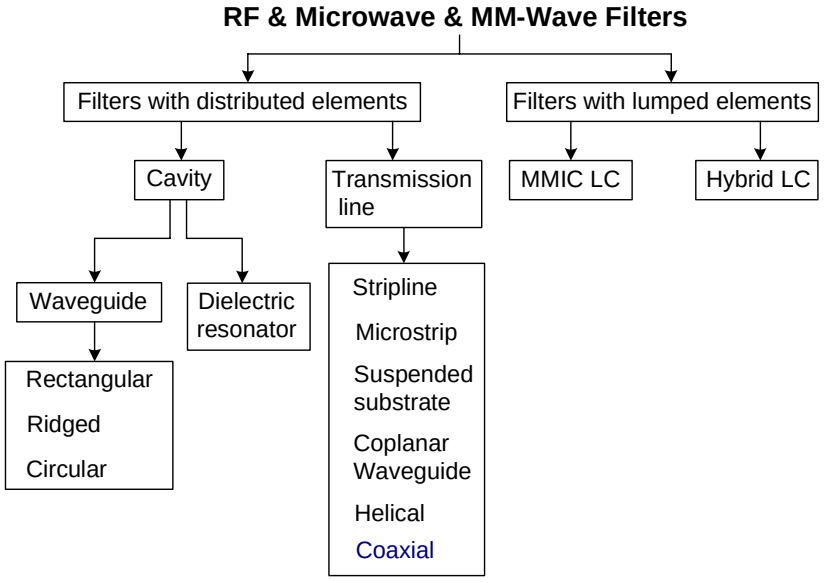


Figure 3.1: Flowchart of the available options for filter implementation. Adapted from [21].

The types of filter implementations available for implementation of the diplexer, is given in Table 3-I. Note that Table 3-I is given as a means of comparison for the different filter media, even though the frequency is given as 10 GHz. A lower frequency than 10 GHz will result in physically larger structures. With an increase in size, higher unloaded quality factors can be obtained. If a dielectric resonator is to be used, the manufacturing complexity will increase.

From Table 3-I [21], the three filter implementation types with the highest obtainable unloaded quality factors are coaxial, waveguide and dielectric resonators.

Table 3-I: Characteristics of various filter realisation media at a frequency of 10 GHz [21].

| **Media** | **Frequency [GHz]** | **Bandwidth (%)** | $\mathbf{Q}_{unloaded}$ |
|---|---|---|---|
| Coaxial | 0.1 - 40 | 1 - 30 | 2000 |
| Waveguide | 1 - 100 | 0.1 - 20 | 5000 |
| Stripline | 0.1 - 20 | 5-otave | 150 |
| Microstrip | 0.1 - 100 | 5-octave | 200 |
| Suspended microstrip | 1 - 200 | 2 - 20 | 1000 |
| Finline | 20 - 200 | 2 - 50 | 500 |
| Lumped elements | 0.01 - 10 (hybrid) | 20 - octave | 200 |
| | 0.1 - 60 (monolithic) | 20 - octave | 100 |
| Dielectric resonator | 0.9 - 40 | 0.2 - 20 | 10000 |

This is due to the high dielectric structure requiring physical support by a structure of low dielectric constant [18]. Using a dielectric will result that at the resonant frequency, most of the fields will be concentrated and contained within the dielectric [18] [17]. According to Pozar [17], these type of filters are generally smaller in cost, size and weight. At higher frequencies, this type of filter will became increasingly complex to manufacture due to its physically small size. A disadvantage to the use of this type of filter is the difficulty in tuning. As most of the fields are contained in the dielectric, extending a tuning screw will have little effect. The practical realisable loaded quality factor is lower due to the lossy nature of the adhesives used between the dielectric and the metal [21] but still higher than cavities.

However, using a waveguide will result in using approximate $\frac{\lambda}{2}$ resonators. As a result, the high unloaded quality factor comes at the price of increased physical size [2]. This is in contrast with a coaxial resonator where resonators are placed in parallel to one another. Consequently this diplexer is implemented as aperture coupled coaxial cavities.

## 3.3 Configurations Available for Implementation

### 3.3.1 Interdigital Filter

The interdigital filter consists of parallel coupled lines as shown in Fig. 3.2a. Each of the lines have an electrical length of $\frac{\lambda}{4}$ (90°) at the centre frequency. They are placed in such a manner that the lines alternate between short- and open circuited ends [22]. Interdigital filters have lower inter-couplings between the resonators [22], resulting in a physical size greater than that of a combline filter. This type of configuration is used in frequencies above 8 GHz [22], especially for filters with wider bandwidth specifications (up to 70 %) [2]. An ideal interdigital filter has symmetrical insertion loss [22] resulting in superior phase and delay characteristics compared to that of combline filters [22]. For tuning purposes, tuning screws are placed on opposite sides of the filter [18].

### 3.3.2 Combline Filter

The combline filter is similar to the interdigital filter in that it also consists of parallel coupled lines as in Fig. 3.2b. The length of each of these lines are less than 90° at the centre frequency. Lines are configured in such a manner that they are all short-circuited at one end. At the opposite end of the lines, they are capacitively loaded [2].

When the length of the line is decreased, the loaded quality factor will decrease [2]. As the length decreases, a larger capacitive load is required at the end of the line. At an electrical line length of 90°, the electric and magnetic coupling cancel, resulting in a bandstop filter [7]. This is due to the electric energy being equal to the magnetic energy (section 2.5.3) at the resonant frequency of the line. According to Matthaei et al [7], as capacitance is introduced and increased (in a coaxial implementation by means of a tuning screw), the magnetic fields start to dominate. According to Hunter [18], the inductive lines will start to resonate with the capacitance at a line length shorter than 90° [18].

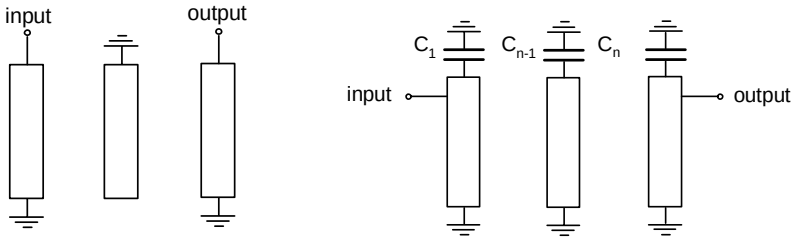


(a) Interdigital filter (b) Combline filter

Figure 3.2: Configuration of combline and interdigital filters in strip-line. Adapted from [18].

Combline filters are widely used in applications at frequencies below 10 GHz and provide excellent unloaded quality factors [22]. A disadvantage of this type of filter is the asymmetry of its insertion loss [18]. The insertion loss is usually greater on the high frequency side of the centre frequency of the combline filter [22] [18].

### 3.3.3 Coupled Coaxial Resonators

The size of a combline filter implemented as a coaxial resonator, can even be more reduced by introducing walls between the resonator posts as in Figure 3.3.

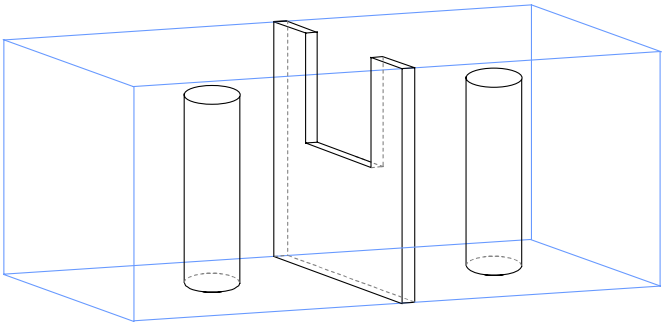

Figure 3.3: Implementation of a coupled coaxial resonator with walls between the posts

## 3.4 Physical Implementation of Circuit Model

It is the purpose of this section to describe the physical implementation of the circuit model in CST, as presented in Chapter 2. The diplexer is designed as an aperture coupled coaxial cavities. A graphical illustration of the sectional front view of the diplexer is shown in Fig. 3.4.

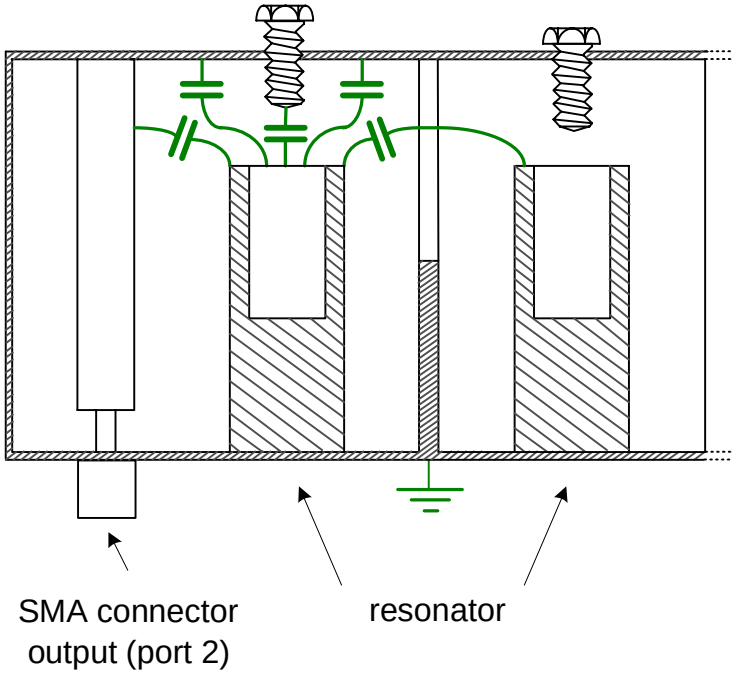


Figure 3.4: Sectional front view of the diplexer (in a combline configuration) set in coaxial media. The resonator is short-circuited to ground (entire casing of diplexer) at the undermost part of the structure.

Note that the resulting capacitance between the resonator- and roof/tuning screw are also shown. The diplexer will consist of interconnection of identical coaxial cavity resonators. Coupling between the resonators is controlled by an iris of a specific length and width to result in a predetermined coupling coefficient. The coaxial resonators are all short-circuited at the same end to the outer aluminium casing of the diplexer. As discussed in Section 3.3.2 of the combline configuration, the electrical length of the coaxial resonators are chosen to be less than 90°.

On account of the distance between the roof of the cavity and the height of the resonator, the circuit model will have a capacitance, short-circuited to the casing of the diplexer. For the sake of convenience, the circuit model (section 2.5.2) representation of Fig. 3.4, is duplicated below in Fig. 3.5.

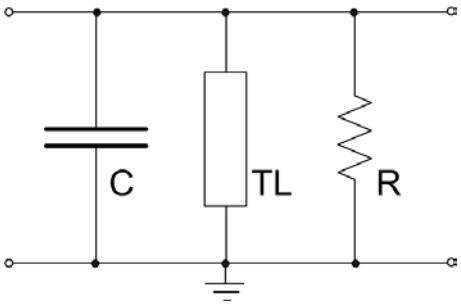


Figure 3.5: Resonator consisting of a capacitor, transmission line and resistor in parallel

The phase difference due to the electrically long coaxial resonator, is presented by a transmission line. As the coaxial resonator is short-circuited to the casing, the transmission line in circuit model is also short-circuited. A resistor is placed in parallel with the capacitance and the transmission line to model the finite unloaded quality factor (discussion of unloaded quality factor follows in section 3.7) of the coaxial cavity.

## 3.5 Concise Design Procedure for Physical Dimensions of Diplexer

The design of the diplexer model is divided into two main structures. These are the two bandpass filters with the specified frequency bands as given in section 2.3.1. Each of these bandpass filters is also divided into its key building blocks. These key building blocks are designed to meet the criteria set by the coupling coefficient, loaded quality factor and resonant frequency of the resonator. The characteristic impedance of the resonator should equal 77 Ohm. Once the dimensions are found it is used as the initial dimensions for constructing the diplexer by placing the

building blocks in cascade. As the methodology for obtaining these dimensions is identical for both of the two filters, the calculation is shown for one of the filters only.

Firstly, the dimensions for an individual resonator that will result in a characteristic impedance of 77 Ω are determined. The design reason behind this specific value, follows in section 3.6.1. This dimension is identical for frequency bands 1 and 2, as the impedance only depends on the ratio of the radius of the resonator to the width of the surrounding vacuum cavity [2]. Secondly, the resonator length is determined that will result in the desired resonance frequency. The length of each of the resonators for the two bandpass filters will differ slightly due to the slight difference in centre frequency.

In the two bandpass filters, the size of the vacuum cavity and the ratio of the radii of the cylinders will be kept the same throughout the design of the diplexer. This is to minimise the time and cost related to manufacturing the diplexer. If the radii of the resonators are identical, one size of an aluminium rod can be be used for all of the resonators, cutting it to length according to the frequency band.

Irises (apertures) are placed between the adjacent coaxial resonators in order to control the coupling. The width and height of these irises are then determined for a predefined coupling coefficient. As a fourth order diplexer is to be designed, the following coupling coefficients require implementation, namely $k_{12}$ and $k_{23}$. For a fourth order filter, $k_{12}$ will equal $k_{34}$ as a result of symmetry.

The loaded quality factor can be varied by altering the distance between the resonator nearest to a port and the external coupling element. An SMA connector is connected to the external coupling elements.

### 3.5.1 Final Implementation of Diplexer

After two bandpass filters are obtained, a preliminary diplexer prototype can be constructed by connecting the two input ports of both bandpass filters such that they share a common port. The loaded quality factor will require further adjustment to compensate for the additional loading effects, see section 2.9. A diplexer with

preliminary dimensions, is then obtained. Further tuning of dimensions is required to obtain a diplexer with an optimum response.

## 3.6 Physical Dimensions of Resonators

### 3.6.1 Resonator Dimensions

For a coaxial line, the optimum ratio of outer to inner radius for minimum power loss, is 3.59 [2]. This would result in an impedance of 76.7 Ω for an air dielectric.

The coaxial resonator is modelled as a coaxial line with a circular inner conductor and a square outer conductor. The characteristic impedance of the coaxial resonator is determined by the ratio of the outer- to the inner radius. If both the outer- and inner radii are increased while the ratio remains constant, the impedance will stay constant [2]. When the outer radius is increased while retaining the ratio of the radii, resistive losses decreases and unloaded quality factor, increases [2]. As an initial starting point, a minimum radius of 4.5 mm for the aluminium cylinder is chosen. A cavity is still required to be drilled to a certain depth and still leave ample space for a tuning screw to be able to extend into. The possible effect of the tuning screw extending at an slight angle to the cylinder, is to be considered. If a long extension of tuning screw into cylinder is required, an inaccuracy in the manufacturing, could lead to the tuning screw being short-circuited at the inner side of the resonator.

For the experiment of investigating the effect of the radius of the square outer conductor, parameter $A$, on the characteristic impedance of the coaxial resonator, the dimensions of the CST model are defined as in Fig. 3.6 (for a given inner conductor radius of 4.5 mm). The height of the inner circular conductor is taken as an initial starting point as an electrical length of 80° (as discussed in section 3.3.2 that the electrical length of resonator should be less than 90°). The difference in length between the inner and outer conductors, (parameter $V$) are taken as an initial value of 6 mm. This is to ensure capacitance between the end of the inner conductor and the roof of the resonator, see section 3.4.

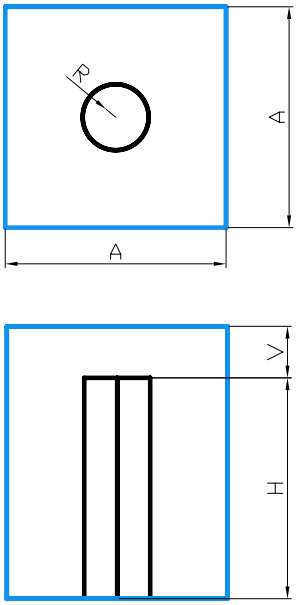


Figure 3.6: Top and front view of coaxial resonator. $A$ is the width of the square vacuum cavity and $H$, is the height of the aluminium cylinder. $V$ is the distance between the resonator and roof of cavity. $H = 33.4$ (electrical length of 80°). Dimensions are in mm.

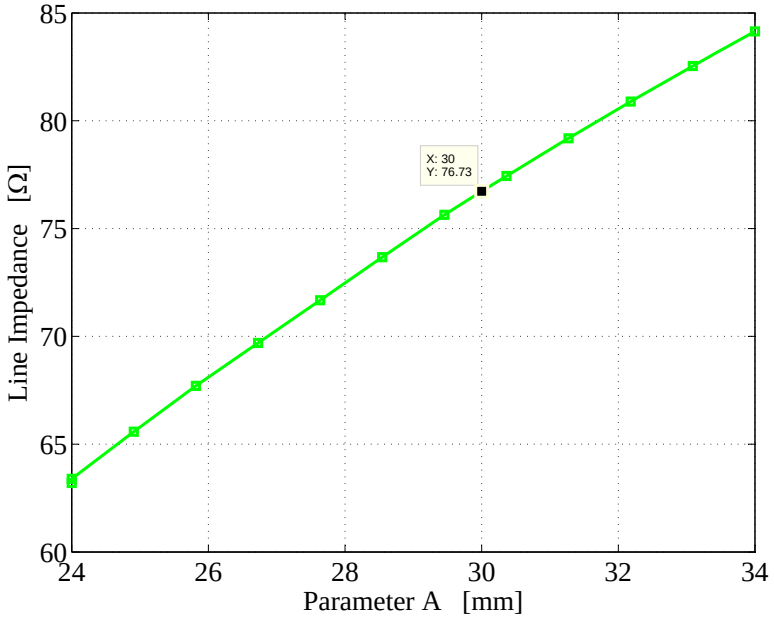


Figure 3.7: Characteristic impedance as function of parameter $A$ with $R$ constant. Dimensions are in [mm]: $H = 33.41$, $R = 4.5$, $V = 6$, $A = 24 \rightarrow 34$.

From the above simulation it is clear that the impedance increases almost linearly with an increase in width of the vacuum cavity. This will hold true as long as the radius of the aluminium cylinder is kept constant. The impedance parameter sweep is shown in Fig. 3.7. In order to obtain an approximate impedance of 76.7 Ω for parameter $R$ equal to 4.5 mm, dimension $A$ is chosen as 30 mm.

The relation between outer and inner radius is mathematically defined in Eq. 3.1 for a square outer conductor and Eq. 3.2 for a circular outer cnductor [2]. Definitions of parameter $a$ and $b$ are given in Fig. 3.8a and Fig. 3.8b, where $b$ and $a$ are the outer and inner radii of the coaxial resonator, respectively.

$$Z_o = \frac{60}{\sqrt{\epsilon_r}} \ln \frac{1.0787b}{a} \quad [\Omega] \tag{3.1}$$

$$Z_o = \frac{60}{\sqrt{\epsilon_r}} \ln \frac{b}{a} \quad [\Omega] \tag{3.2}$$

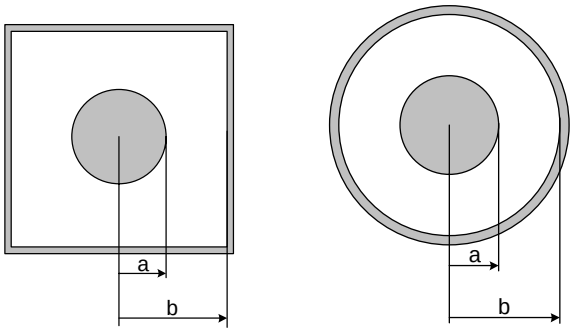


(a) Coaxial resonator with square outer conductor.

(b) Coaxial resonator with round outer conductor.

Figure 3.8: Parameter $a$ and $b$ for a coaxial resonator for determining impedance [2].

A further limitation on the physical size of the cavity also needs to be taken into consideration. According to Ramo et al [23], the lowest-order mode that can propagate on a coaxial line is the TEM wave. A coaxial line can however also support TE and TM waveguide modes [17]. If unwanted higher modes propagate it will lead to the superposition of the different modes with their respective different propagating constants [17].

For prototype 2 (see Fig. 3.29), parameter $a$ and $b$ equals 4.5 and 16.2 mm respectively. An approximate equation [17] for the cutoff wavenumber, $k_c$, is given in Eq. 3.3.

$$k_c = \frac{2}{a+b} \tag{3.3}$$

The cutoff frequency of $TE_{11}$ [17] is found from Eq. 3.4.

$$f_c = \frac{c \cdot k_c}{2 \cdot \pi\sqrt{\epsilon_r}} \tag{3.4}$$

### 3.6.2 Determining the Length of Resonator

In determining the dimension of a resonator that will result in a specified characteristic impedance, the length of the coaxial resonator is insignificant. This is due to the impedance depending only on the ratio of the radii (Eq. 3.1).

The resonator length is chosen to ensure resonance at the two predetermined centre frequencies. On account of a transmission line resonating at $\frac{\lambda}{4}$ of the centre frequency, an initial resonator length was taken as 90°. Fig. 3.9 illustrates the effect of sweeping parameter $V$ from 2 to 14 mm. The length of the resonator was also swept for a number of points to illustrate its effect on the frequency. From the simulation results, it is concluded that the electrical length at which the resonator resonates, is less than a quarter of a wavelength. This is in correlation with the theory of a combline configuration as discussed in section 3.3.2.

The effect of increased capacitance on the resonating frequency, is also investigated. As parameter $V$ is increased, capacitance will decrease. This mathematical relation is shown by Eq. 3.5 [24], where variable $d$ is the distance between plates (in this case the roof of the cavity and the metal cylinder, parameter $V$), $A$ the area (in square metres) of the plates and $\epsilon$ the relative permittivity.

$$C = \epsilon \frac{A}{d} \tag{3.5}$$

As parameter $V$ increases, the capacitance decreases. This results in an increase in frequency of mode 1 of resonator. Pozar [17] states that a microwave resonator can be modelled as an RLC lumped element model. For a parallel RLC resonator, the resonant frequency can be determined by Eq. 3.6, where L is the inductance [Henry] and C the capacitance [Farad].

$$\omega = \frac{1}{\sqrt{L \times C}} \tag{3.6}$$

From Eq. 3.6 it is clear that as the capacitance increases, the resonating frequency will decrease. This is illustrated in Fig. 3.9.

Eventually, as parameter $V$ increases, the frequency of mode 1 settles to a constant frequency. When Fig. 3.4 is investigated, it is seen that as the tuning screw is tuned, the capacitance from the coaxial resonator to the external coupling element or sideways to the wall of the cavity, remain constant. If the tuning screw is removed, capacitance between the roof of cavity and cylinder will be extremely small. Consequently this constant capacitance (as mentioned above) will dominate. As parameter $V$ is increased, the frequency will tend to settle as the constant capacitance starts to dominate.

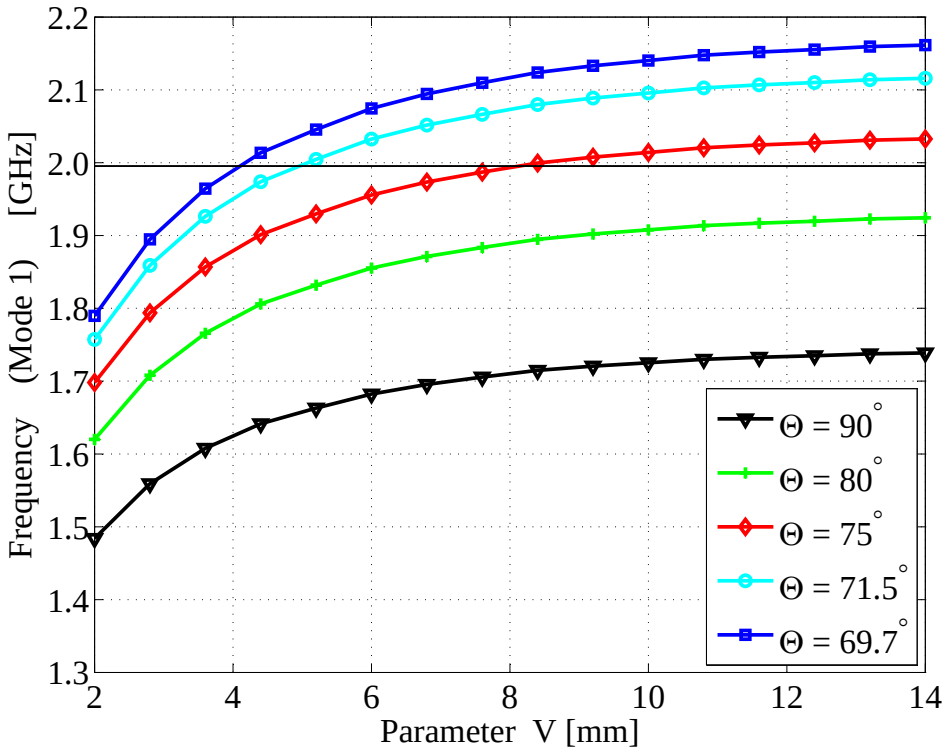


Figure 3.9: Frequency response of mode 1 as a function of parameter $V$ and $H$. Dimensions in [mm]: $A = 30$, $R = 4.5$, $H = 90° \rightarrow 69.7°$, $V = 2 \rightarrow 14$. An electrical length of 71.5° is approximated as 30 mm.

Ideally the resonator length should be chosen such that parameter $V$ results in a steep gradient in the frequency (Fig. 3.9) at the desired frequency of 1.995 GHz for the lower frequency band filter. From Fig. 3.9 the length of the resonator is taken as 71.5° at the resonating frequency. An electrical length of 71.5° corresponds to an approximate resonator length of 30 mm for the resonator for the lower frequency band filter. For the upper frequency band filter, the resonator length is approximately 27 mm. This will ensure that when the tuning screw is added to the configuration and adjusted, a wide range of frequencies can be obtained due to the tuning screw having the same effect of increasing the capacitance (therefore decreasing parameter $V$. If a point on the curve is chosen such that the gradient is very near zero, the sensitivity of the tuning screw enabling the tuning of the frequency, is minimised. Also the tuning screw may be short-circuited in the inside of the resonator even well before the centre frequency was ever reached.

## 3.7 Unloaded Q of Resonator

In section 2.8, the unloaded quality factor of a resonator is defined as the ratio of energy stored in fields to dissipated energy [2]. The quality factor is therefore proportional to the diameter of the resonator [2]. In Fig. 3.10, parameter $A$ is swept from 12 to 40 mm.

Increasing the volume will increase the total energy stored. With the increased stored energy comes increased unloaded quality factor.

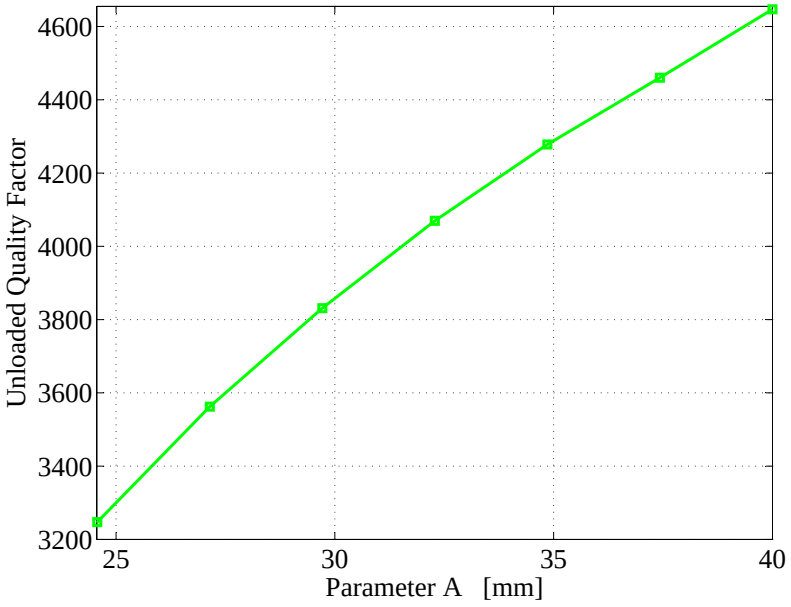


Figure 3.10: Unloaded quality factor as a result of parameter $A$. Dimensions are in [mm]: $H = 30$, $R = 4.5$, $V = 7$, $A = 24.57 \rightarrow 40$.

Extending the tuning screw will also have an effect on the unloaded quality factor of the resonator. This is graphically illustrated in Fig. 3.12. As the length of the tuning screw extends into the resonator, parameter $L$ is increased, the unloaded quality factor of the resonator decreases. This can be contributed to a decrease in volume resulting in less stored energy in the fields. The increase in the metal surface of the metal tuning screw as it extends, will result in an increase in dissipated energy.

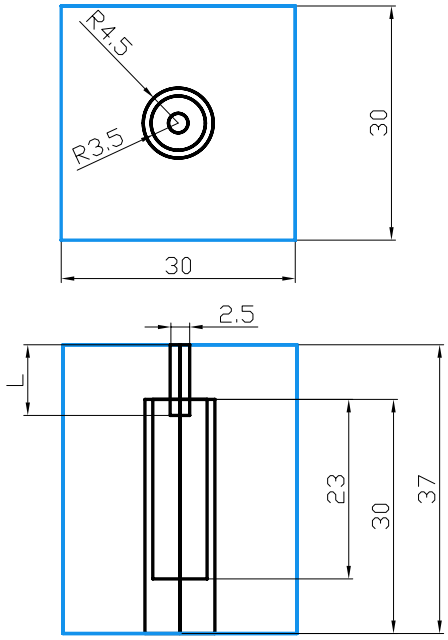


Figure 3.11: Definition of parameters for CST model for the results obtained in Fig. 3.12

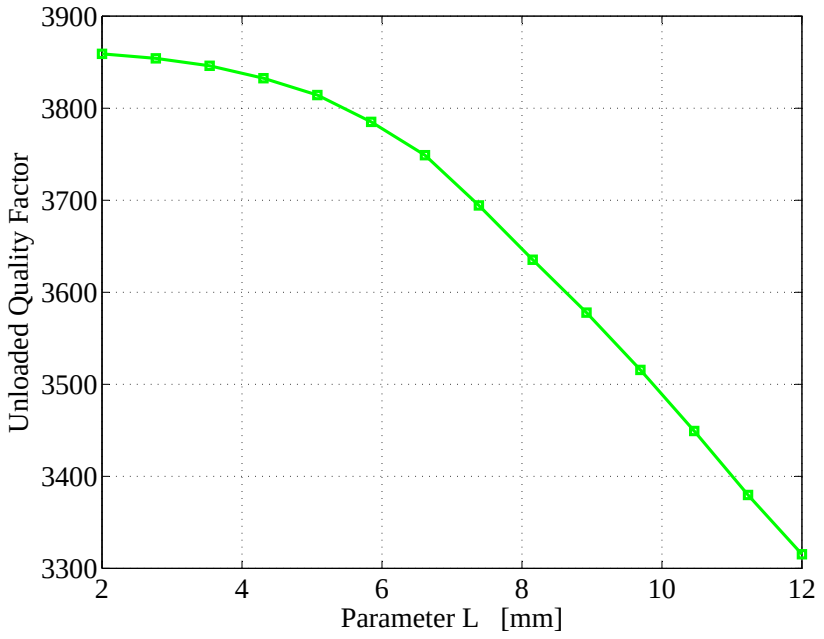


Figure 3.12: Unloaded quality factor as a function of parameter $L$. Dimensions are in [mm]: $A = 30$, $H = 30$, $R = 4.5$, $V = 7$, $L = 2 \rightarrow 12$.

## 3.8 Input/Output Q-factors

When a resonant circuit is connected to external circuitry, the quality factor will decrease due to external loading effects [17]. This is defined as the loaded quality factor $Q_l$ and should be equal to the input/output q-values of the circuit model. The loaded quality factor can be calculated by CST Design Studio by making use of its *Filter Macro*. The mathematical relation between loaded quality factor and $S_{11}$ is discussed next in section 3.8.2.

### 3.8.1 Group Delay

Group delay, $t_d$ is defined in Eq. 3.7 [25] where

$$t_d(\omega) = -\frac{d\phi}{d\omega} \tag{3.7}$$

$$\begin{aligned} \phi &= \text{phase of } S_{11} && [\text{rad}] \\ \omega &= \text{angular frequency} && [\text{rad}\cdot\ \text{s}^{-1}] \\ t_d &= \text{group delay} && [s] \end{aligned}$$

### 3.8.2 Computing $Q_l$ from Group Delay

The loaded quality factor, $Q_l$, can be calculated from the group delay as defined in Eq. 3.8 [26] [8].

$$t_d(\omega_o) = \frac{4Q_l}{\omega_o} \tag{3.8}$$

The relation between the group delay and $Q_l$ is used to optimise the parameters of the diplexer model and thereby obtaining dimensions that would result in the correct loaded quality factor. The optimised normalised loaded quality factor is now required to ascertain parameter $D$, as defined in Fig. 3.13. In Table 3-II and Table 3-III the normalised loaded quality ($\omega_c = 1$, $R_L = 1$), factors and the bandwidth transformed loaded quality factors are given.

Table 3-II: The optimised normalised loaded quality factor ($\omega_c = 1$), bandwidth transformed for filter 1.980 to 2.010 GHz, respectively. Load resistance = 1.

| **Loaded Quality Factor, q** | $\mathbf{q} \times \frac{1}{bandwidth}$ |
|---|---|
| $\mathbf{q}_l$ | $1.052 \times \frac{1}{0.019} = 55.36842105$ |
| $\mathbf{q}_n$ | $1.046 \times \frac{1}{0.019} = 55.05263158$ |

Table 3-III: The optimised normalised loaded quality factor ($\omega_c = 1$), bandwidth transformed for filter 2.170 to 2.200 GHz, respectively. Load resistance = 1.

| **Loaded Quality Factor, q** | $\mathbf{q} \times \frac{1}{bandwidth}$ |
|---|---|
| $\mathbf{q}_l$ | $1.065 \times \frac{1}{0.019} = 56.05263158$ |
| $\mathbf{q}_n$ | $1.046 \times \frac{1}{0.019} = 55.05263158$ |

In Fig. 3.13 parameter definition and configuration for the calculation of $Q_l$ is shown. SMA connectors are connected to the external coupling elements to form the designated input and output ports. The loading effect will be as a result of the coupling between the resonator and the load.

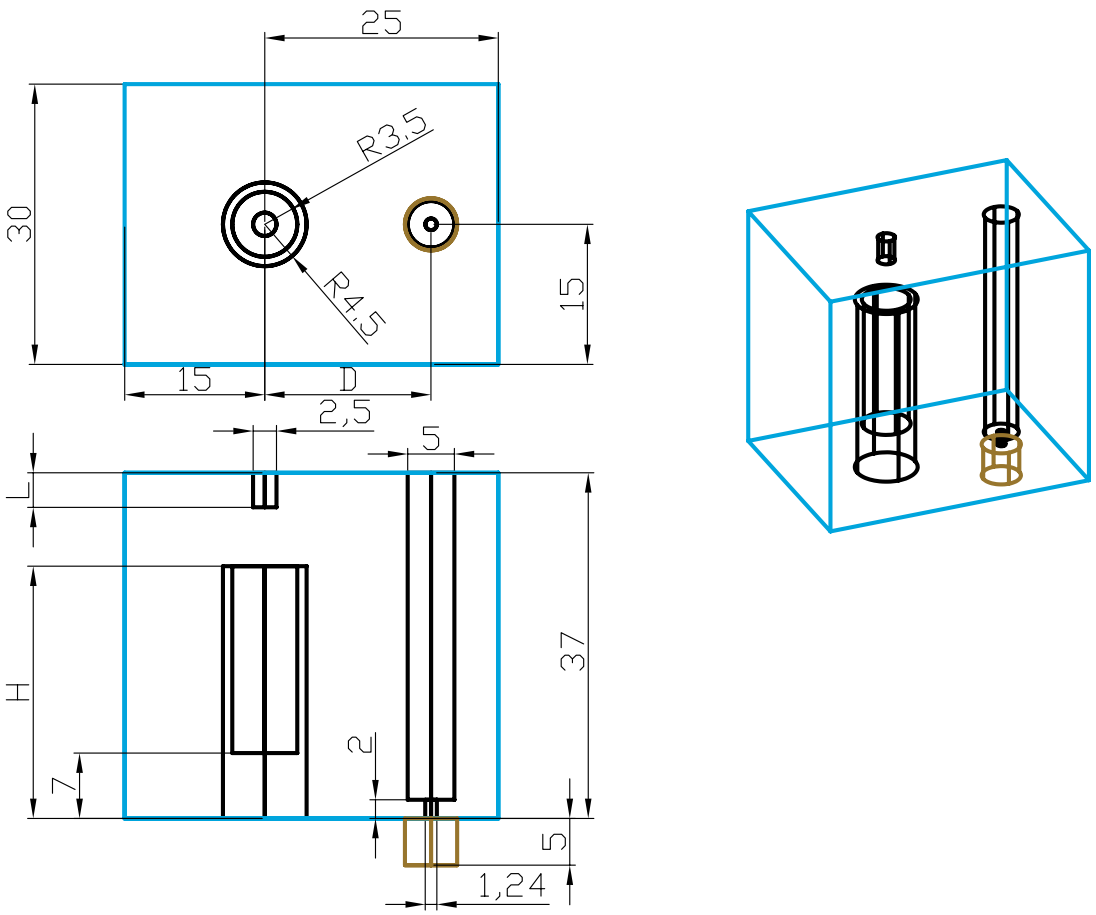


Figure 3.13: Dimensions for computing the loaded quality factor.

It is shown in Fig. 3.14 that the input quality factor is proportional to the distance between the resonator and external coupling element. An increase in parameter $D$ will increase the loaded quality factor. Similarly, a decrease in $D$ will result in a decrease in the loaded quality factor. As the distance $D$ is increased, the volume containing the stored energy of the fields, are increased. Due to this increase in stored energy, the loaded quality factor increases.

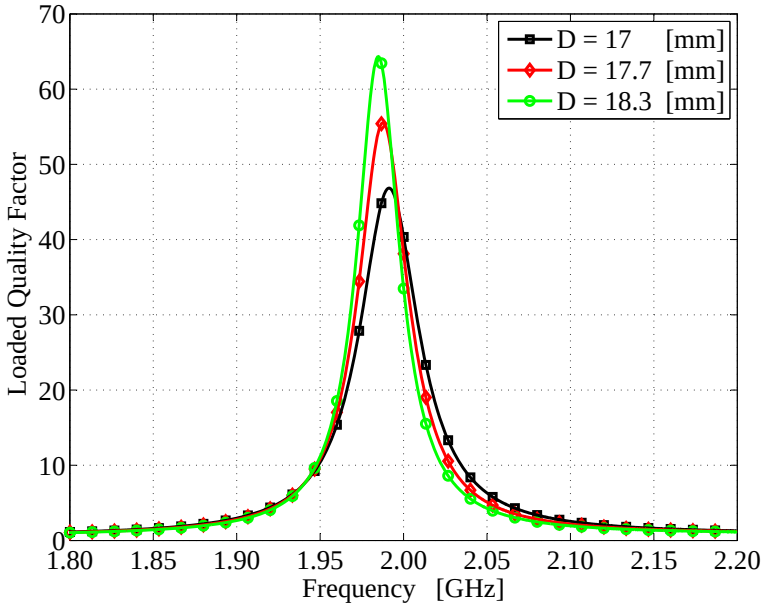


Figure 3.14: Effect of parameter $D$ on the loaded quality factor. An increase in parameter $D$ is proportional to the magnitude of the loaded quality factor. Extending the the tuning screw into the resonator results in a decrease in frequency.

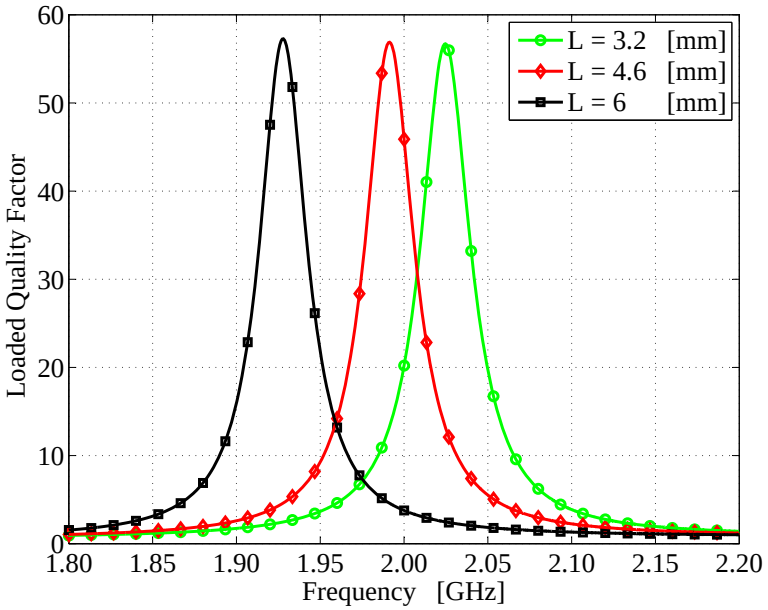


Figure 3.15: Effect of parameter $L$ on the loaded quality factor. The magnitude of the loaded quality factor however remains unchanged.

## 3.9 Coupling Coefficients

The next key structure requiring implementation, is the coupling between the two adjacent resonators at the resonant frequency. The amount of coupling between the resonators will be regulated by placing an iris between the resonators. The dimensions of the iris will be chosen to result in optimised and bandwidth transformed coupling coefficients, as computed in the circuit model, (section 2.7). A graphical illustration of the parameter definition of the CST model that is used to determine the coupling coefficients, is shown in Fig. 3.16.

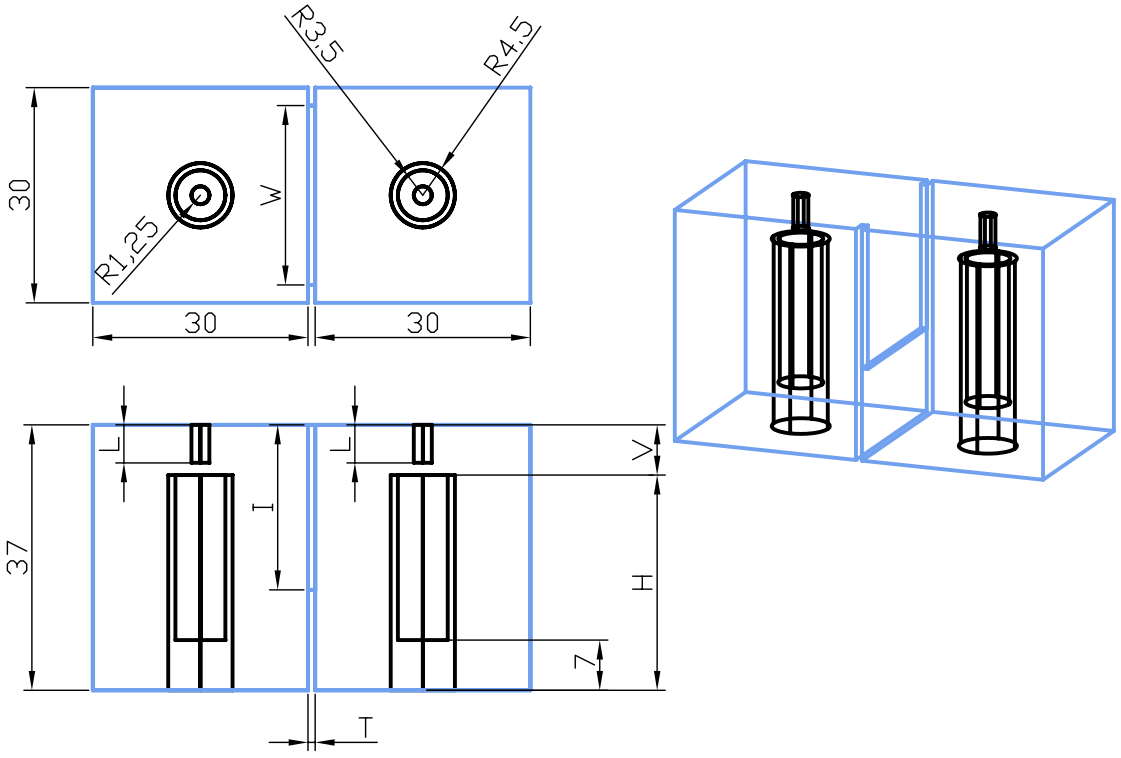


Figure 3.16: Parameter definition in CST for the implementation of the coupling coefficient

### 3.9.1 Eigenmode Method for Determining Coupling

The coupling coefficient, k, can be determined by means of the even and odd mode frequencies, where:

$$\begin{aligned} f_o &= \text{odd mode frequency} && \text{[Hz]} \\ f_e &= \text{even mode frequency} && \text{[Hz]} \\ f_O &= \text{resonant frequency} && \text{[Hz]} \end{aligned}$$

For positive coupling as used in this diplexer design, $f_e < f_o$ [16] [27]. The coupling coefficient can now be defined as in Eq. 3.9 [16]. Frequency of resonance, $f_O$, can be determined by Eq. 3.10 [16].

$$k = \frac{f_o^2 - f_e^2}{f_o^2 + f_e^2} \tag{3.9}$$

$$f_O^2 = \frac{2 \times f_o^2 \times f_e^2}{f_o^2 + f_e^2} \qquad \text{[Hz]} \tag{3.10}$$

CST enables the designer to add a 'watch' for the frequencies of mode 1 and 2 (*3D Eigenmode Result*) if the *Eigenmode Solver* is run. The above mentioned equations can now be implemented in CST's Template Based Post Processing (*0D Results*). The *Eigenmode Solver*'s optimisation function can then be used to determine the correct dimensions that will result in the predefined coupling coefficient as determined in section 2.7.

### 3.9.2 Physical Realisation of $k_{12}$, $k_{23}$ and $k_{34}$ for Filter

The coupling coefficients, $k_{12}$, $k_{23}$ and $k_{34}$ can now be physically realised for the diplexer model. In Table 3-IV, the optimised normalised coupling coefficient ($\omega_c = 1$, load resistance = 1) as used for implementation, is given. Each of these coupling coefficients are to be realised for the two filters.

Table 3-IV: The bandwidth transforming of the optimised normalised coupling coefficient.

| **Coupling coefficient, k** | **k × bandwidth** |
|---|---|
| $\mathbf{k}_{l2}$, $\mathbf{k}_{34}$ | $0.7369 \times 0.019 = 0.0140011$ |
| $\mathbf{k}_{23}$ | $0.5413 \times 0.019 = 0.0102847$ |

The effects of parameters $T$ and $W$ on the coupling coefficient are also investigated. In Fig. 3.17 it is illustrated that an increase in parameter $T$ results in a decrease in the coupling coefficient.

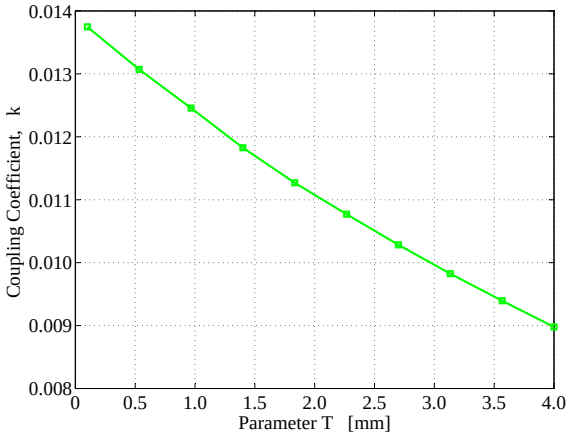


Figure 3.17: Coupling coefficient as a function of parameter $T$. An increase in parameter $T$ results in a decrease in the coupling coefficient. Dimensions are in [mm]: $H = 30$, $I = 23$, $L = 5.65$, $V = 7, W = 23$, $T = 0.1 \rightarrow 4$.

As the distance between the two resonators are increased, less field couple between the resonators. The effect of the width of the iris on the coupling coefficient was also investigated. From Fig. 3.18 it can be seen that the width of the iris is proportional to the amount of coupling. With the increase in the width of the iris, more magnetic field can couple between the resonators, resulting in a higher coupling coefficient.

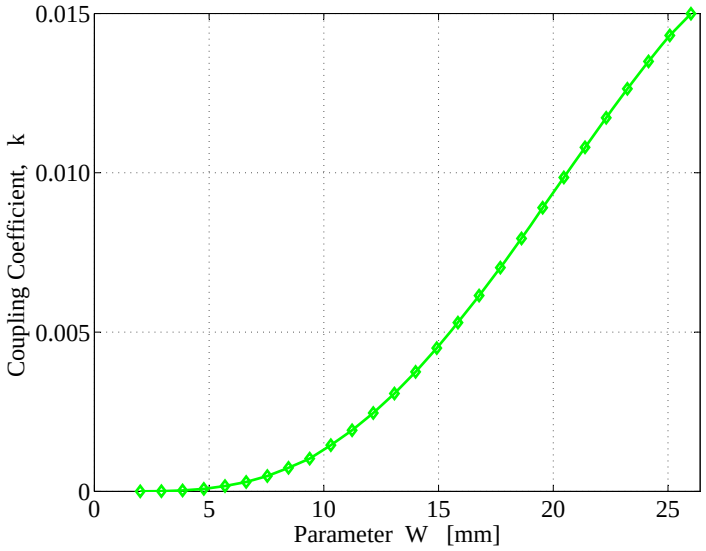


Figure 3.18: Coupling coefficient as a function of parameter $W$. Dimensions are in [mm]: $H = 30$, $I = 23$, $L = 5.65$, $T = 1$, $V = 7$, $W = 2 \rightarrow 26.25$. An increase in parameter $W$ results in an increase in the coupling coefficient.

### 3.9.3 Field Distribution in Resonators

As knowledge of electric and magnetic fields play an integral role in the determining the coupling between resonators and quality factors, distribution of the fields was investigated. At the bottom of the resonator, it is short-circuited resulting in magnetic field dominating. This phenomenon is graphically illustrated in Fig. 3.19a. At the open-circuited end of the resonator, electric fields will tend to dominate as shown in Fig. 3.19b.

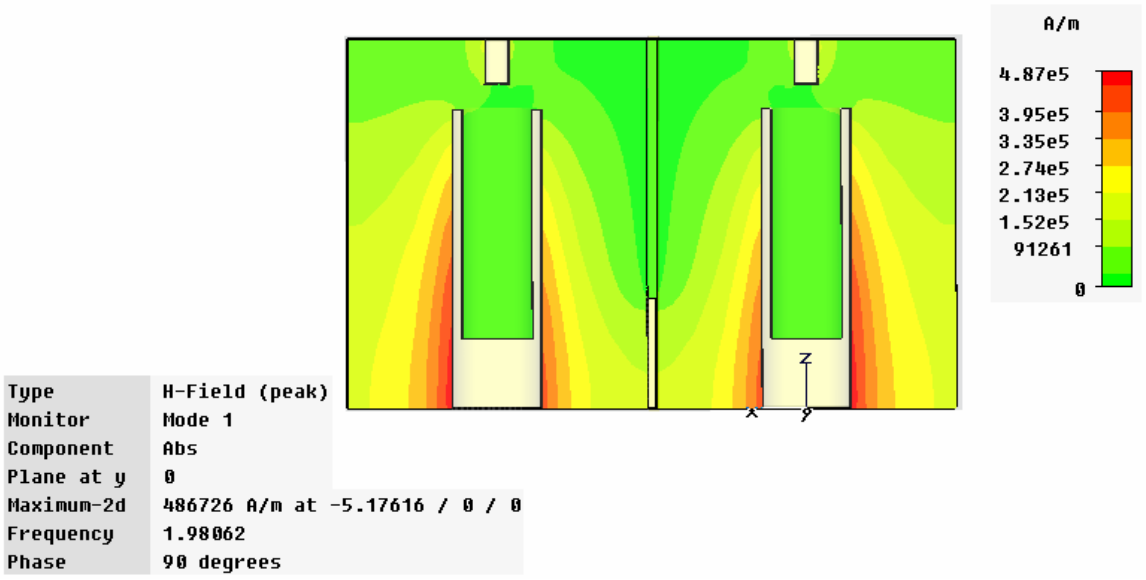


(a) The absolute value of the magnetic field of mode 1 in adjacent resonators. Note the concentration of magnetic field at the short-circuited end of the resonator.

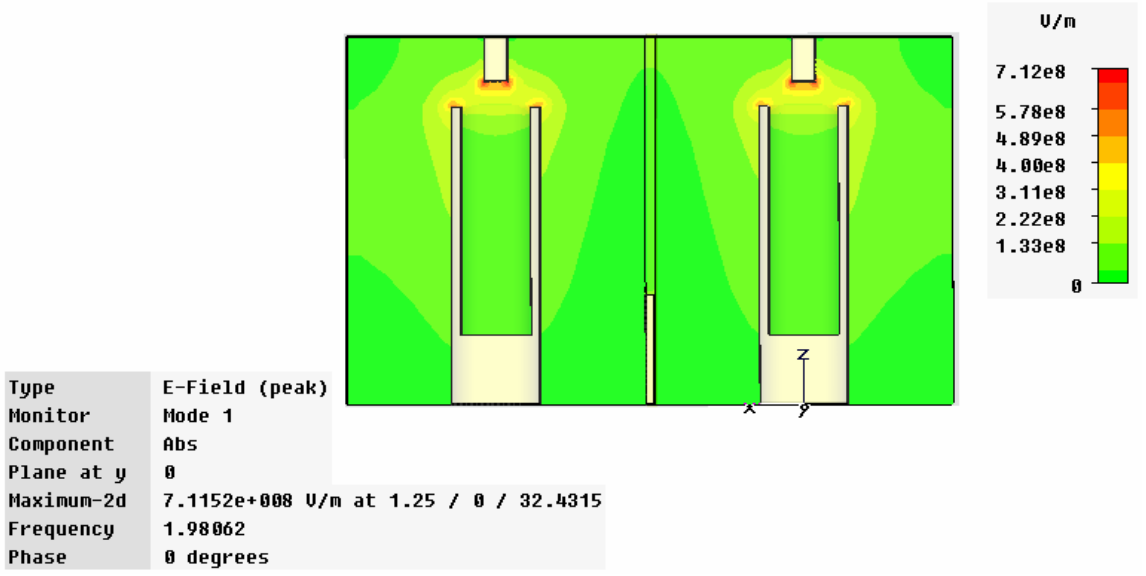


(b) The absolute value of the electric field of mode 1 in adjacent resonators. Note the concentration of electric field at the open-circuited end of the tuning screw.

Figure 3.19: Field distribution in two adjacent resonators

The electric and magnetic field distribution on the plane situated on the face of the iris, are addressed. In Fig. 3.20, the location and definition of where the fields are to be investigated, are illustrated.

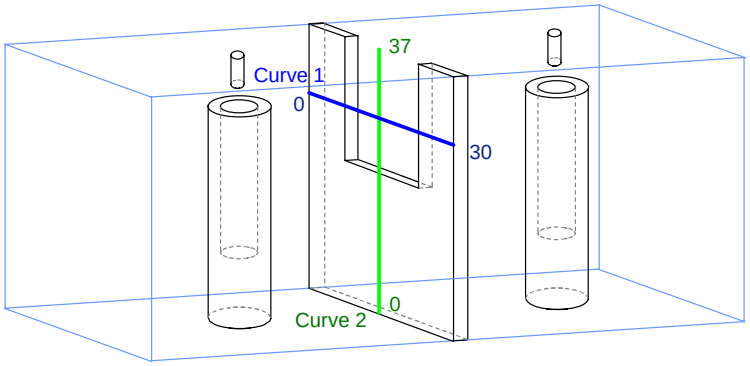


Figure 3.20: Definition of curve location for the investigation into field distribution

The absolute value of the electric field on the face of the iris, is now considered. From Fig. 3.21, it is clear that the largest concentration of the electric field is at the sides of the iris and at the open-circuited coaxial resonator. The exact numerical values of the absolute value of the electric field at location *curve* 1 and 2, are shown in Fig. 3.22a and Fig. 3.22b.

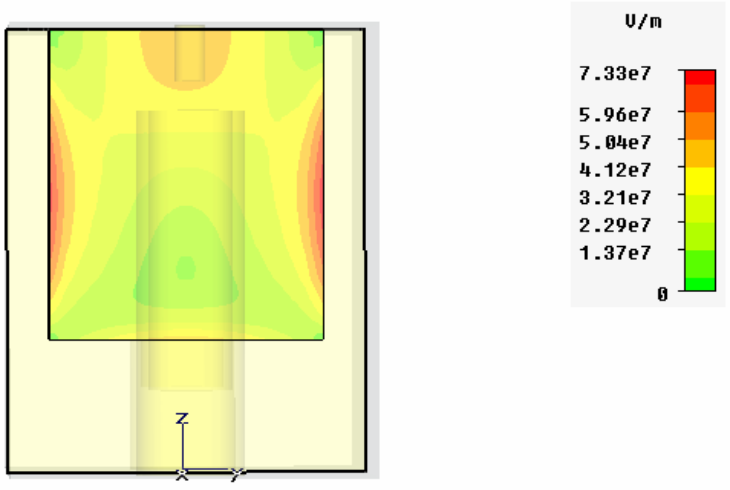


Figure 3.21: The absolute value of the electric field, mode 1 on surface of iris

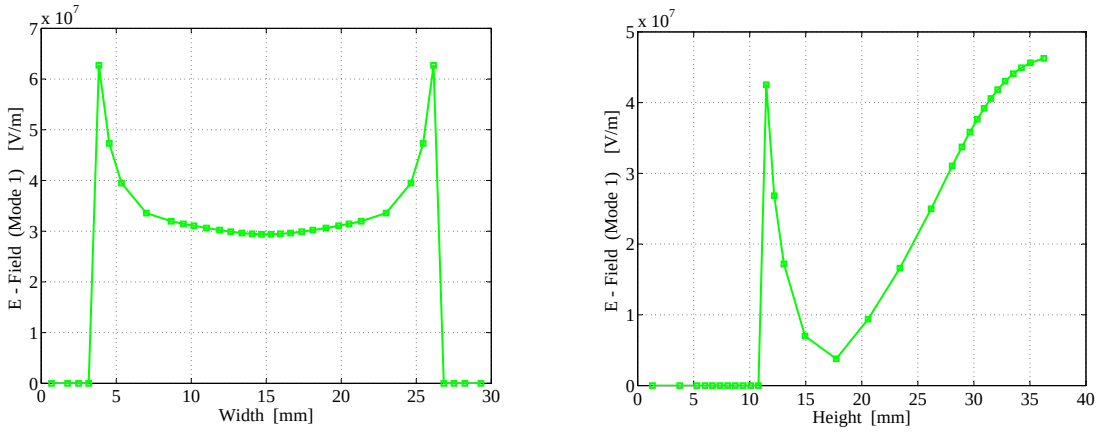


(a) Curve 1 (b) Curve 2

Figure 3.22: Magnitude of the electric field distribution on iris [V/m]

The absolute value of the magnetic field on the face of the iris, is now under investigation. From Fig. 3.23, it is clear that the largest concentration of the magnetic field is at the sides of the iris and at the open-circuited coaxial resonator. The exact numerical values of the absolute value of the magnetic field at location *curve* 1 and 2, are shown in Fig. 3.24a and Fig. 3.24b.

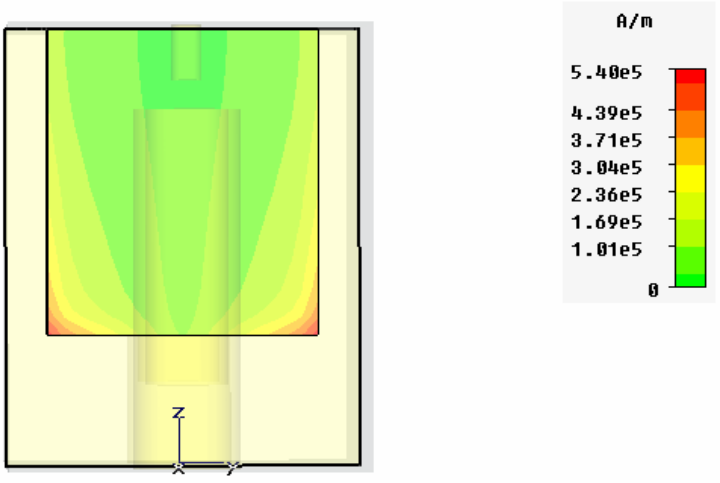


Figure 3.23: The absolute value of the magnetic field, mode 1 on surface of iris

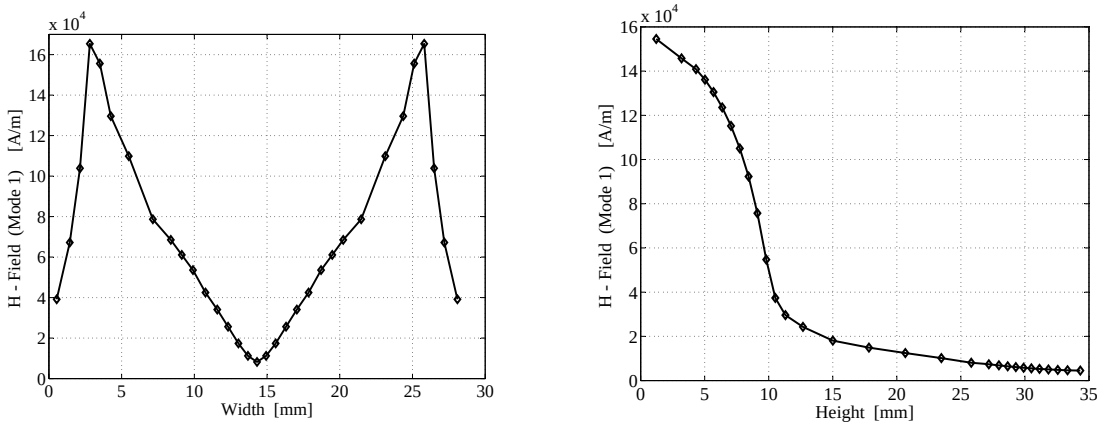


(a) Curve 1 (b) Curve 2

Figure 3.24: Magnitude of the magnetic field distribution on iris [A/m]

## 3.10 Diplexer Prototype

### 3.10.1 Physical Realisation of Common Port Coupling for Diplexer

Once the dimensions for the respective filters are acquired, a diplexer with preliminary dimensions is obtained by placing the key structures in cascade. The two input ports to the filters are now connected as one common input port. As explained in section 2.8, the loaded quality factor, $Q_l$ will require adjustment. This adjustment will be done in the final tuning process, to be discussed in the next section (section 3.11).

## 3.11 Tuning Procedure of Diplexer

In 1951 it was stated by Dishal [20] that any narrowband filter can be described by three types of fundamental variables. These variables are the following:

- couplings between adjacent resonators
- external quality factor
- resonant frequency of each resonator

These three variables will form the basis of the parameter extraction procedure for fine-tuning the diplexer. In the previous sections, preliminary dimensions were obtained to enable the three fundamental variables as mentioned above. A tuning process is now required to adjust the preliminary dimensions to obtain the desired diplexer response. For this specific diplexer model there are 18 non-linear dependant variables that influence the three factors above. As the diplexer tuning process is time-consuming and demand great accuracy, consequently a systematic approach to the tuning process is required. A technique proposed by Ness [8] to utilising the group delay of diplexer to ensure the correct loaded quality factors, coupling coefficients and resonant frequencies, will be used.

### 3.11.1 Tuning by means of MWO and CST

The circuit model developed in section 2.5 will be viewed as the ideal model in the sense that it has the desired response for the diplexer. Multipliers will be synthesised for the 18 variables and defined in the Microwave Office (MWO) model. Each of these variables can be related to a particular physical dimension in the CST model. The above mentioned 18 variables in the MWO circuit model and their corresponding dimension in CST physical model, are shown in Table 3-V. Dimensions of the CST model are defined in Fig. 3.25.

Table 3-V: The 18 variables of the diplexer in the MWO model and the corresponding CST model. The $l$ and $u$ denotes lower and upper. Parameters $q$ is the loaded quality factor, $k$ the coupling coefficient and $f$ the resonant frequency of the resonator.

| **MWO Circuit Model** | **CST Physical Model** |
|---|---|
| $q_n$ $q_1$ | $D_n$ $D_1$ |
| $f_4$ | $L_4$ |
| $k_{34}$ | $I_{34}$ |
| $f_3$ | $L_3$ |
| $k_{23}$ | $I_{23}$ |
| $f_2$ | $L_2$ |
| $k_{12}$ | $I_{12}$ |
| $f_1$ | $L_1$ |

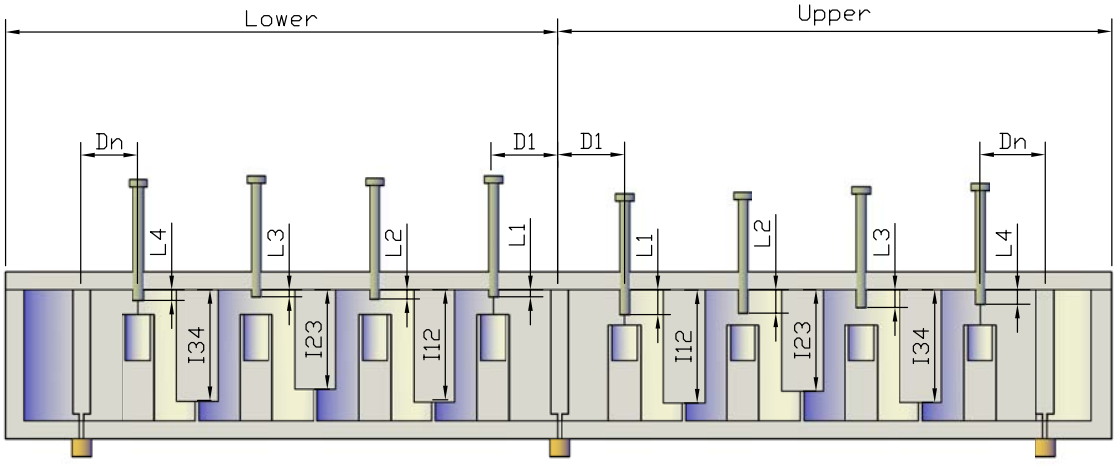


Figure 3.25: Parameter definition of CST physical model

The MWO synthesised multipliers are initially set to one. They are then multiplied with their corresponding k,q or resonant frequency. As a parameter extraction

will be carried out, it is important to keep the synthesised variables and their corresponding MWO k, q or frequency multipliers apart. This will ensure that the CST model can be accurately tuned, depending on the value of the extracted synthesised value of the multipliers. After the s-parameters are obtained in CST, they are exported (in *Touchstone* format) to the MWO circuit model. After the s-parameters are imported into MWO, the group delay of both the imported s-parameters and the circuit model is computed. By means of MWO's optimisation function, the values of the multipliers in the circuit model are then optimised such that the two group delay functions are equal. Synthesised multipliers are then extracted from the MWO model.

A value of one for a certain parameter would indicate that for that specific physical dimension, the ideal circuit model equals the physical model. For a value smaller than one, it would mean that the circuit model parameter is larger than the corresponding physical model. As a result, the corresponding parameter in the CST model has to be adjusted. This does however not necessarily mean that the corresponding dimension of the parameter must be increased. This is shown in Table 3-VI.

Table 3-VI: Result of parameter extraction on CST dimensions

| **MWO Model** | **Extracted constant** | **CST Model** |
|---|---|---|
| Loaded q | $< 1$ | increase D |
| | $> 1$ | decrease D |
| Frequency | $< 1$ | decrease L |
| | $> 1$ | increase L |
| Coupling Coefficient | $< 1$ | increase I |
| | $> 1$ | decrease I |

The tuning of the diplexer starts with the systematic tuning of the resonator $i$ nearest to a port. In the MWO model, short-circuit resonator $i + 1$. Inverter

between resonator $i$ and $i + 1$ will result in resonator $i$ seeing an open-circuit. In the CST model, the same principle can be applied by short-circuiting resonator $i + 1$ by extending the tuning screw until it makes contact with the resonator. This will lead to additional simulation time due to an increased number of mesh cells. Alternatively, only the section containing the port and resonator can be simulated. For the next section, the resonator section is then added. This is graphically illustrated in Table 3-VII and Table 3-VIII.

Table 3-VII: Centre sections of the CST model for the fine tuning of diplexer. The resulting group delay is shown on the right. Note that each resonator will result in a resonating frequency. Group delay is computed in [ns].

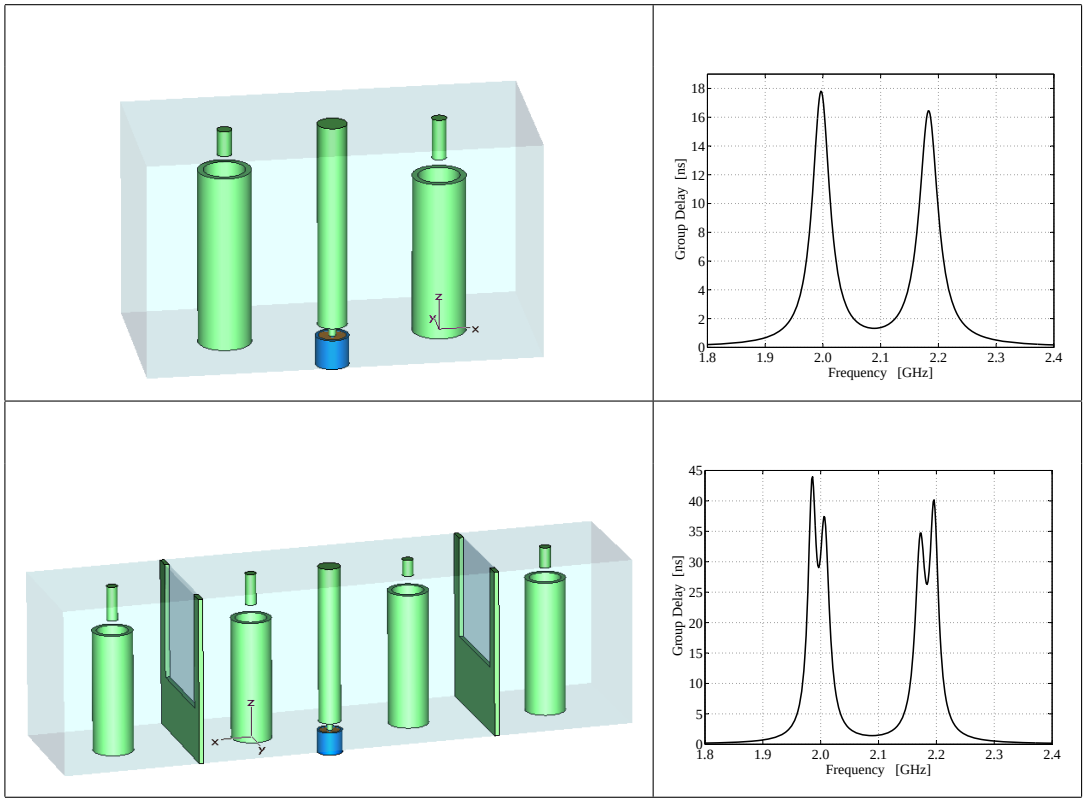

Table 3-VIII: Sections of the CST model for the fine tuning of the diplexer. This process is repeated for both the upper and lower band frequency part of the diplexer. Resulting group delay is shown on the right. Note that each resonator will result in a resonating frequency. Group delay is in [ns].

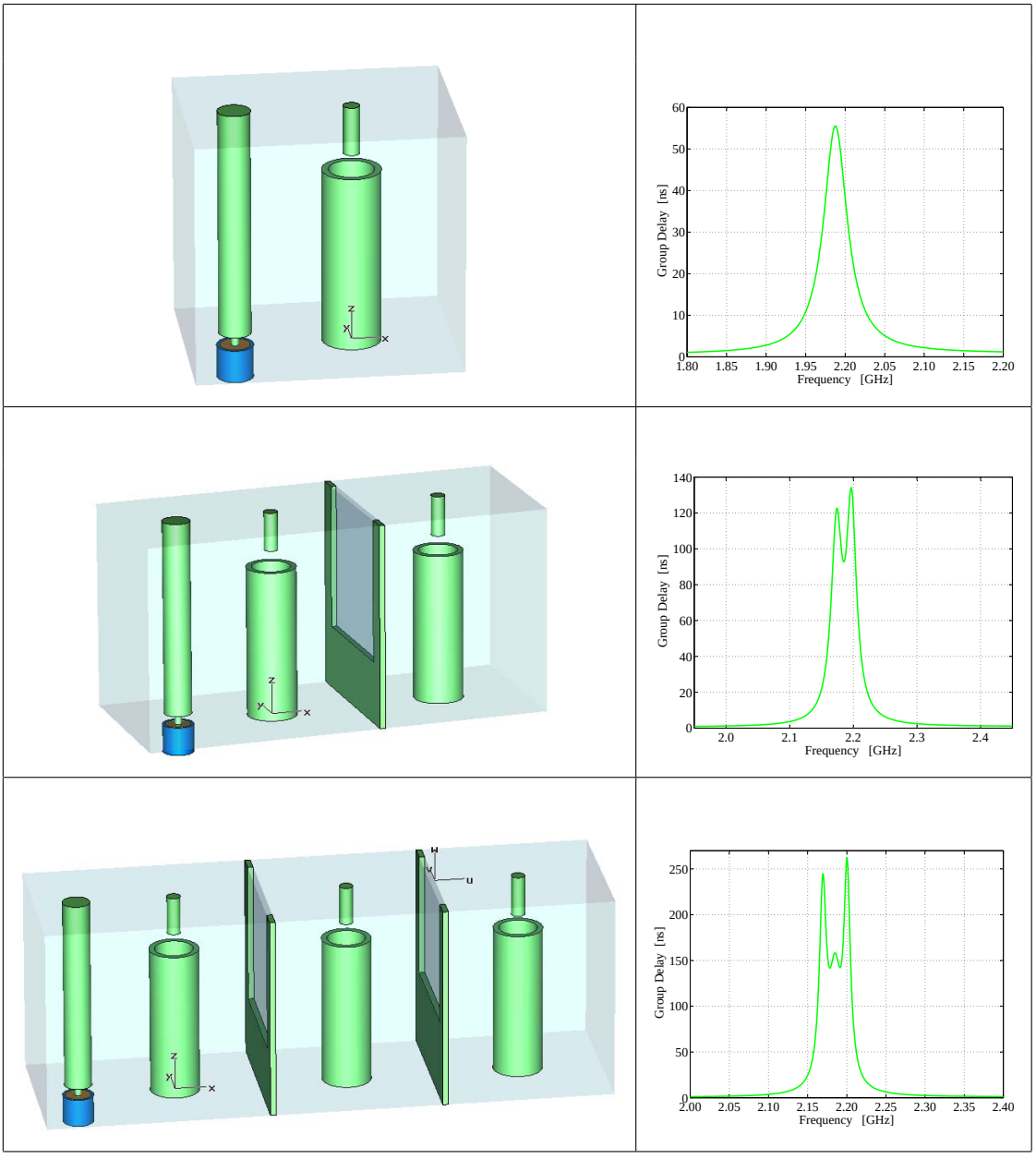

## 3.12 Final Diplexer Prototype

A final diplexer is obtained after the tuning process is carried out. The final dimensions for the diplexer prototype one as simulated in CST, is given in Fig. 3.26.

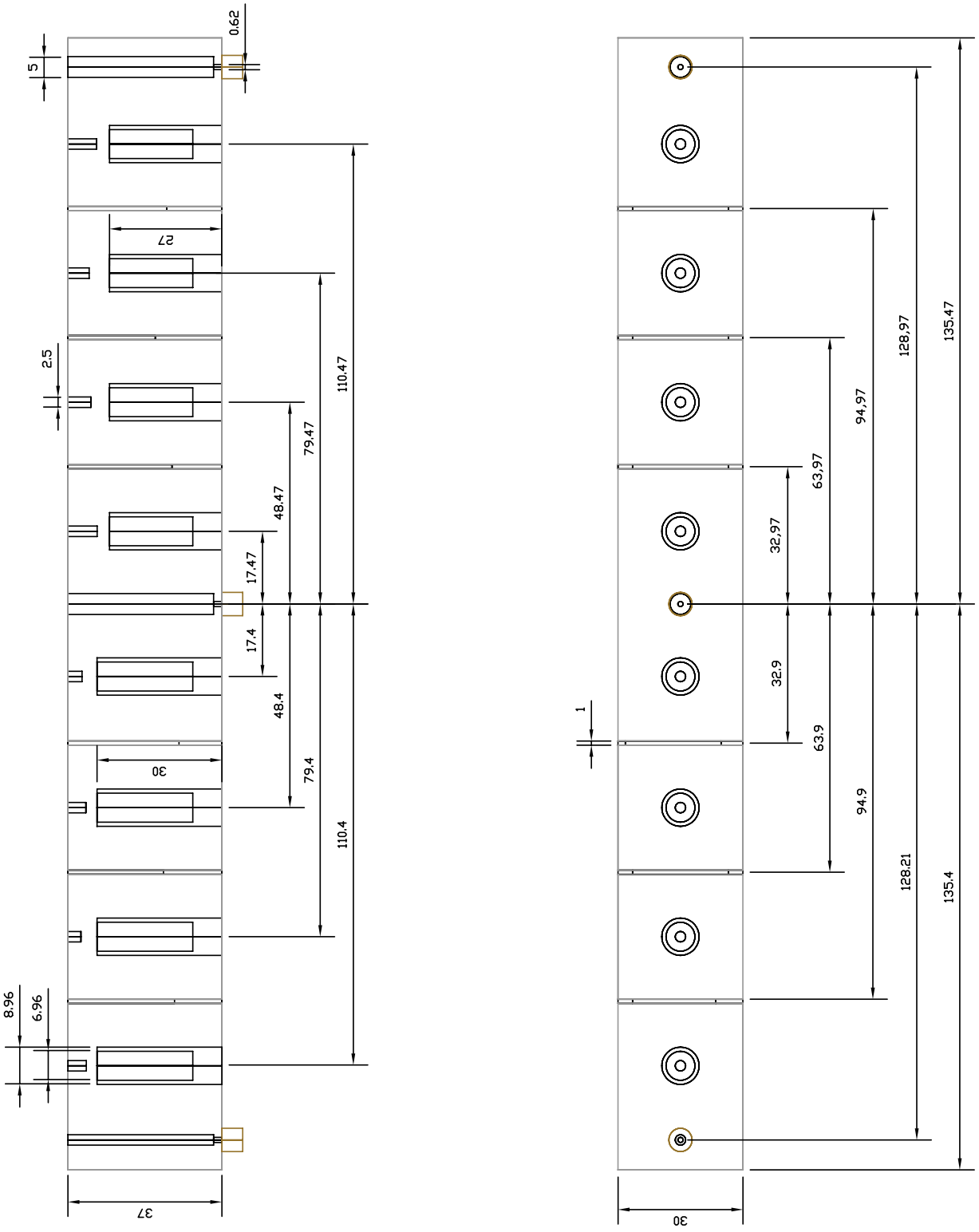


Figure 3.26: Front and top view of diplexer prototype one as implemented in CST. Resonators for lower and upper frequency band equals 30 mm and 27 mm, respectively.

## 3.13 Modification of Prototype for Manufacturing Purposes

The prototype designed in the preceding sections can be modified slightly to enable a much simpler manufacturing process. Instead of using square vacuum cavities, circular cavities can be used. This would result in a less time-consuming manufacturing process. Circular cavities can now be directly drilled out of a solid aluminium block. For prototype one, very accurate and consecutive milling would be required. It would also be impossible to ensure that corners are exactly 90°. Consequently, prototype two will be a more accurate representation of the CST diplexer model.

Resonators are to be implemented by utilising aluminium rods (with cavities drilled inside to a certain height), fastened at the face opposite of the tuning screws. This decreases the cost, time and complexity of the manufacturing. A disadvantage to this process is that if resonators are not correctly positioned, the impedance of the resonator will change. A thin lid of aluminium is fastened to the roof of the diplexer. A photograph of the final manufactured diplexer (prototype two) is shown in Fig. 3.27.

Figure 3.27: Top view of diplexer prototype 2 with roof and tuning screws removed

Another option for the manufacturing process would be to mill the diplexer from a solid piece of aluminium. The disadvantage of this process is that a CNC machine is needed.

A top view of diplexer, together with dimensions, is illustrated in Fig. 3.28. A sectional front view with dimensions, is shown in Fig. 3.29. The outer radii of the resonators are 4.5 mm. Tuning screws are placed above each iris to enable precise setting of the coupling between the resonators. If the coupling between the adjacent resonators is too small, it can be increased by extending the tuning screw into the cavity. Tuning screws above each resonator (as in the CST model) will assist in the tuning process of the resonant frequency of each resonator.

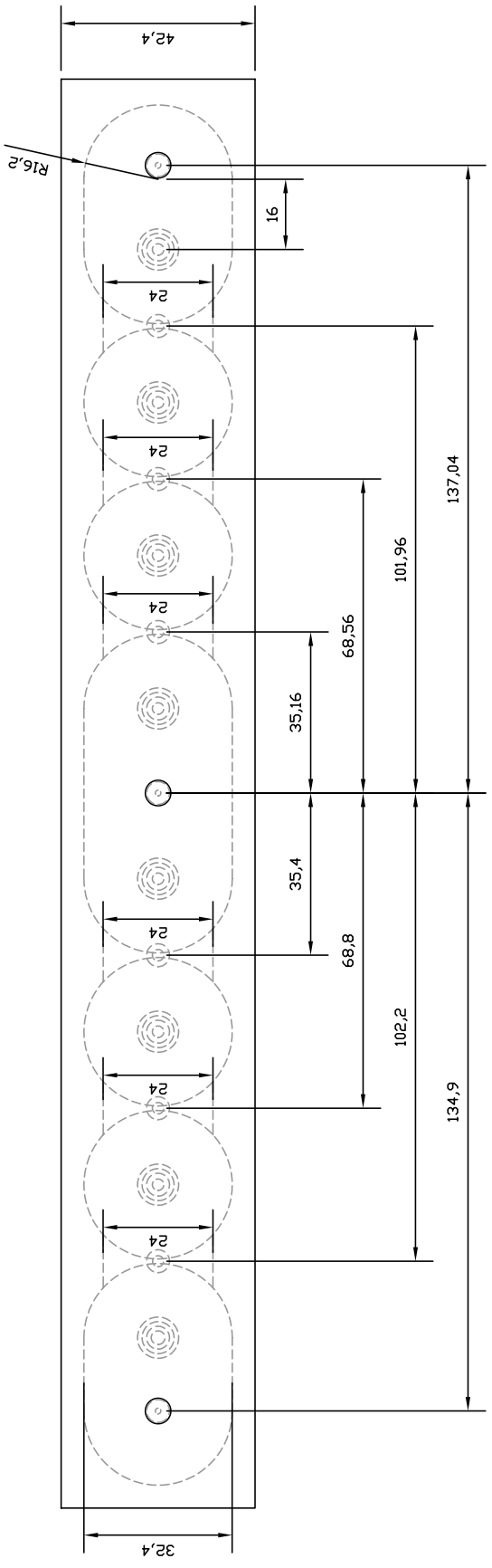


Figure 3.28: Top view of diplexer prototype 2

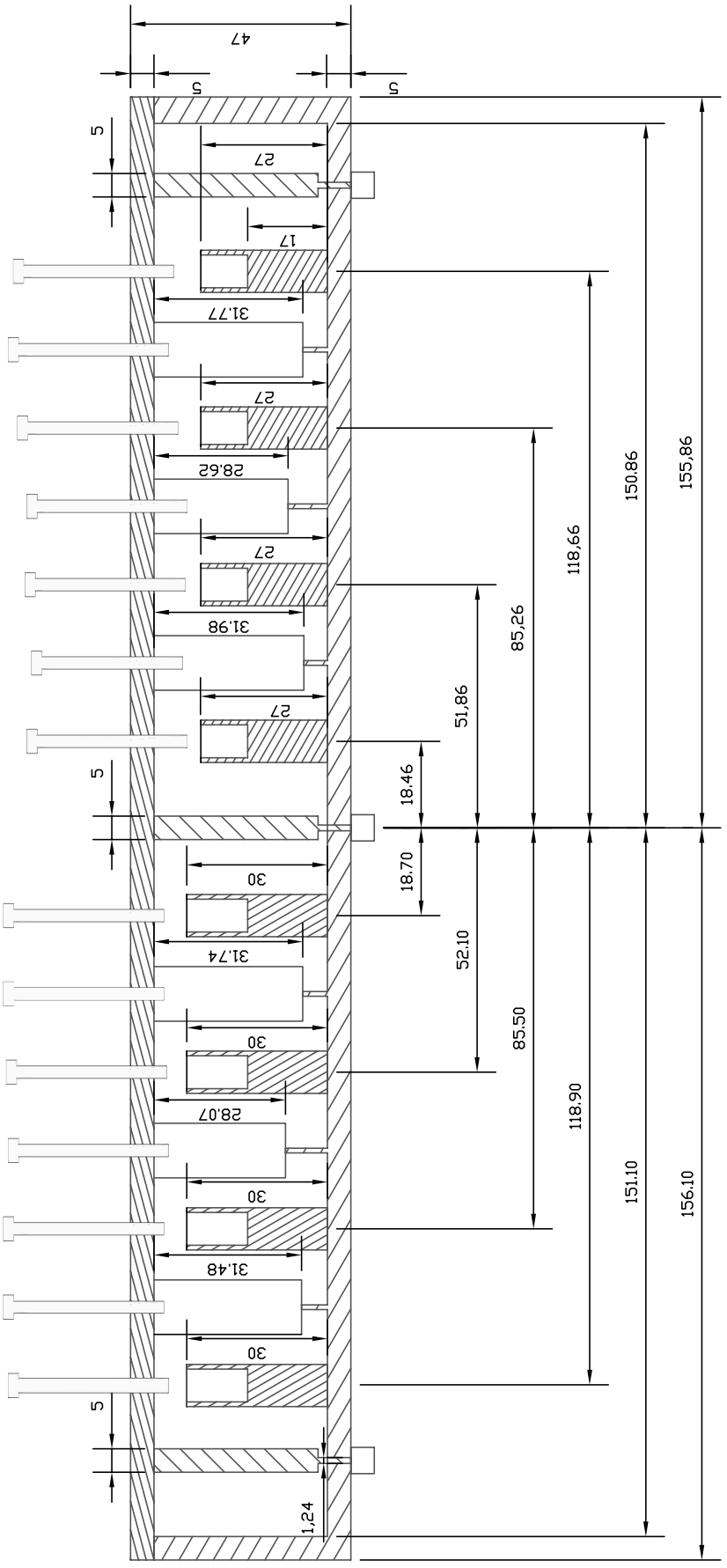


Figure 3.29: Front section view of diplexer prototype 2. Radii of resonators equal to 4.5 mm.

## 3.14 Measurement Procedure

### 3.14.1 Measurement Configuration

Once constructed, a final tuning of the diplexer can be done by means of a VNA (vector network analyser). The diplexer was connected to a calibrated *Agilent 8510* VNA. Quick tuning of the diplexer was done by turning the tuning screws and setting the resonant frequencies and coupling while measuring the magnitude of $S_{11}$ on the VNA. It was found that for the three irises in the lower frequency band, the coupling was already slightly larger than anticipated. Therefore, the tuning screws were redundant and as a result, removed. The coupling between the resonators can only be increased by means of extending the tuning screws. A more systematic approach together with a MATLAB graphical user interface (GUI) written to aid in the tuning process, is explained in Appendix A. The final diplexer together with the *Agilent 8510* VNA is shown in Fig. 3.30.

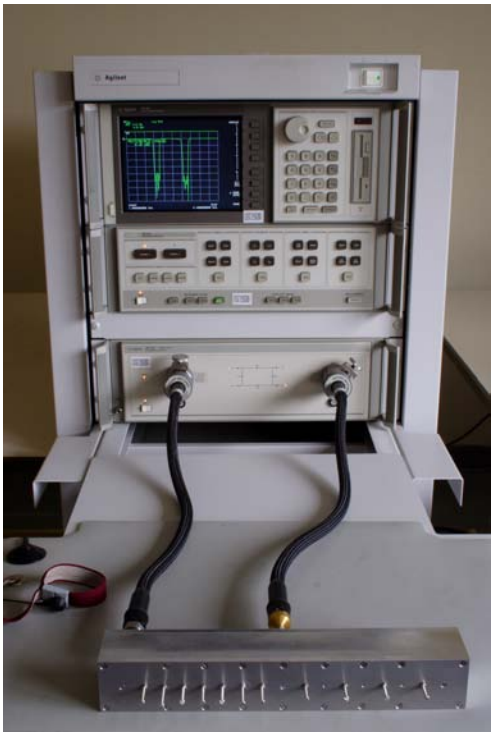

Figure 3.30: Measurement configuration

### 3.14.2 Results

The designed diplexer have better than 18.83 dB and 21.52 dB return loss in the lower and upper passband respectively. An insertion loss of 0.58 dB and 0.61 dB was measured for the lower and upper passband respectively. The isolation at 2.01 GHz is 74.5 dB and at 2.17 GHz it is 81.5 dB. The final measurement of $S_{21}$ and $S_{11}$ compared against $S_{21}$ and $S_{11}$ of the circuit model, are shown in Fig. 3.31 and Fig. 3.32.

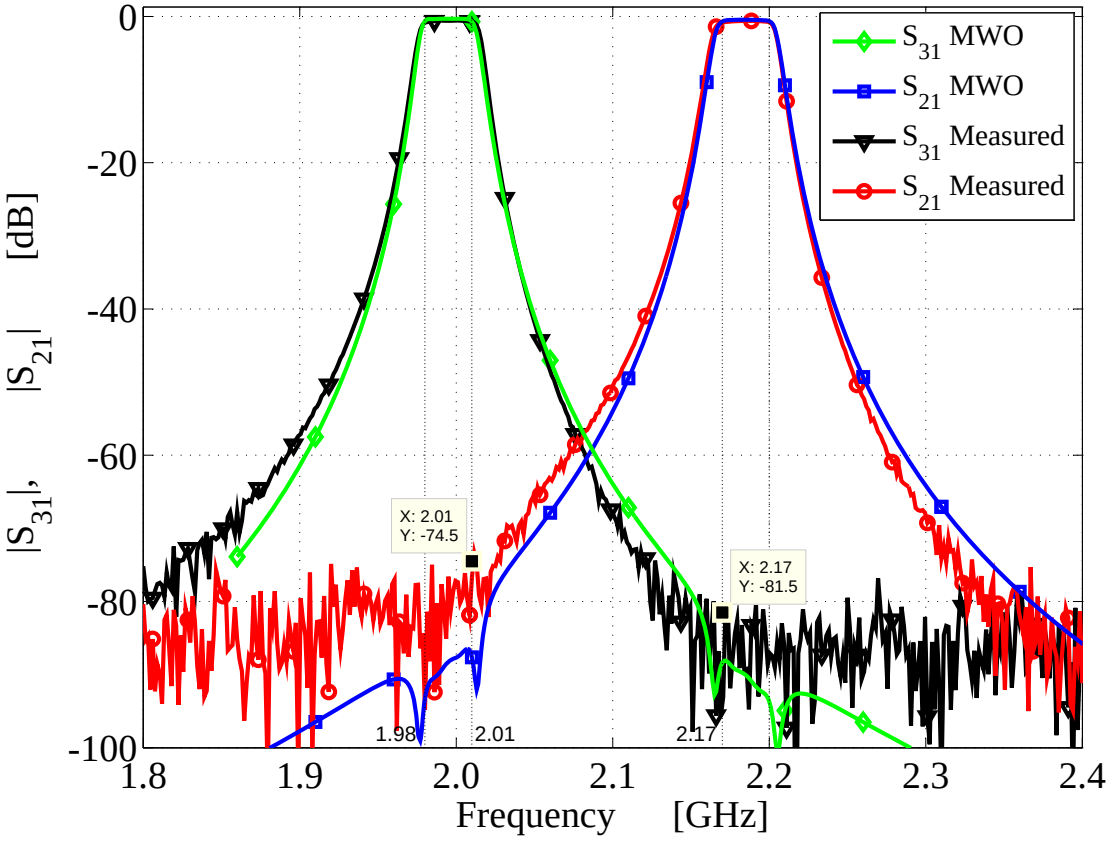


Figure 3.31: Comparison of $S_{21}$ between MWO circuit model and final measurement of the diplexer. The respective frequency bands are indicated with dotted lines.

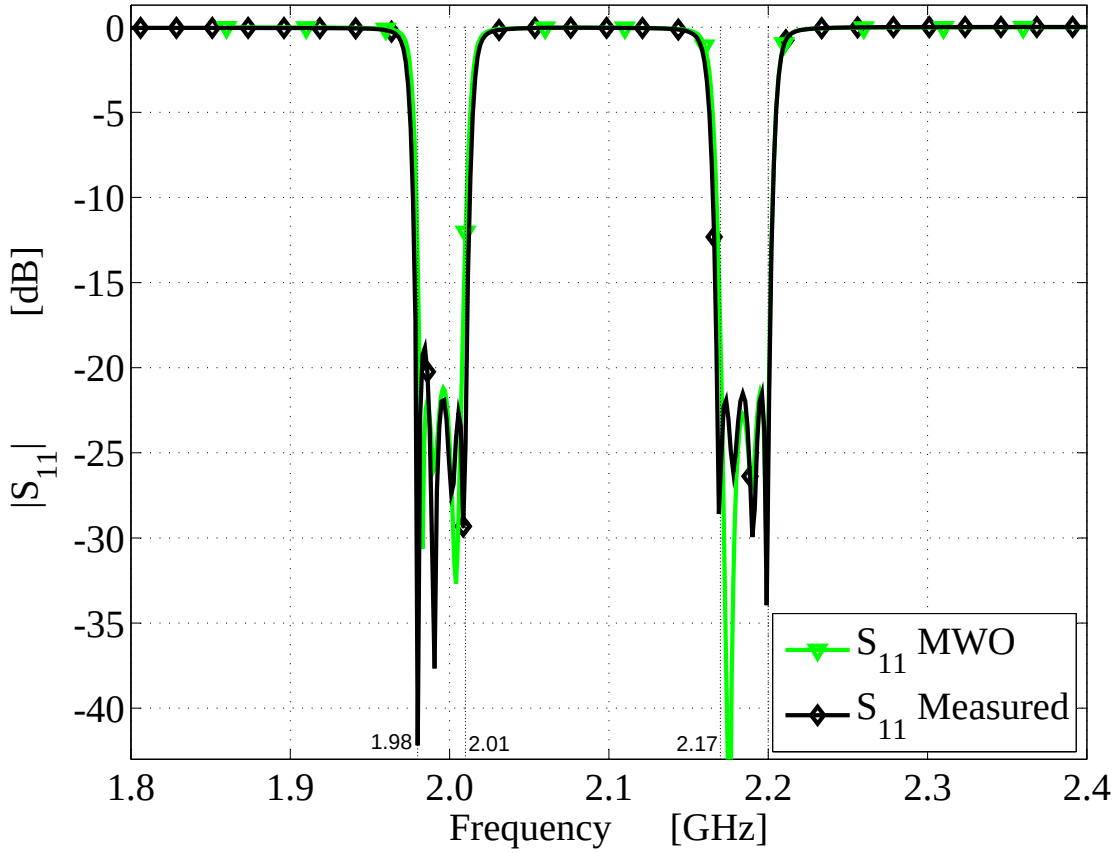


Figure 3.32: Comparison of $S_{21}$ between MWO circuit model and final measurement of the diplexer. The respective frequency bands are indicated with dotted lines.

### 3.14.3 Graphical User Interface

A graphical user interface (GUI) application has been created to aid in the final tuning of the diplexer. The reader is referred to Appendix A for an illustrated and comprehensive investigation into the implementation of the GUI and the tuning process.

The MATLAB model of diplexer is implemented as follows for the two centre sections of the diplexer as illustrated in Table 3-VII. This is illustrated graphically in Fig. 3.33

- The ABCD parameters are determined for each individual resonator
- The ABCD parameters are placed in cascade for each frequency band filter

- The total ABCD parameters are obtained by multiplying the cascaded ABCD matrices
- Calculate $Y_{in}$ from the total ABCD matrix of the respective frequency band filter
- Add the two input admittance to obtain $Y_{total}$
- Calculate $Z_{in}$ from $Y_{total}$
- Calculate $S_{11}$ from $Z_{in}$

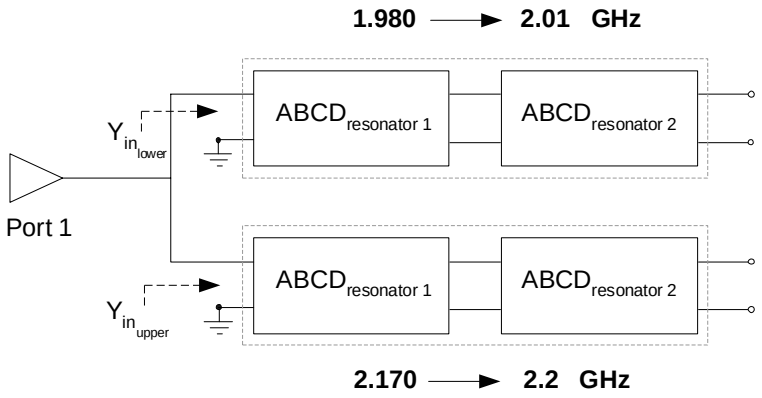


Figure 3.33: Determining $Y_{total}$ for the centre sections of diplexer as defined in Table 3-VII

Two screen shots from the GUI are shown in Fig. 3.34 and Fig. 3.35. In Fig. 3.34, the s-parameters form the network analyser has already been imported into the GUI. In the window, the s-parameters, obtained through measurement and from the ideal MATLAB model are shown. The *NA* denotes *not available*. The 'Optimise' button must be pressed to obtain the extracted parameter values. The 'Bounds' button must be pressed to alter the upper and lower band of each variable for optimisation. Note the difference in the resulting group delay of the measured and ideal response.

Fig. 3.35 shows a screen shot after the 'Optimise' button has been pressed. The values of the extracted parameters are displayed. Note the agreement between the measured and ideal response.

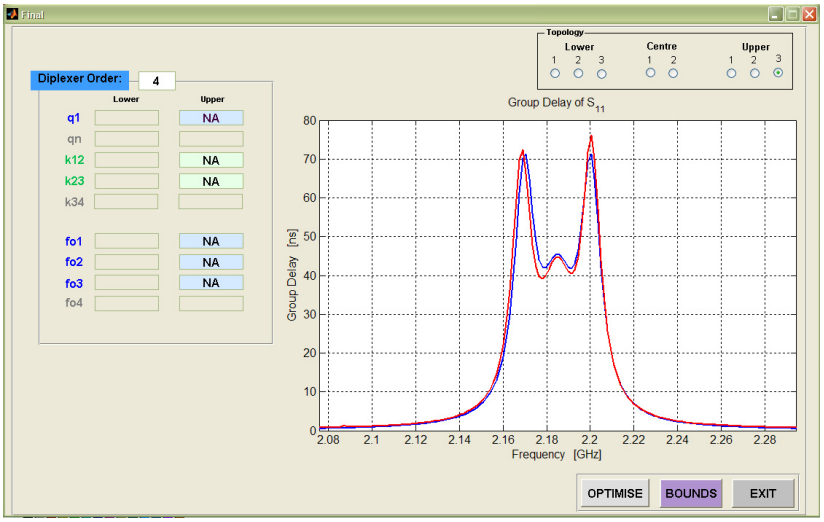


Figure 3.34: Screen shot of GUI application that has been created as a tool to assist diplexer tuning

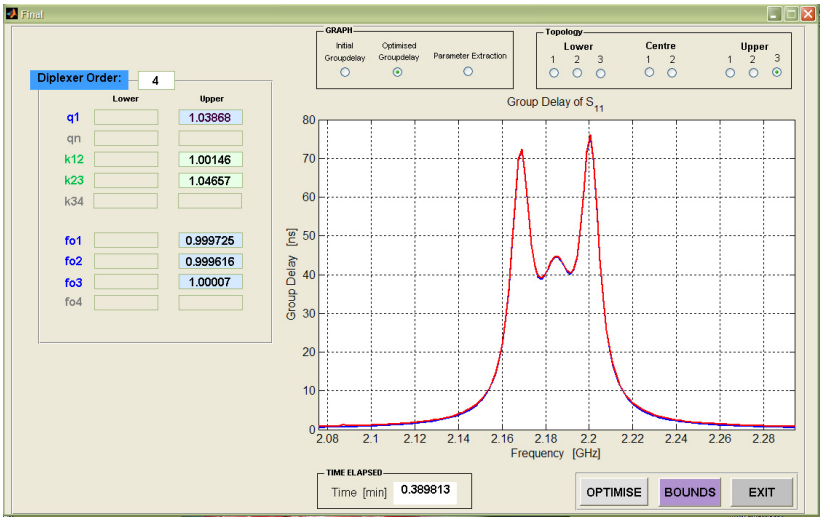


Figure 3.35: Screen shot from GUI application after the 'Optimise' button has been pressed

In Fig 3.36a and Fig 3.36b, the final s-parameters obtained by using the GUI, are shown. For comparison, the initial tuning of the filter is presented. From the results it is seen that the return loss for the GUI application tuned diplexer response is slightly worse than the initial tuning response. This is due to the initial tuning process, if the coupling between the resonators are larger than anticipated, the other variables can be slightly adjusted to cancel the effect of the incorrect coupling.

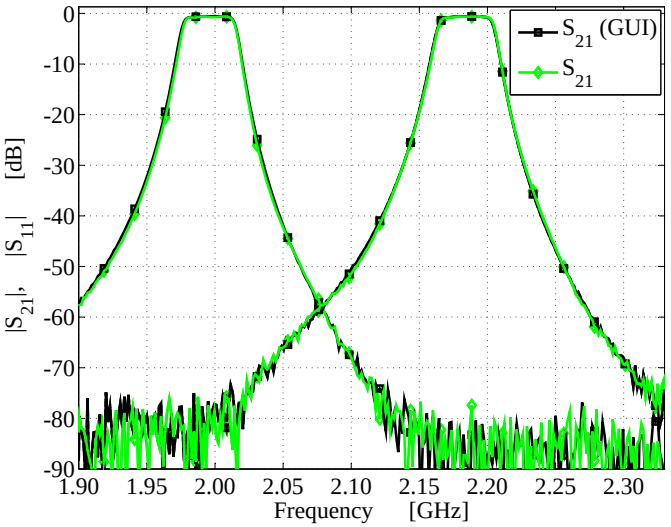


(a) $S_{11}$

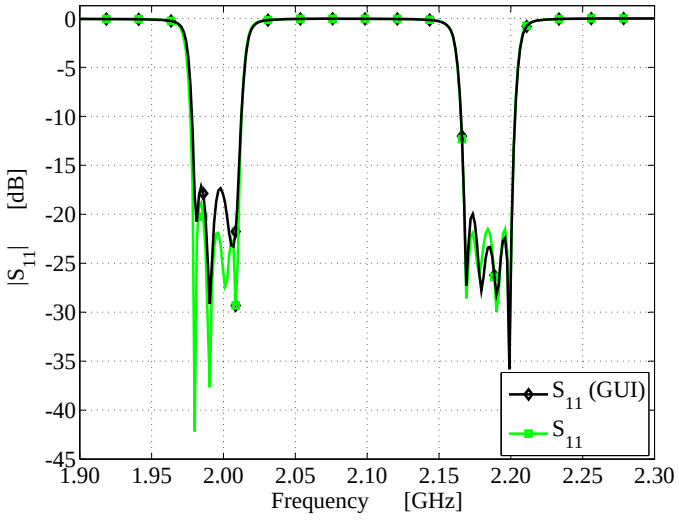


(b) $S_{11}$

Figure 3.36: The final $S_{21}$ and $S_{11}$ obtained from the tuning process by means of the GUI application, compared to the initial hand tuning.

From Fig 3.36, it is clear that the return loss of the lower frequency band of the diplexer was greater than the specified 20 dB. In Table 3-IX, the final extracted parameters for the lower frequency band side of the diplexer are shown. From the results it is seen that $q_1$ showed the largest deviation from the ideal value of one. Hence, increasing the dimension $Dn$ could decrease the return loss.

Table 3-IX: Comparison of final optimised extracted parameters k-, q and frequency against ideal values, obtained by means of the GUI application to aid in the tuning process.

| | **Curvefit** | **Ideal** |
|---|---|---|
| $\mathbf{q}_{1_{lower}}$ | 1.07863 | 1 |
| $\mathbf{k}_{12_{lower}}$ | 1.02584 | 1 |
| $\mathbf{k}_{23_{lower}}$ | 1.04348 | 1 |
| $\mathbf{f}_{01_{lower}}$ | 1.0002 | 1 |
| $\mathbf{f}_{02_{lower}}$ | 0.999259 | 1 |
| $\mathbf{f}_{03_{lower}}$ | 1.00084 | 1 |

## 3.15 Conclusion

Following the discussion of a circuit model for a diplexer in Chapter 2 an overview was given for the physical implementation of the diplexer model in CST. The implementation of the loaded quality factor and coupling coefficient between resonators were investigated. Effect of various dimensions of the diplexer on loaded quality factor, coupling and resonant frequency were shown. The final diplexer was obtained by placing the key structures in cascade. A filter tuning procedure outlined by Ness [8] was implemented in the tuning procedure of the CST diplexer model. The final s-parameters of the diplexer were measured and have shown good correlation between the physical model and the circuit model.

# Chapter 4

# Coupling Mechanisms in Coaxial and Waveguide Filters

## 4.1 Introduction

In Chapter 3 the design process whereby the physical dimensions of the diplexer was obtained (implemented in Computer Simulation Technology, CST), was presented. The coupling between the resonators were implemented by means of irises between resonators. In the circuit model (implemented in Microwave Office, MWO), admittance inverters were used to represent the coupling in the physical model. The circuit model was used as the ideal filter reference response to which the physical model was compared against. By means of parameter extraction in the circuit model, dimensions of the physical model could be adjusted so that its group delay would match that of the circuit model. If the admittance inverter in this procedure is not an accurate circuit representation of the iris, the designer will not be able to adjust the physical model accurately. Designing a filter with tuning capabilities for the measurement stage will usually suffice for inaccuracies in the coupling values. If design specifications are of paramount importance, an incorrect coupling that is too large, can result in the repetition of the design and manufacturing stage.

In this chapter, the coupling mechanisms implemented in coaxial and waveguide filters will be investigated. For the first investigation, two coaxial resonators will be implemented in CST Design Studio. The coupling between the resonators will

be controlled through the use of irises. The resonators will be fed by a capacitive probe. Various coupling coefficients will be realised by altering the width and height of the iris. By means of the Eigenmode Method (implemented in CST), the coupling coefficient will be computed for these dimensions.

The response of the physical model will be compared to the circuit model implementation of a inverter configuration. The coupling coefficient will be determined by means of comparison. For the waveguide media, three impedance inverter configurations will be investigated as to their accurate representation of the coupling coefficient in a post and iris in CST. Numerical results from each of these inverter topologies will be compared to the Eigenmode Method of determining the coupling coefficient. The validation and accuracy of the inverter model and the Eigenmode Method for calculating the coupling coefficient, will therefore be determined.

The different inverter topologies will be used to realise a given coupling coefficient in a waveguide filter realised in CST. A waveguide filter will be implemented by using dimensions as dictated by the inverter model for the coupling coefficient. It will be shown that by choosing a certain inverter model for the circuit model, it can have a dramatic effect on the return- and insertion loss of a filter or diplexer.

## 4.2 Coaxial Implementation

The verification of the Eigenmode Method for determining coupling coefficient for resonators, implemented in coaxial media, will be discussed next. Two resonators were implemented in CST, together with their tuning screws. Coupling between the two resonators are controlled via an iris with width, $W$, and height, $I$. The probes are located near the short-circuited end of the structure. Implementation of resonators in CST together with their parameter definition, is illustrated in Fig. 4.1.

Following the discussion in Chapters 2 and 3 for the circuit representation of two coupled resonators, the circuit model representation of Fig. 4.1 is shown in Fig. 4.2.

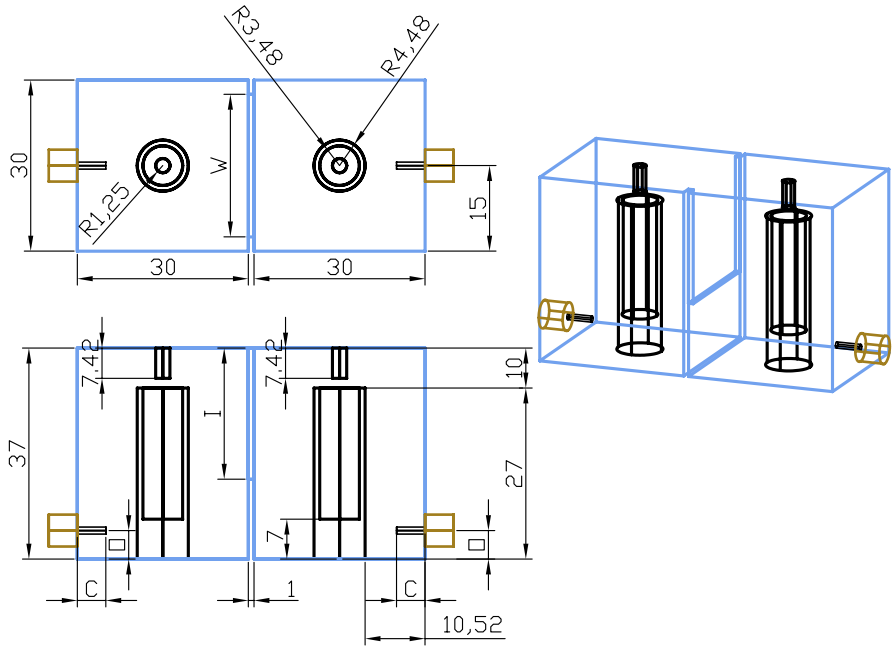


Figure 4.1: Parameter definition for a coaxial resonator. The model is implemented in CST and the coupling coefficient is determined by means of the Eigenmode Method.

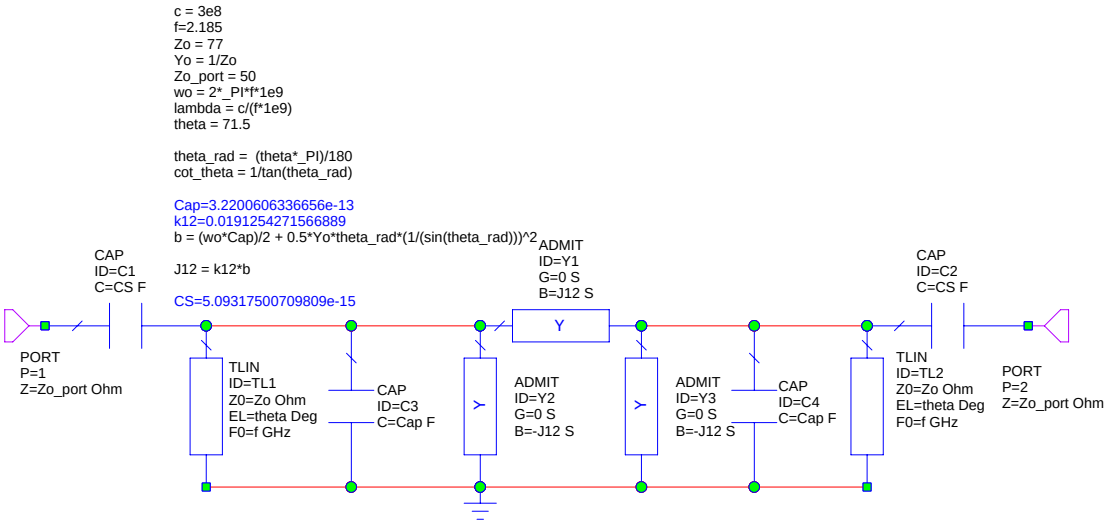


Figure 4.2: MWO schematic of two coupled resonators. Input signal is coupled via an *SMA* capacitive probe. This is represented by the series capacitor to the right of port 1 and to the left of port 2.

### 4.2.1 Design Procedure and Parameter Extraction

In the CST model (Fig. 4.1), a wide range of coupling values were realised by altering the height of the iris, parameter *I*. The resulting s-parameters were imported into the MWO circuit model from CST. The coupling value ($k_{12}$), the shunt capacitor (*Cap*), and the series capacitor (*CS*) were optimised by using a predefined error function. The error function is defined as the difference between the magnitude of $S_{21}$ of the CST and MWO model. The capacitor representive of the resonator and the coupling coefficient is now used in the definition of the Reactance Slope Parameter, Eq. 2.14. An inverter can be realised by Eq. 2.20. The coupling coefficient, $k_{12}$, of this parameter extraction is compared to the coupling coefficient computed by means of the Eigenmode Method.

### 4.2.2 Results

The dimensions used for configuration 1-6 and configuration A-F(CST model) are shown in Table 4-I and Table 4-II, respectively.

Table 4-I: Values of parameter *I* and *W* for *Configuration* 1-6. Parameter *C* and Parameter *O* are set to 5 [mm].

| | **Parameter I** | **Parameter W** |
|---|---|---|
| **Configuration 1** | 25.86 | 13 |
| **Configuration 2** | 25.86 | 16 |
| **Configuration 3** | 25.86 | 20 |
| **Configuration 4** | 25.86 | 23 |
| **Configuration 5** | 25.86 | 25 |
| **Configuration 6** | 25.86 | 27 |

Table 4-II: Values of parameter $I$ and $W$ for *Configuration* A-F. Parameter $C$ and Parameter $O$ are set to 5 [mm].

| | **Parameter I** | **Parameter W** |
|---|---|---|
| **Configuration A** | 35 | 23 |
| **Configuration B** | 29 | 23 |
| **Configuration C** | 23 | 23 |
| **Configuration D** | 17 | 23 |
| **Configuration E** | 11 | 23 |
| **Configuration F** | 5 | 23 |

In *Configurations* 1 to 6, the width of the iris was swept from 13 to 27 mm. *Configurations* A to F, the height of the iris was swept from 35 to 5 mm.

In Fig. 4.3, the optimised $|S_{21}|$ of MWO and the CST model for *Configuration* A and *Configuration* F are shown. These particular configurations are chosen to show the effect of a wide range of coupling coefficients on the bandwidth. The resulting coupling values as determined by the Eigenmode Method and the extracted coupling coefficients for the parameter sweeps, are shown in Tables 4-III and 4-IV.

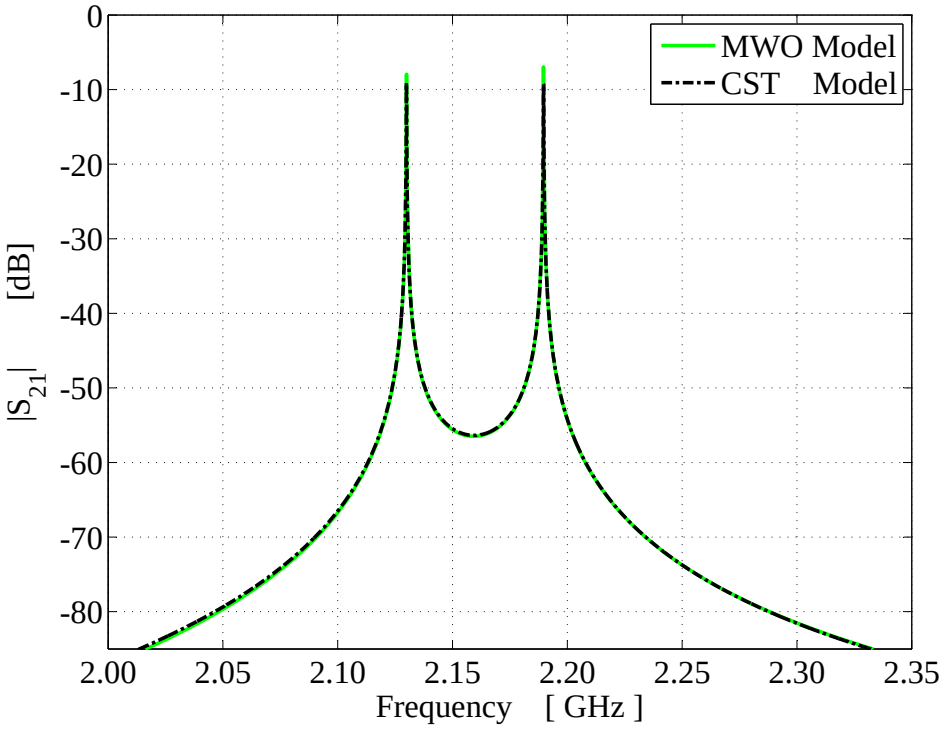


(a) $|S_{21}|$ of both optimised MWO model and the CST model. Configuration A.

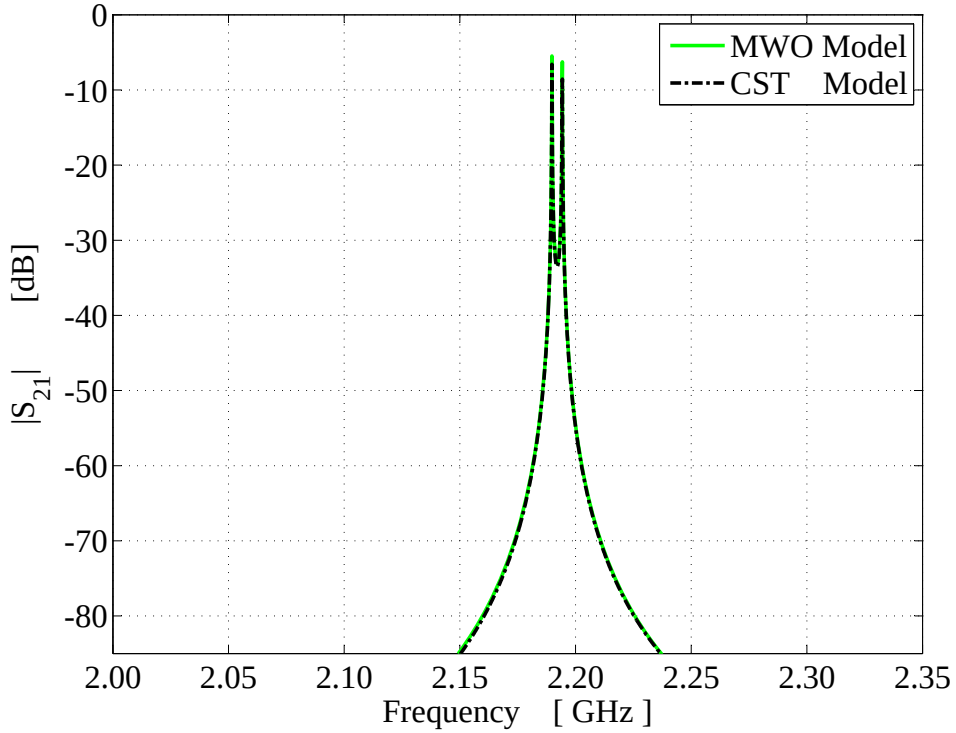


(b) $|S_{21}|$ of both optimised MWO model and the CST model. Configuration F.

Figure 4.3: Coupling coefficient is proportional to the bandwidth.

Table 4-III: Validation of coupling coefficients, $k$, by means of the Eigenmode Method and extracted coupling coefficient of the circuit model. The effect of adjusting the height of iris, parameter $I$, on the coupling coefficient was investigated.

| | **Coupling Coefficient, $k$** | | |
|---|---|---|---|
| | **Eigenmode Method** | **Parameter Extraction** | **% Deviation** |
| **Configuration A** | 0.0276392 | 0.02762362 | 0.0564 |
| **Configuration B** | 0.0190652 | 0.01912543 | 0.3159 |
| **Configuration C** | 0.0108036 | 0.01084173 | 0.3529 |
| **Configuration D** | 0.00625919 | 0.00624722 | 0.1913 |
| **Configuration E** | 0.00403525 | 0.00404073 | 0.1358 |
| **Configuration F** | 0.00202838 | 0.00202412 | 0.2100 |

Table 4-IV: Validation of coupling coefficients, $k$, by means of the Eigenmode Method and extracted coupling coefficient of the circuit model. The effect of adjusting the width of iris, parameter $W$, on the coupling coefficient was investigated.

| | **Coupling Coefficient, $k$** | | |
|---|---|---|---|
| | **Eigenmode Method** | **Parameter Extraction** | **% Deviation** |
| **Configuration 1** | 0.014357 | 0.01440490 | 0.3336 |
| **Configuration 2** | 0.00359973 | 0.00362188 | 0.6154 |
| **Configuration 3** | 0.00638543 | 0.00637888 | 0.1026 |
| **Configuration 4** | 0.0108932 | 0.01089449 | 0.0118 |
| **Configuration 5** | 0.0164488 | 0.01653486 | 0.5232 |
| **Configuration 6** | 0.0181029 | 0.01815924 | 0.3112 |

Numerical results given above, show that the calculation of the coupling coefficient by means of the Eigenmode Method and the circuit model, are in agreement. When very small coefficients are used to calculate the deviation, the resulting deviation will be larger than for larger coupling coefficients. This is due to numerical inaccuracy. The deviation of the extracted coupling coefficient from the Eigenmode Method, is given by Eq. 4.1

$$deviation = \frac{Eigenmode_k - MWO_k}{Eigenmode_k} \cdot 100 \tag{4.1}$$

where $Eigenmode_k$ is the coupling coefficient obtained by the Eigenmode Method in the CST model and $MWO_k$ is the optimised extracted coupling coefficient from the circuit model. The coupling coefficient as calculated by the Eigenmode Method is taken as the reference value.

## 4.3 Waveguide Implementation

### 4.3.1 Concise Design Procedure For Comparison of Coupling Mechanism

A waveguide filter can be implemented using lengths of waveguide with shunt discontinuities [18]. These shunt discontinuities behave as impedance inverters [18] and a circuit model consisting of inverters and resonators can represent the physical waveguide model. The question may now be asked as to which particular impedance inverter will yield the most accurate representation of the coupling in the physical model, computed by the Eigenmode Method. To answer this question, two structures for physical coupling in a waveguide filter, will be investigated. These are:

- Inductive Iris
- Inductive Post

For the implementation of the physical model, the rectangular waveguide will be used as resonator. Coupling between two resonators were realised as mentioned above by means of an iris (model 1) and a post (model 2), respectively. The coupling coefficient between the resonators are controlled by altering the width of the iris, or altering the radius of the post. A parameter sweep was then generated for both models to realise a wide range of coupling coefficients. The resulting $S_{21}$ for these coupling coefficients were exported to MWO. The Eigenmode Method (Eq. 3.9) was used to determine the coupling coefficient for these dimensions of the iris and post. The resonating frequency at which the coupling was determined, was calculated by Eq. 3.10.

In MWO, a circuit model was implemented to represent the physical coupling structure in CST. This model consist of a inverter topology placed in between lengths of waveguide. The coupling coefficient was then optimised such that the magnitude of $S_{21}$ of both circuit and physical model are equal at the resonating frequency for a certain inverter topology.

An in-depth discussion will be given regarding the realisation of the respective inverter topology in section 4.4. The coupling coefficients obtained by the various inverter models for a certain physical dimension, are then compared to the Eigenmode Method's coupling coefficient for the same dimension. This shows that for a given dimension for a post or iris in the physical model, slightly different coupling coefficients are obtained for the various inverter topologies.

## 4.4 Inverter Topologies Under Consideration

The following inverter topologies will be investigated in the coupling mechanisms in waveguide media, see Table 4-V. The inverter models will be designated as Configuration 1, 2 and 3 respectively. Configuration 1 consists of a T-network of ideal impedances. Configuration 2 consists of a shunt inductance placed at the centre of two capacitors. Configuration 3 consists of a shunt inductance, $\jmath X$, placed between two short transmission lines, each with an electrical length of $\frac{\Theta}{2}$ [28]. A complete derivation of equations for inverter of Configuration 3, is given in Appendix B. Configuration 2 is given by [7] as the equivalent circuit for the shunt discontinuities as illustrated in Fig. 4.4a and Fig. 4.4b.

(a) Front sectional view of an iris (b) Front sectional view of a post

Figure 4.4: Shunt discontinuities, adapted from [7].

### 4.4.1 Frequency at which Coupling is Calculated

In the three configurations of impedance inverters that will be discussed next, the coupling coefficient will be calculated at a certain frequency. This fixed frequency, corresponding to a certain iris or post dimension in the CST model was determined by the Eigenmode Method in the CST model, Eq. 3.10. The coupling coefficient will then be determined by means of tuning, until the magnitude of $S_{21}$ of the MWO and CST models are equal at this frequency. This is to ensure that the coupling coefficients are computed at the same frequency as the Eigenmode method. Hence the coupling values for the four can be used for comparison.

Table 4-V: Inverter topologies under consideration for comparison of coupling coefficients. The three topologies are given the names of configuration 1, 2 and 3. These will be the designated names that will be used in the graphical illustration of the coupling values and $S_{21}$ that will follow in the underlying sections.

| **Inverter Topology** | **Configuration** |
|---|---|
| 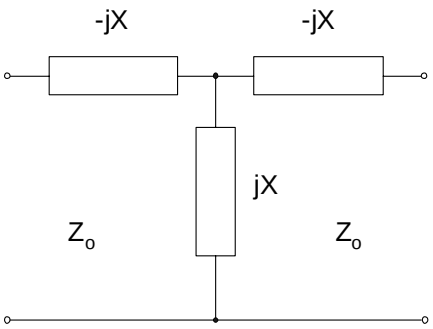  | Configuration 1 |
| 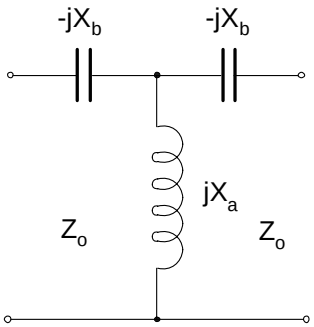  | Configuration 2 |
| 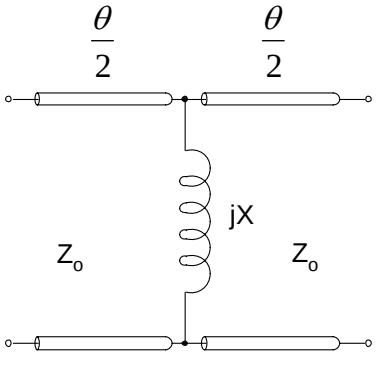  | Configuration 3 |

### 4.4.2 Configuration 1

*Configuration* 1 consists of a T impedance network and is graphically illustrated in Table 4-V. This configuration is frequency independent [18] if implemented by an ideal impedance structure in MWO.

The reactance of the inverter in *Configuration* 1 will be calculated by determining the reactance slope parameter of the series circuit, as discussed in section 2.7. The input impedance, $Z_{in}$ of a short-circuited transmission line is given by Eq. 4.2 where $Z_o$ is the characteristic impedance in $\Omega$ [17].

$$Z_{in} = \jmath Z_o \tan\theta = \jmath X \qquad [\Omega] \tag{4.2}$$

The electrical length $\Theta$ of the transmission line is equal to the propagation constant $\beta$, multiplied by the length $\ell$ of the transmission line, Eq. 4.3 [16].

$$\theta = \beta\ell \tag{4.3}$$

The propagation constant for a waveguide is defined as in Eq. 4.4 [16], where

$$\beta = \frac{\omega}{c}\sqrt{1-\left(\frac{\omega_c}{\omega}\right)^2} \tag{4.4}$$

$$\begin{aligned} \omega_c &= \text{cut-off angular frequency} && [rad\cdot s^{-1}] \\ \omega &= \text{angular frequency} && [rad\cdot s^{-1}] \end{aligned}$$

In the calculation of the reactance slope parameter, the input reactance of the circuit cn be differentiated with respect to the angular frequency $\omega$, see Eq. 4.5.

$$\frac{dX}{d\omega} = \frac{dX}{d\Theta} \cdot \frac{d\Theta}{d\beta} \cdot \frac{d\beta}{d\omega} \tag{4.5}$$

The input reactance $X$ differentiated with respect to the electrical length $\Theta$ is given by Eq. 4.6.

$$\frac{dX}{d\Theta} = Z_o \left[1 + \tan^2 \Theta\right] \tag{4.6}$$

The electrical length $\Theta$ differentiated with respect to the propagation constant, $\beta$ Eq. 4.7.

$$\frac{d\Theta}{d\beta} = \ell \tag{4.7}$$

The propagation constant $\beta$ differentiated with respect to the angular frequency $\omega$ is given by Eq. 4.8.

$$\begin{aligned} \frac{d\beta}{d\omega} &= \frac{d}{d\omega}\left[\frac{\omega}{c}\left(1 - \left(\omega_c^2 \cdot \omega^{-2}\right)\right)^{\frac{1}{2}}\right] \\ &= \frac{1}{c}\left[1 - \left(\omega_c^2 \cdot \omega^{-2}\right)\right]^{\frac{1}{2}} + \frac{\omega}{2C}\left[1 - \left(\omega_c^2 \cdot \omega^{-2}\right)\right]^{\frac{-1}{2}}\left[\frac{2\omega_c^2}{\omega^3}\right] \end{aligned} \tag{4.8}$$

The reactance slope $\chi$ parameter, Eq. 4.9.

$$\chi = \frac{dX}{d\omega} \cdot \frac{\omega_o}{2} \tag{4.9}$$

The reactance, $X_o$ of the inverter model of *Configuration* 3 is now given by Eq. 4.10.

$$X_o = \chi \cdot k \tag{4.10}$$

Equations 4.2 to 4.10 are then implemented as a circuit model in MWO as given in Fig. 4.5.

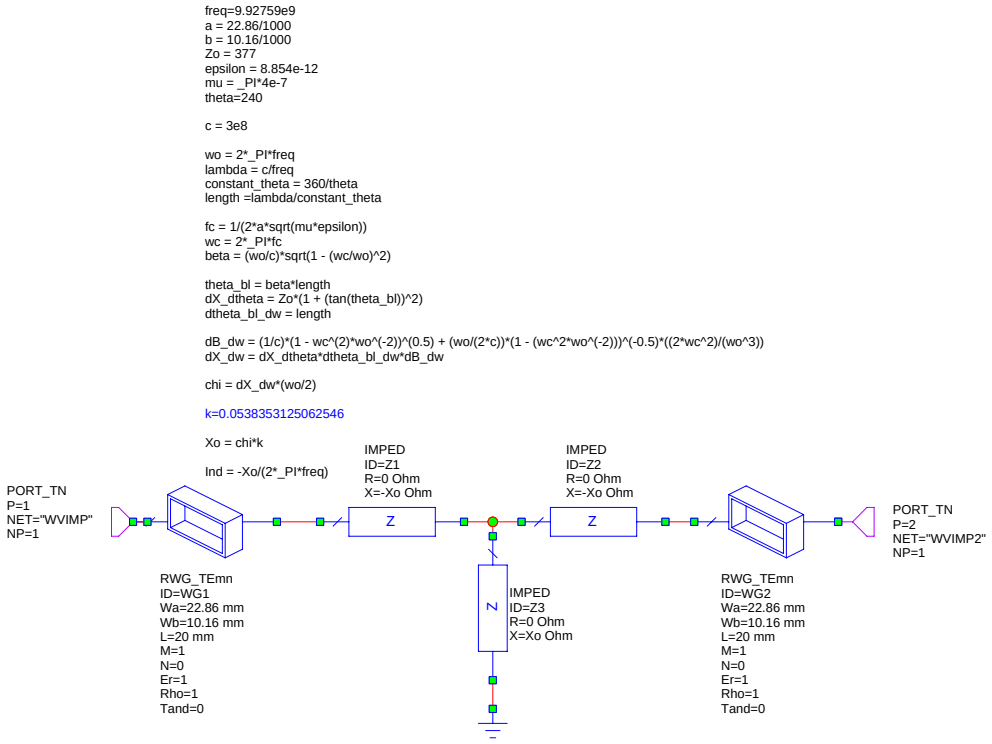


Figure 4.5: MWO schematic of *Configuration* 1

### 4.4.3 Configuration 2

In Matthaei et al [7] and [6] it is stated that a shunt lumped-inductance discontinuity may be used to represent a very thin (dimensions should be small in terms of the wavelength [7]) inductive iris. Thin inductive obstacles will result in frequency proportional positive reactances [7] and as a result can be modelled as a shunt inductor. Configuration 2 is illustrated in Table 4-V. The coupling coefficient of this type of configuration inverter will now be frequency dependent [18] due to the frequency dependence of the inductance.

The implementation of *Configuration 2* in MWO is shown in Fig. 4.6.

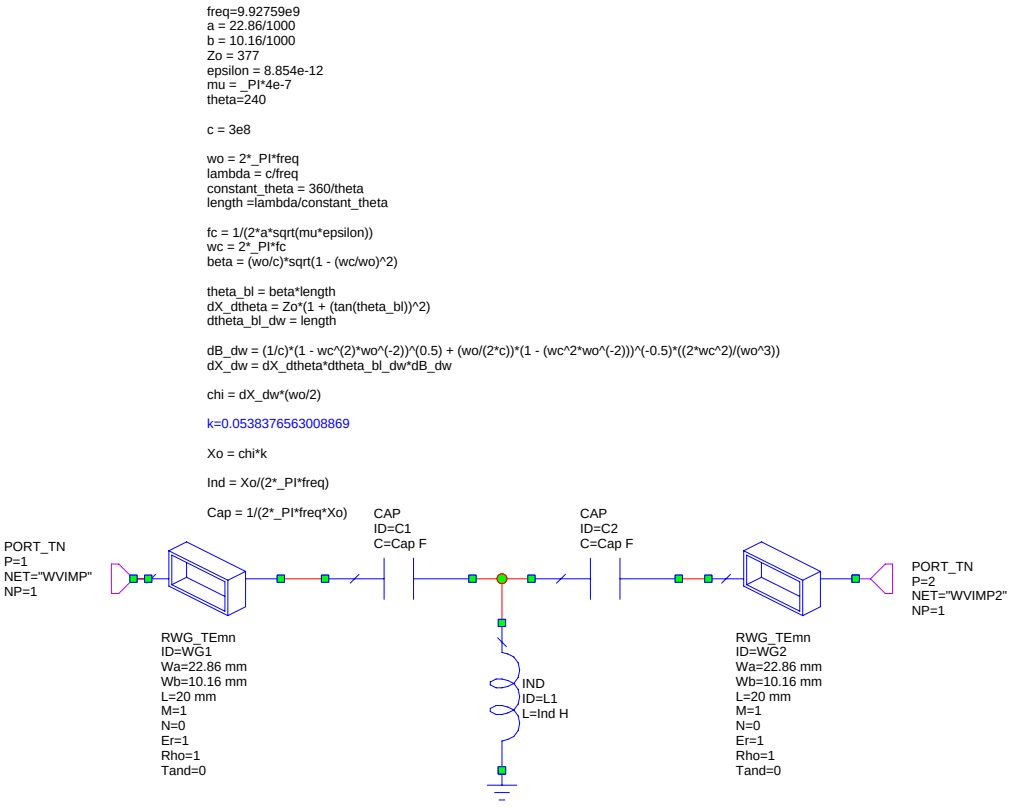


Figure 4.6: MWO schematic of *Configuration 2*

The derivation of the reactance slope parameter for Configuration 1, follows the same procedure as in 4.2 to 4.10. It will therefore not be repeated. The value of the

inductance and capacitance are then determined as in Eq. 4.11, where *Ind* denotes the inductance, *Cap* is the capacitance and $f$ is the frequency in Hertz.

$$\begin{aligned} Ind &= \frac{X_o}{2 \cdot \pi \cdot f} \qquad [Henry] \\ Cap &= \frac{1}{2 \cdot \pi f \cdot X_o} \qquad [Farad] \end{aligned} \tag{4.11}$$

### 4.4.4 Configuration 3

*Configuration* 3 consists of a shunt lumped-inductance set between lines of negative electrical length $\frac{\Theta}{2}$. For a post with a large radius, the electrical length $\frac{\Theta}{2}$ may be positive [7]. The length of transmission lines can be added or subtracted from the adjacent lines of the same impedance [7].

The coupling coefficient in this configuration was determined by tuning the inductance at a certain frequency until the magnitude of $S_{21}$ of both the CST and MWO model are equal.

The reactance of the inverter, X, can then be determined by Eq. 4.12, where L is the inductance in Henry.

$$X = \jmath\omega L \tag{4.12}$$

The electrical length, $\theta$, can then be calculated by the following relation, Eq. 4.13 [28]

$$\theta = \tan^{-1} \frac{2X}{Z_o} \tag{4.13}$$

The inductance value is then optimised in MWO until $|S_{21}|$ of both the circuit model and physical model are equal at the predefined frequency (section 4.4.2). Inductance obtained by the optimisation was then used in MATLAB to calculate the coupling coefficient $k$ by use of Eq. 4.14 [28].

$$\text{Coupling coefficient, k} \quad = \quad \tan^{-1}\frac{2X}{Z_o} \tag{4.14}$$

The circuit schematic of *Configuration* 3 in MWO, is shown in Fig. 4.7.

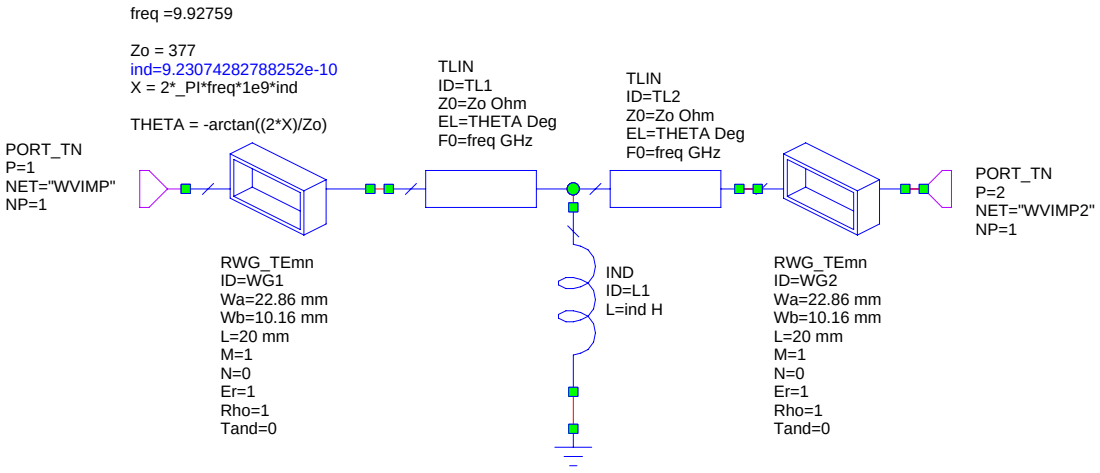


Figure 4.7: MWO schematic of *Configuration* 3

### 4.4.5 Computational Results

#### Post

In the previous section, the three different impedance inverter configurations were evaluated and discussed. Parameter definitions together with the dimensions used to obtain the coupling values, are shown in Fig. 4.8. The extracted coupling coefficients for these three impedance inverter configurations for a post, are shown

in Fig. 4.10. The numerical results show clearly that *Configuration* 1 and 2 follow the coupling coefficient of the Eigenmode Method the closest.

As the coupling values are computed at a single frequency as calculated by the Eigenmode Method, section 4.4.1, both configurations would result in the same coupling coefficient. A possible rationale for *Configuration* 3 showing the largest deviation from the Eigenmode Method, is that the post is not accurately represented by the transmission line lengths in the impedance inverter model.

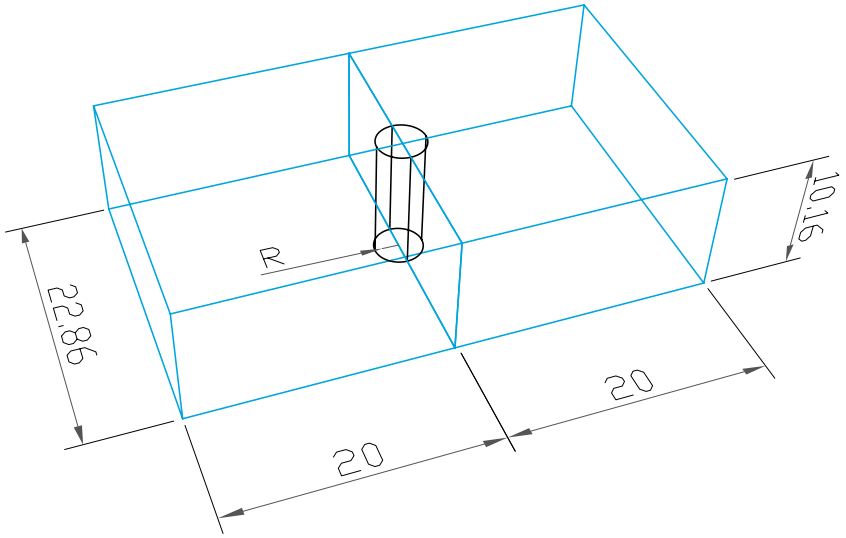


Figure 4.8: The dimensions for a post that will result in a wide range of couple coefficients by sweeping parameter $R$. Coupling coefficients are computed by the Eigenmode Method, implemented in the post processing template in CST.

### Iris

In Fig. 4.11 the numerical results obtained for the three inverter configurations, together with the coupling coefficients obtained by the Eigenmode Method for an iris, are shown. As for the post, *Configuration* 1 and 2 yield the same results, due to reasons given above. *Configuration* 3 now shows the smallest deviation from the Eigenmode Method. This could be due to the transmission line lengths being a more accurate representation of the iris in the physical model. The transmission line is able to represent the resulting phase difference in the electric and magnetic fields that propagate in the waveguide.

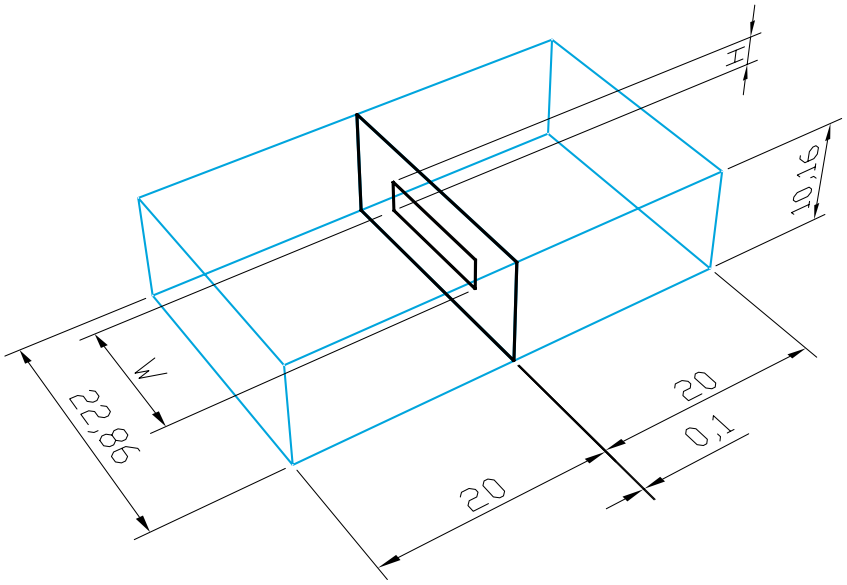


Figure 4.9: The dimensions for an iris that will result in a wide range of couple coefficients by sweeping parameter $W$. Coupling coefficients are computed by the Eigenmode Method, implemented in the post processing template in CST.

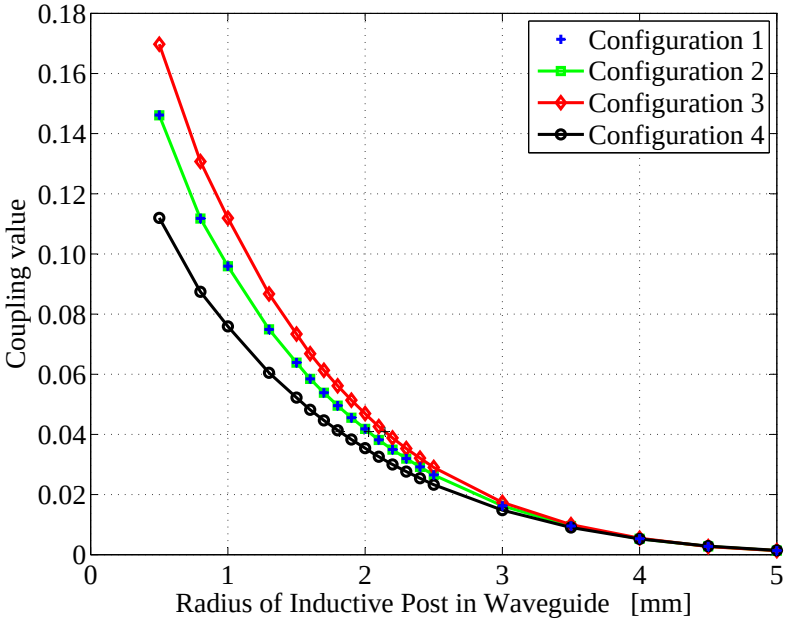


Figure 4.10: Comparison of Coupling Coefficients obtained by the three inverter configurations and the Eigenmode Method for determining coupling coefficients for a post in a rectangular waveguide.

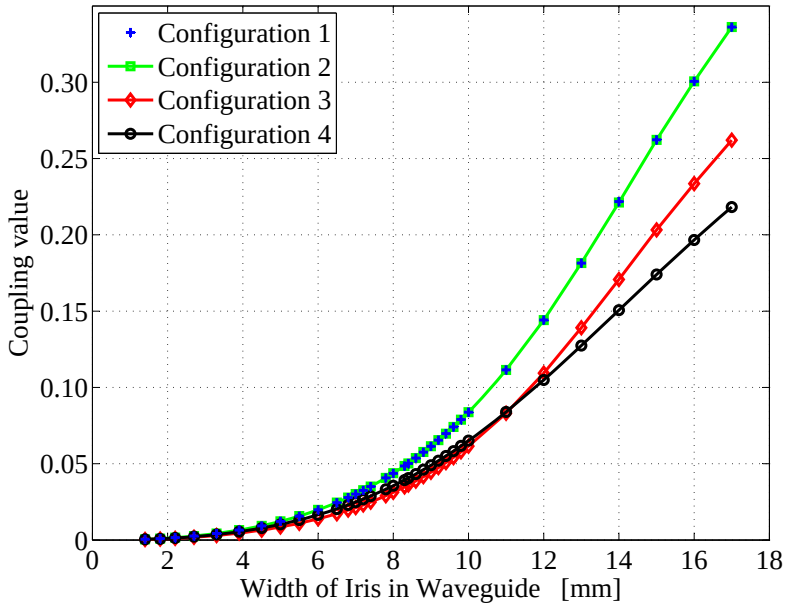


Figure 4.11: Comparison of Coupling Coefficients obtained by the three inverter configurations and the Eigenmode Method for determining coupling coefficients for an iris in a rectangular waveguide.

## 4.5 Implementation of Coupling Mechanisms in a Filter

The different inverter topologies were implemented in a waveguide filter. Once again, the coupling between the resonators will be implemented using iris and inductive posts, respectively. It was decided that a third order Chebyshev filter with 0.01 dB ripple would be used as the filter prototype to investigate the effect of the inverter models. Bandwidth of filter is set to be 6 % of centre frequency. Centre frequency is to be 10 GHz, with the result that dimensions for $X$ band will be used. The dimensions are 22.86 mm by 10.16 mm for the waveguide resonators at $X$ band [17]. The following k and q values were obtained from [10], Table 4-VI.

Table 4-VI: The normalised k and q values for a third order Chebyshev filter with 0.01 dB ripple with $w_c = 1$ and a load resistance, $R_l = 1$ as given in [10]. Bandwidth is decided on as 6 % of centre frequency.

| | $\mathbf{q}_1$ | $\mathbf{q}_n$ | $\mathbf{k}_{12}$ | $\mathbf{k}_{23}$ |
|---|---|---|---|---|
| **Normalised [10]** | 1.811 | 1.1811 | 0.6818 | 0.6818 |
| **Bandwidth Scaled** | 19.685 | 19.685 | 0.0409 | 0.0409 |

For a given k- value of 0.0409, dimensions of the iris and post are found from Fig. 4.12 and Fig. 4.12. Table 4-VII shows the dimensions for the iris and post models for three configurations and the Eigenmode Method for determining the coupling coefficient.

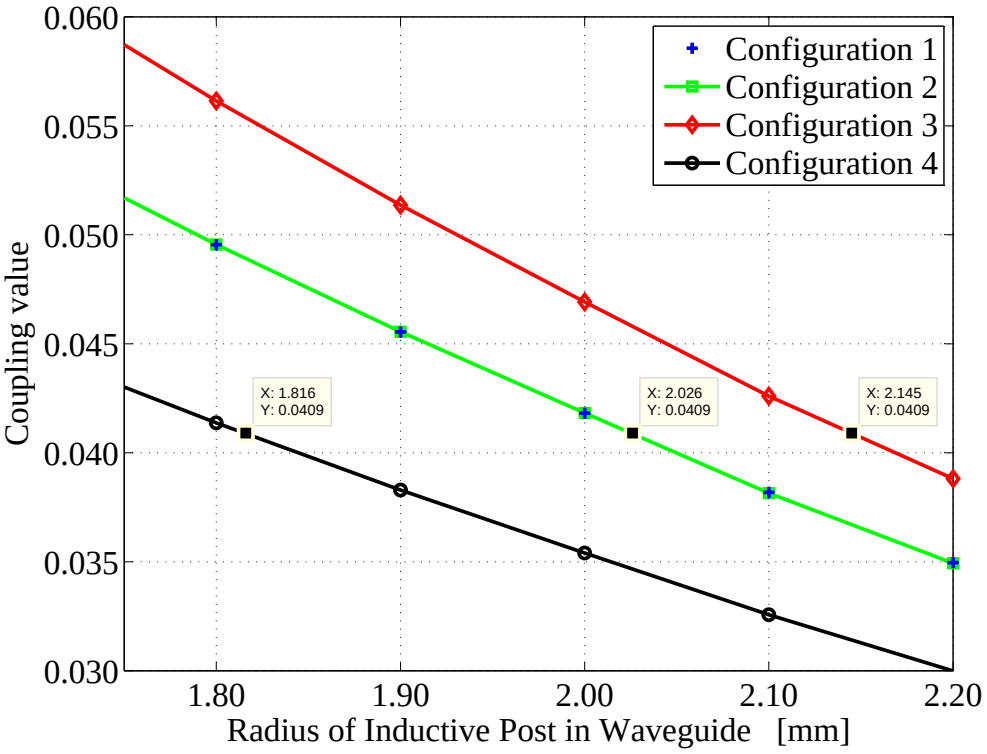


(a) Post

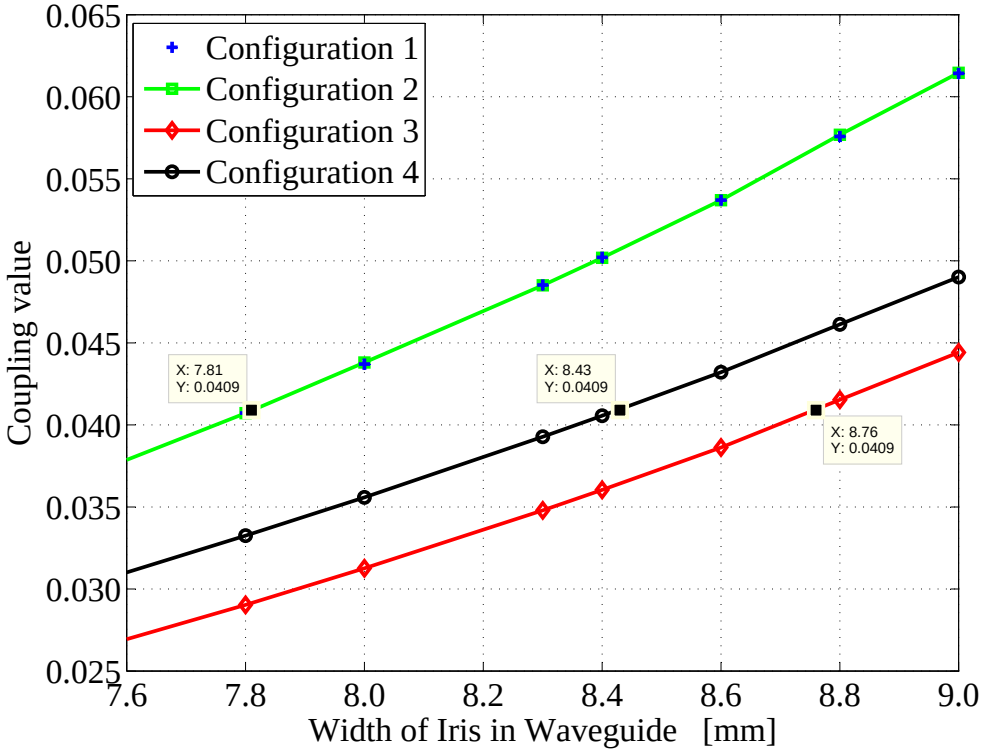


(b) Iris

Figure 4.12: Comparison of coupling coefficients for a post and an iris

Table 4-VII: Dimensions obtained for the iris and post (CST model) by means of the three configurations and the Eigenmode Method for determining the coupling coefficient.

| | **Width of Iris [mm]** | **Radius of Post [mm]** |
|---|---|---|
| **Configuration 1** | 7.81 | 2.026 |
| **Configuration 2** | 7.81 | 2.026 |
| **Configuration 3** | 8.76 | 2.145 |
| **Eigenmode method** | 8.43 | 1.816 |

### 4.5.1 Post

As the dimensions for ensuring a predetermined coupling coefficient is known, only the radius of the first and last post and the lengths of the waveguide resonators, are at this stage unknown. The relation between the group delay and the loaded quality factor (as discussed in section 3.8 [8]) was implemented in CST and the radius of the post optimised. Dimensions used for the CST model are graphically illustrated in Fig. 4.8. A radius of the post, dimension $R$, was found to be 0.54 mm.

The third order filter was then implemented by using the radii of the post obtained in Fig. 4.12. Sections of the filter consisting of the loaded quality factor post and the coupling between the resonators, were then configured by placing the relevant sections in cascade. A graphical illustration of the filter implementation in CST, can be seen in Fig. 4.13. Lengths of waveguide resonators, $L_1$ and $L_2$ were optimised to result in centre frequency of 10 GHz. The initial starting point for these dimensions before optimisation, were chosen as $\frac{\lambda}{2}$ at the centre frequency of 10 GHz.

The following dimensions for the waveguide filter were obtained for the three inverter configurations and the Eigenmode Method, Table 4-VIII.

Table 4-VIII: Dimensions obtained for the post representation of the impedance inverter (CST model). The Eigenmode Method was used for determining the coupling coefficient. Dimensions $R_1$ is approximately 0.53706 mm.

| **Dimensions** | $\mathbf{L}_1$ [mm] | $\mathbf{L}_2$ [mm] | $\mathbf{R}_2$ [mm] |
|---|---|---|---|
| **Configuration 1** | 18.715 | 20.248 | 2.026 |
| **Configuration 2** | 18.715 | 20.248 | 2.026 |
| **Configuration 3** | 18.648 | 20.700 | 2.145 |
| **Eigenmode method** | 18 | 20.023 | 1.816 |

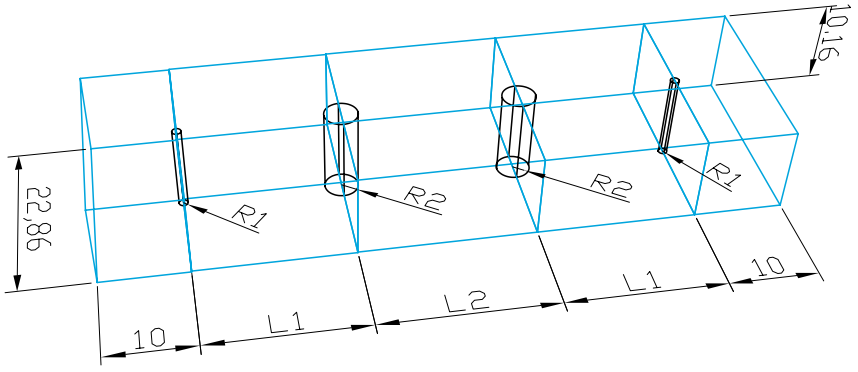


Figure 4.13: Dimensions for CST model with post as coupling structure

### 4.5.2 Computational Results

The dimensions obtained in section 4.5, resulted in obtaining the following $S_{11}$ and $S_{21}$ response, Fig. 4.14 and Fig. 4.15. The results clearly show that the best $S_{11}$ and $S_{21}$ response for rectangular waveguide with an inductive post is obtained by using dimensions determined by the *Configuration* 4 (Eigenmode Method).

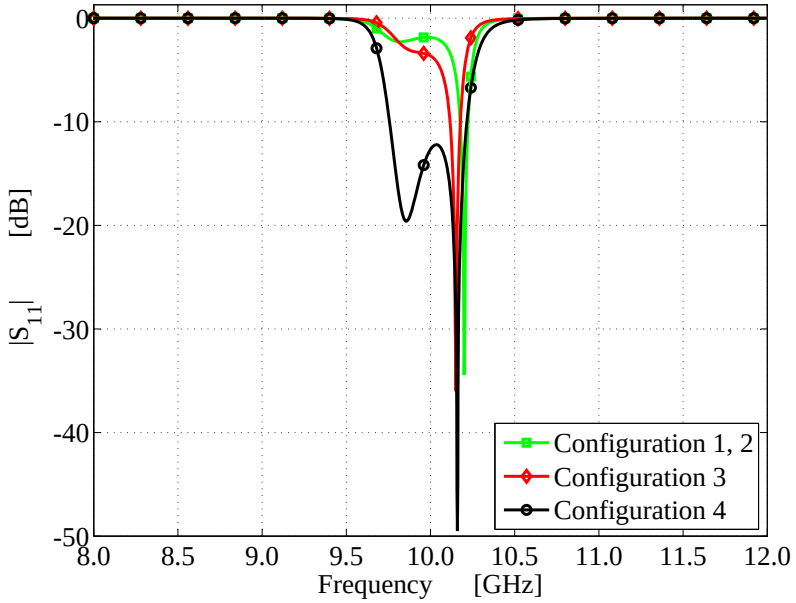


Figure 4.14: $S_{11}$ of rectangular waveguide filter with inductive post. Use was made of dimensions obtained in section 4.5 for a predetermined coupling coefficient of 0.0409.

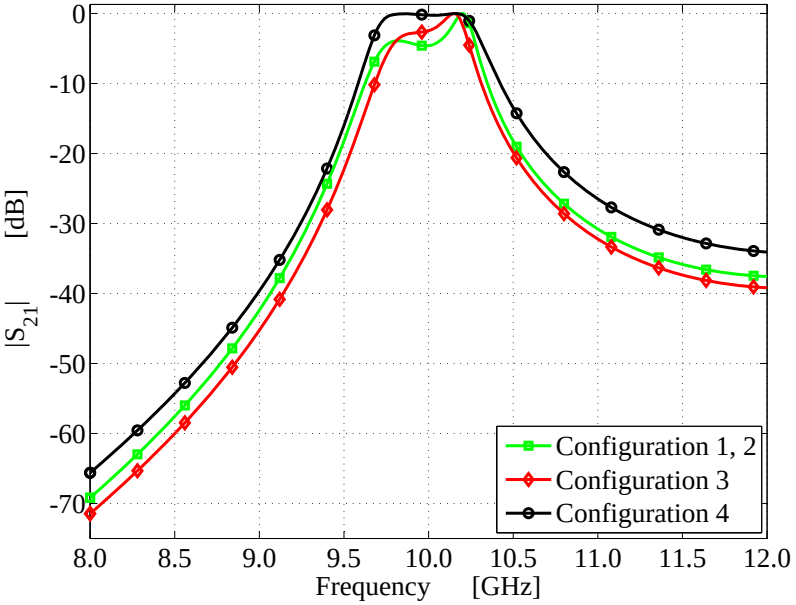


Figure 4.15: $S_{21}$ of rectangular waveguide filter with inductive post. Use was made of dimensions obtained in section 4.5 for a predetermined coupling coefficient of 0.0409.

### 4.5.3 Iris

In the physical model with an iris, the width of the iris was required to enable a q-value as given in Table 4-VI. The same procedure as for the post was followed for determining the dimensions of the iris. The height of the iris was kept constant at 3 mm. Parameter definition of CST model is given in Fig. 4.16.

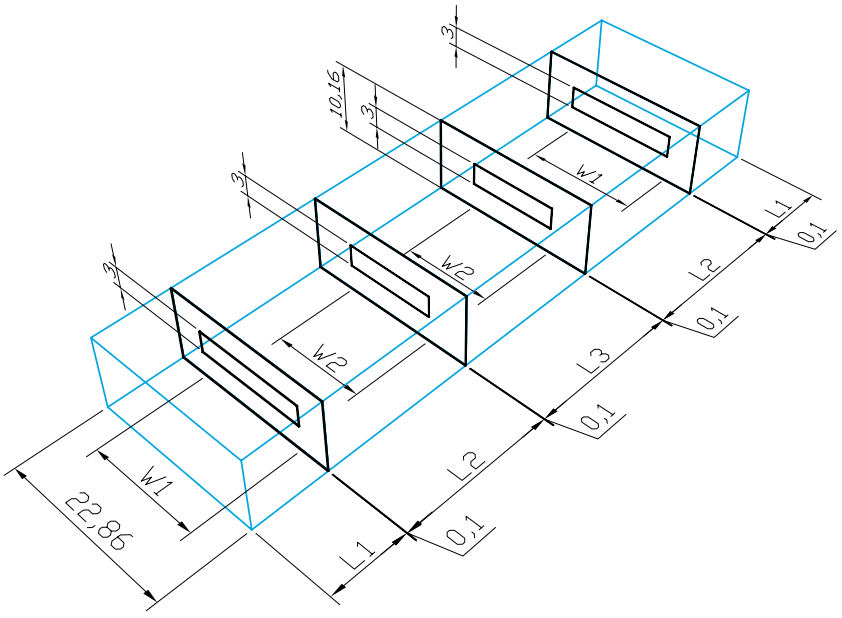


Figure 4.16: Dimensions for CST model with an iris as coupling structure

Final dimensions for the three inverter topologies and the Eigenmode Method, are given in Table 4-IX.

Table 4-IX: Dimensions obtained for the iris representation of the impedance inverter (CST model). The three configurations and the Eigenmode Method for determining the coupling coefficient, are investigated. Length $L1 = 10$ [mm] and $W1 = 11.720$ [mm]

| **Dimensions** | $\mathbf{L}_2$ [mm] | $\mathbf{L}_3$ [mm] | $\mathbf{W}_2$ [mm] |
|---|---|---|---|
| **Configuration 1** | 17.688 | 18.220 | 7.81 |
| **Configuration 2** | 17.688 | 17.688 | 7.81 |
| **Configuration 3** | 16.895 | 18.065 | 8.76 |
| **Eigenmode method** | 17.256 | 18.111 | 8.43 |

### 4.5.4 Computational Results

The results obtained for using the dimensions obtained in section 4.5 for a predetermined coupling, resulted in obtaining the following $S_{11}$ and $S_{21}$ response, Fig 4.17 and Fig. 4.15. The results clearly show that the best $S_{11}$ and $S_{21}$ response for rectangular waveguide with an inductive iris are obtained by using dimensions determined by the *Configuration* 3, followed by *Configuration* 4 (Eigenmode Method). *Configuration* 4 consists of the lumped shunt inductance set between lengths of transmission line.

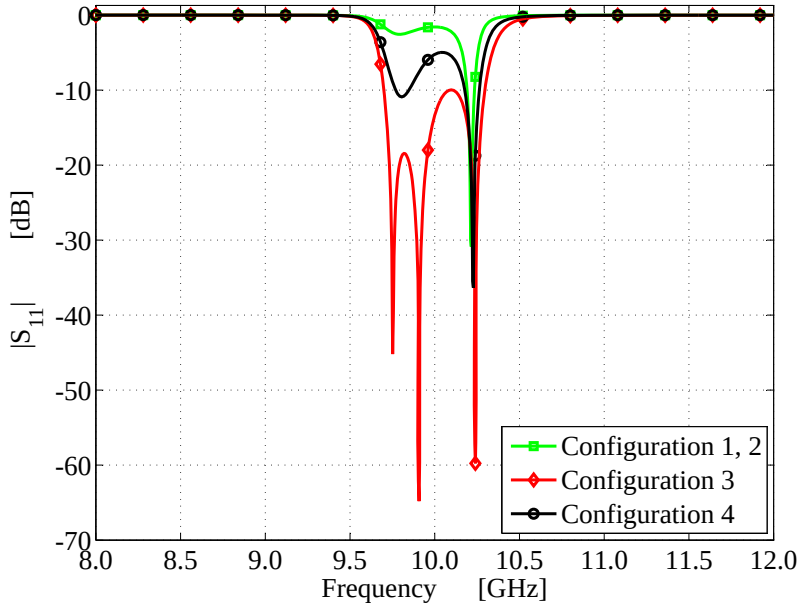


Figure 4.17: $S_{11}$ of rectangular waveguide filter with inductive iris. Dimensions obtained in section 4.5 for a predetermined coupling coefficient of 0.0409.

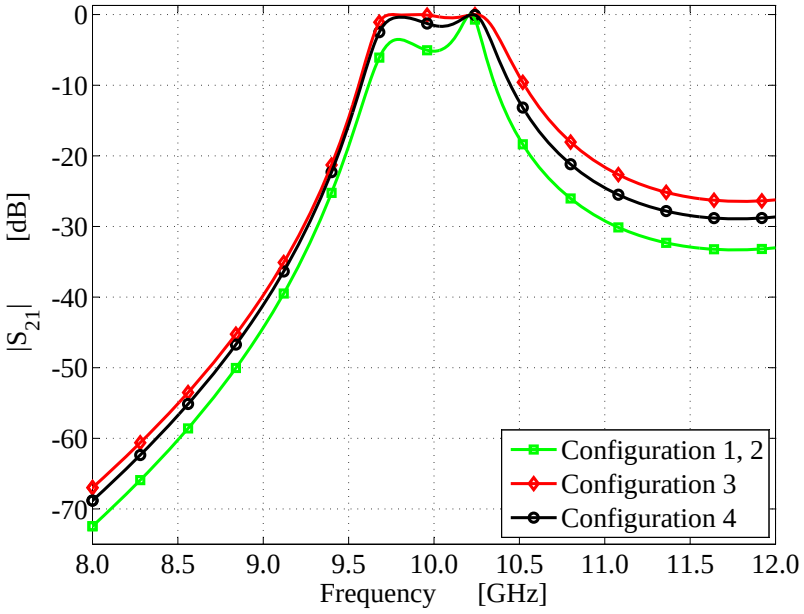


Figure 4.18: $S_{21}$ of rectangular waveguide filter with inductive iris. Dimensions obtained in section 4.5 for a predetermined coupling coefficient of 0.0409.

## 4.6 Conclusion

The coupling mechanisms in coaxial and waveguide media filters were investigated. A method for validating the accuracy of Eigenmode Method and the parameter extraction method from a circuit model for coaxial and waveguide, for the two filter media were presented. For the coaxial media, it was found that the numerical results of the two methods are in agreement over a wide frequency range.

In the waveguide media, a post and an inductive post were used to implement the coupling between the resonators. For the waveguide filter, it was found that the three circuit inverter models each gave different coupling values in comparison to the Eigenmode Method at a single frequency. For the post waveguide structure, *Configuration* 1 and 2 showed the smallest deviation from the Eigenmode Method. In the waveguide structure with an iris to enable coupling, *Configuration* 3 deviated least from the Eigenmode Method.

Dimensions obtained from each of these three circuit inverter models, were then implemented to investigate their effect on a third order waveguide filter. For the post structure, it was found that *Configuration* 4 (Eigenmode Method) gave the best filter response. As for the iris structure, it was found that *Configuration* 3, consisting of the shunt inductance between a set of transmission lines, led to the optimum filter response as set in the specifications (section 4.5).

# Chapter 5

# Conclusion

In this thesis, a lumped-element circuit utilising an admittance inverter was presented for an aperture coupled coaxial cavity. An overview of inverters and their calculation as well as implementation, were shown. Numerical results from the circuit model showed that the given specifications for the diplexer are met.

A combline configuration in coaxial media was utilised to implement the physical implementation of the diplexer. The physical diplexer model was designed by firstly computing the dimensions of the key structures that make up a diplexer. A diplexer with preliminary dimensions was obtained after the key structures were placed in cascade. The tuning process presented by Ness [8], was applied to the physical model in CST. By means of comparison between the circuit model and physical model, parameters were extracted in the circuit model. The physical model was then adjusted accordingly as governed by the value of extracted parameter.

The final diplexer prototype was manufactured and evaluated. The diplexer was first measured by adjusting the frequencies and couplings until a satisfactory magnitude of $S_{11}$ was obtained. The Diplexer was later tuned by MATLAB GUI application programmed to aid in the fine-tuning of the diplexer. The results of the two methods were presented. It was shown that the tuning of the diplexer by the GUI application, was slightly worse. This could be that in the parameter extraction method, the assumption was made that adjusting the dimensions enabling coupling coefficients do not have an effect on the frequency band of the diplexer. The same holds true for the dimensions enabling frequency adjustment having no effect on

the coupling between resonators.

The results from the physical realisation of the diplexer correlates well with the response of the circuit model. It can however be seen from the results that the filter for the lower frequency band, the return loss was slightly less than the specified 20 dB. When the extracted coupling coefficients obtained from the MATLAB GUI application were investigated, it was found that the extracted value for dimension $D_n$, see Fig. 3.25 for the lower frequency band filter, showed the largest deviation from the ideal value of one from all the extracted parameters. From this result, it can be concluded that the distance $D_n$ should be decreased. The coupling between the resonators was slightly larger than anticipated, resulting that the related tuning screws had to be removed. One way to prevent this from happening is to design resonators for slightly smaller coupling coefficients. Consequently, the coupling between the resonators can be increased in the tuning stage by extending the tuning screw. The MATLAB GUI application can be used as a tool to validate the dimensions of the physical model of the diplexer.

The coupling mechanisms in coaxial and waveguide media filters were investigated. A method for validating the accuracy of Eigenmode Method and the parameter extraction method from a circuit model for coaxial and waveguide, for the two filter media was presented. For the coaxial implementation, it was found that the numerical results of the two methods agree well with one another over a wide frequency range.

In the waveguide implementation, a post and an inductive post were used to implement the coupling between the resonators. For the waveguide filter, it was found that the three circuit inverter models each gave different coupling values in comparison to the Eigenmode Method at a single frequency. For the post waveguide structure, *Configuration* 1 and 2 showed the smallest deviation from the Eigenmode Method. In the waveguide structure with an iris to enable coupling, *Configuration* 3 showed the least deviation from the Eigenmode Method.

Dimensions obtained from each of these three circuit inverter models, were then implemented to investigate their effect on a third order waveguide filter. For the

post structure, it was found that *Configuration* 4 (Eigenmode Method) gave the best filter response. As for the iris structure, it was found that *Configuration* 3, consisting of the shunt inductance between a set of transmission lines, led to the optimum filter response as set in the specifications (section 4.5).

Possible future work include the following:

Extending the MATLAB graphical user interface (GUI) application to be able to handle third to tenth order filter topologies. The MATLAB models for different types of filter implementations, such as waveguide, can be added. An option in the GUI can be added as to which configuration of inverter (as discussed in Chapter 4) to use in the implementation of the circuit model.

# Bibliography

[1] Packard, K.S.: The Origin of Waveguides: A Case of Multiple Rediscovery. *IEEE Transactions on Microwave Theory and Techniques*, vol. 32, no. 9, pp. 961–969, 1984.

[2] Rhea, R.W.: *HF Filter Design and Computer Simulation*. 1st edn. Noble Publishing, 1994.

[3] Johnson, D.E.: *Introduction to Filter Theory*. First edition edn. Prentice-Hall, 1976.

[4] Levy, R. and Cohn, S.B.: A History of Microwave Filter Research, Design and Development. *IEEE Transactions on Microwave Theory and Techniques*, vol. 32, no. 9, pp. 1055–1067, 1984.

[5] Boria, V.E. and Gimeno, B.: Waveguide Filters for Satellites. *IEEE Microwave Magazine*, vol. October, no. 10, pp. 60–69, 2007.

[6] Marcuvitz, N.: *Waveguide Handbook*. 1st edn. Short Run Press Ltd., Exeter, 1986.

[7] Matthaei, G.L., Young, L. and Jones, E.M.T.: *Microwave Filters, Impedance-Matching Networks, and Coupling Structures*. 2nd edn. Artech House, 1980.

[8] Ness, J.B.: A Unified Approach to the Design, Measurement, and Tuning of Coupled-Resonator Filters. *IEEE Transactions on Microwave Theory and Techniques*, vol. 46, no. 4, pp. 343–350, 1998.

[9] Van der Walt, P.W.: *Post Graduate Course in Microwave Filter Synthesis*. 2008.

[10] Zverev, A.I.: *Handbook of FILTER SYNTHESIS*. 1st edn. John Wiley and Sons,Inc., 1967.

[11] Atia, A.E., Williams, A.E. and Newcomb, R.W.: Narrow-Band Multiple-Coupled Cavity Synthesis. *IEEE Transactions on Circuits and Systems*, vol. 21, no. 5, pp. 649–655, 1974.

[12] Atia, A.E. and Williams, A.E.: Narrow-Band Waveguide Filters. *IEEE Transactions on Microwave Theory and Technique*, vol. 20, no. 4, pp. 258–265, 1972.

[13] Cameron, R.J.: General Coupling Matrix Synthesis Methods for Chebyshev Filtering Functions. *IEEE Transactions on Microwave Theory and Technique*, vol. 47, no. 4, pp. 433–442, 1999.

[14] Coetzee, N.: *Asymmetrical S-Band Coupled Resonator Filters*. University of Stellenbosch, December 2005.

[15] Macchiarella, G. and Tamiazzo, S.: Novel Approach to the Synthesis of Microwave Diplexers. *IEEE Transactions on Microwave Theory and Techniques*, vol. 54, no. 12, pp. 4281–4290, 2006.

[16] Meyer, P.: *Post Graduate Course in Microwave Networks*. 2007.

[17] Pozar, D.M.: *Microwave Engineering*. 2nd edn. John Wiley and Sons,Inc., 1998.

[18] Hunter, I.: *Theory and Design Of Microwave Filters*. 2nd edn. The Institution of Electrical Engineers, 2001.

[19] Nilsson, J.W. and Riedel, S.A.: *Electric Circuits*. Fifth edition edn. Addison-Wesley Publishing Company, 1996.

[20] D G Swanson, J.: Narrow-Band Microwave Filter Design. *IEEE Microwave Magazine*, vol. October, no. 10, pp. 105–114, 2007.

[21] Budimir, D.: *Generalised Filter Design by Computer Optimization*. First edition edn. Artech House, 1998.

[22] Levy, R.: Theory of Direct-Coupled-Cavity Filters. *IEEE Transactions on Microwave Theory and Techniques*, vol. 15, no. 6, pp. 340–348, 1967.

[23] Ramo, S., Whinnery, J.R. and Duzer, T.V.: *Fields and Waves in Communication Electronics*. Third edition edn. John Wiley & Sons, Inc., 1993.

[24] Boylestad, R.L.: *Introductory Circuit Analysis*. 9th edn. Prentice Hall, 2000.

[25] Su, K.: *Analog Filters*. First edition edn. Chapman & Hall, 1996.

[26] Steyn, W.: *CAD-Based Iris Design Procedure for Multi-Mode Coupled Cavity Devices*. University of Stellenbosch, March 2002.

[27] Sabbagh, M.E., Zaki, K.A., Yao, H. and Yu, M.: Full-Wave Analysis of Coupling Between Combline Resonators and Its Application to Combline Filters with Canonical Configurations. *IEEE Transactions on Microwave Theory and Techniques*, vol. 49, no. 12, pp. 340–348, 2001.

[28] Levy, R.: Theory of Direct-Coupled-Cavity Filters. *IEEE Transactions on Microwave Theory and Techniques*, vol. 15, no. 6, pp. 340–348, 1967.

# Appendix A

# Diplexer Tuning Procedure

In the tuning procedure of the diplexer, the different sections of the diplexer to be tuned will be designated as Sections 1-8. This is graphically illustrated in Fig. A.1.

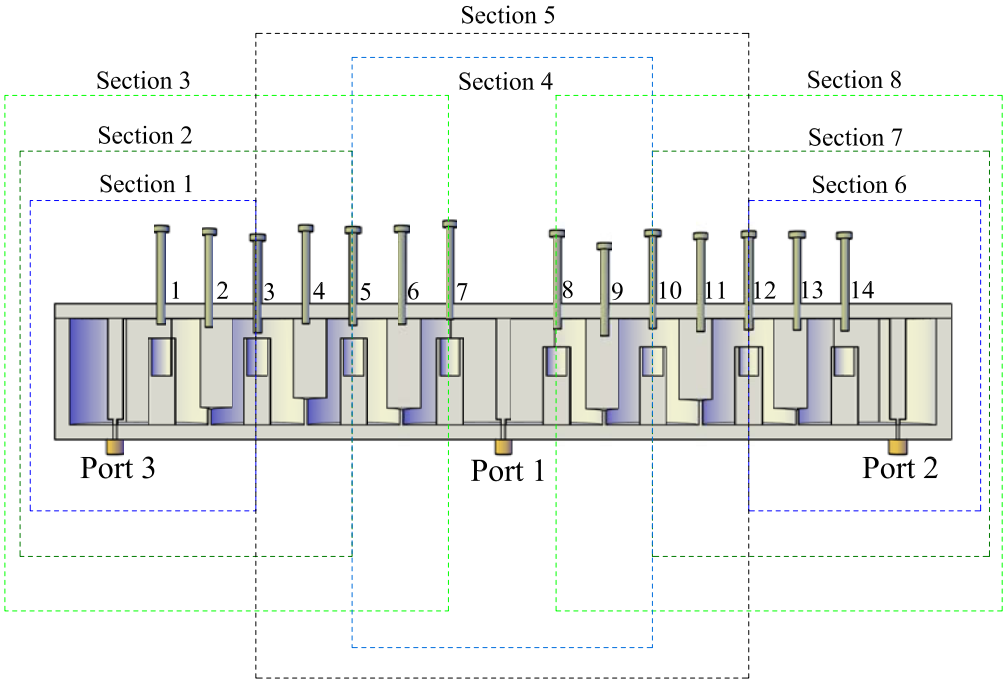


Figure A.1: Definition of the various designated sections as used in the MATLAB application

In the tuning procedure of the diplexer, Sections 4 and 5 are tuned first, followed by Sections 1-3 and lastly Sections 6-8. The tunings screws are numbered

chronologically from left to right of the diplexer. For the tuning of Sections 4-5, connect port one of the *Agilent 8510* VNA to port one (input) of the diplexer. Match port 2 and 3 of the diplexer with matched loads. In the tuning of Sections 1-3, connect port 1 of the VNA to port 3 (output for frequency band 1). Similarly, connect port 1 of the VNA to port 2 (output for frequency band 2). Connect a matched load to port 1 of the diplexer.

## A.1 Tuning of Section 4

The physical tuning of Section 4 is graphically illustrated in Fig.A.2. Extend tuning screws 5 and 10 until it is short-circuited in the inner conductor of the coaxial resonator. Adjust the tuning screws 7 and 8 to enable the tuning of frequencies, $f_{0_{lower}}$ and $f_{0_{upper}}$.

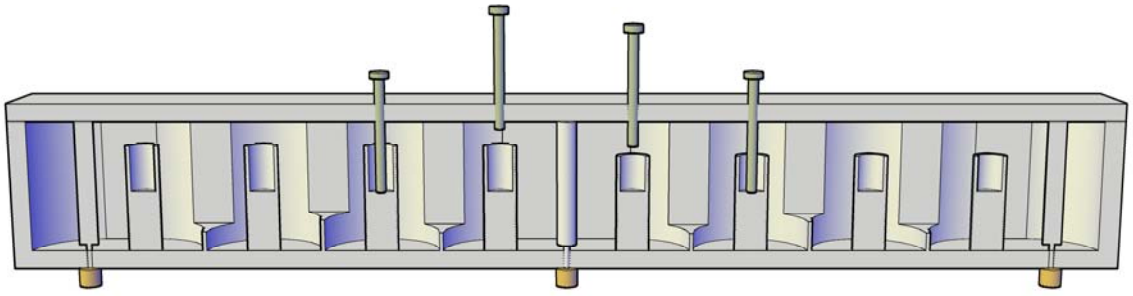

Figure A.2: Tuning of Section 4

Screenshots from the MATLAB application with graphical user interface, are shown in Fig.A.3a and Fig. A.3b. In Fig. A.3a the initial group delay of Section 4, is shown. Note that this screenshot was taken before any tuning was done. In Fig. A.3b, a screenshot is given after the *Bounds* button was pressed. Here the upper and lower boundaries of the multipliers can be adjusted. For the MATLAB application, $k_{12}$ and $F_{01}$ are always referenced closest to the port from which the group delay is computed.

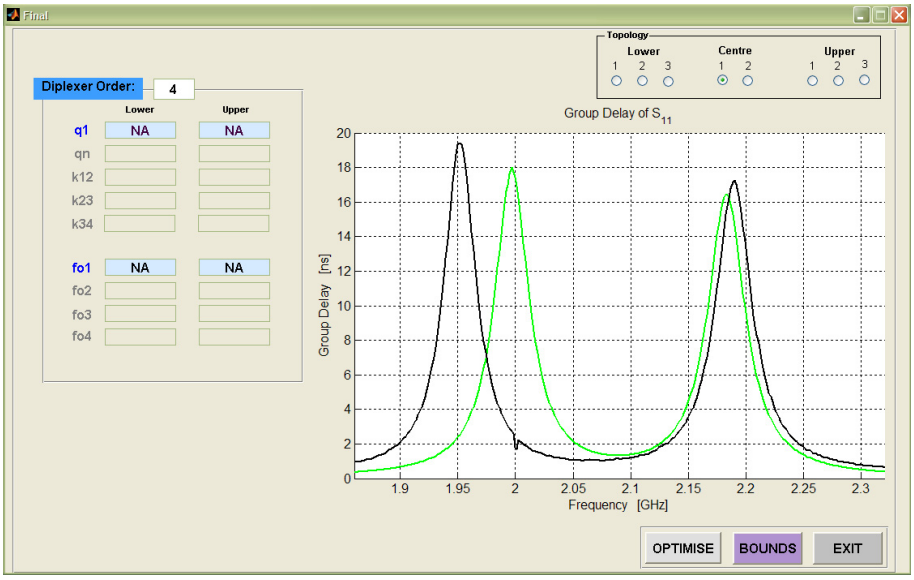


(a) Screenshot of the group delay for Section 4 before any tuning was performed. NA denotes *Not Available*.

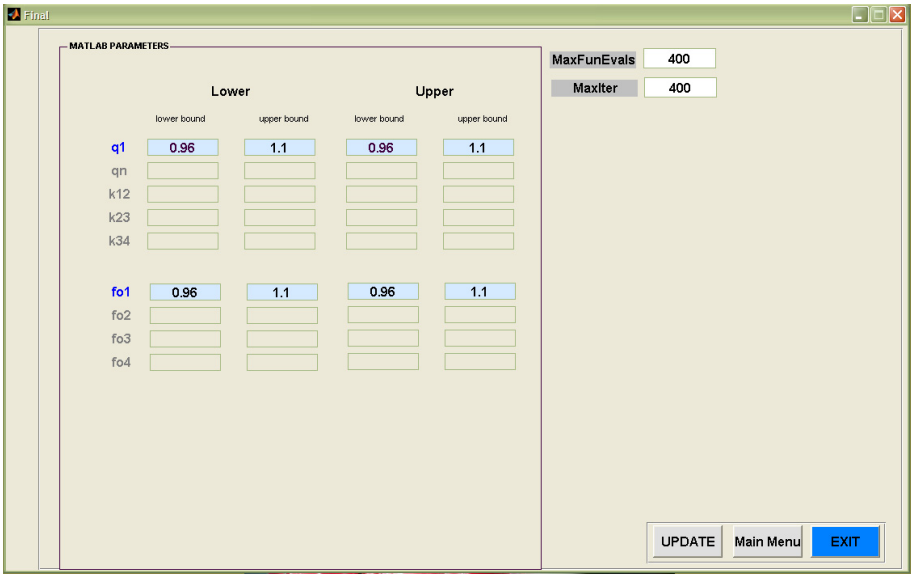


(b) Screenshot of MATLAB application after the *Bounds* button was pressed.

Figure A.3: Screenshots from MATLAB application with graphical user interface to aid in the tuning of the diplexer

A screenshot from the MATLAB application while the curve-fitting is in progress, is shown in Fig. A.4a. The extracted values of the multiplies as determined by MATLAB, are shown in the screenshot of Fig. A.4a.

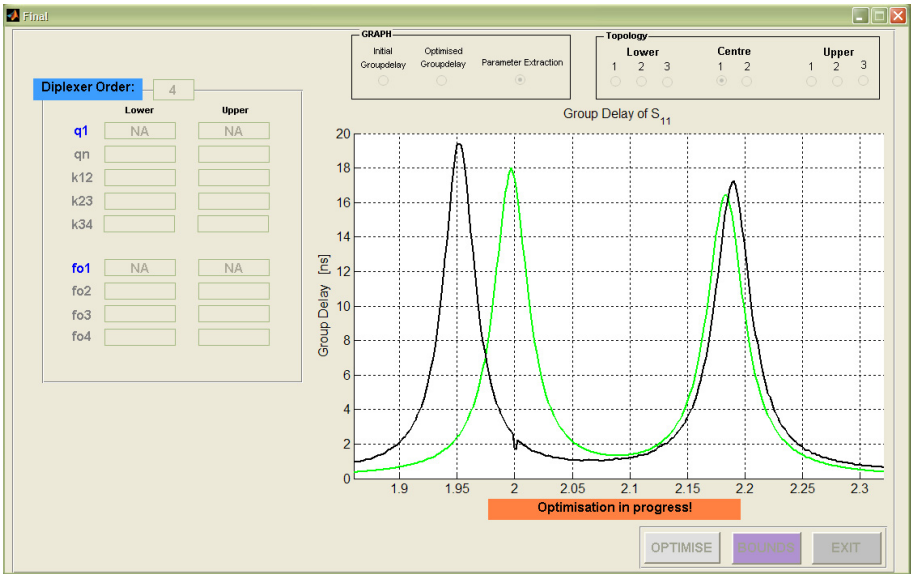


(a) Screenshot of MATLAB application while curve-fitting is in progress

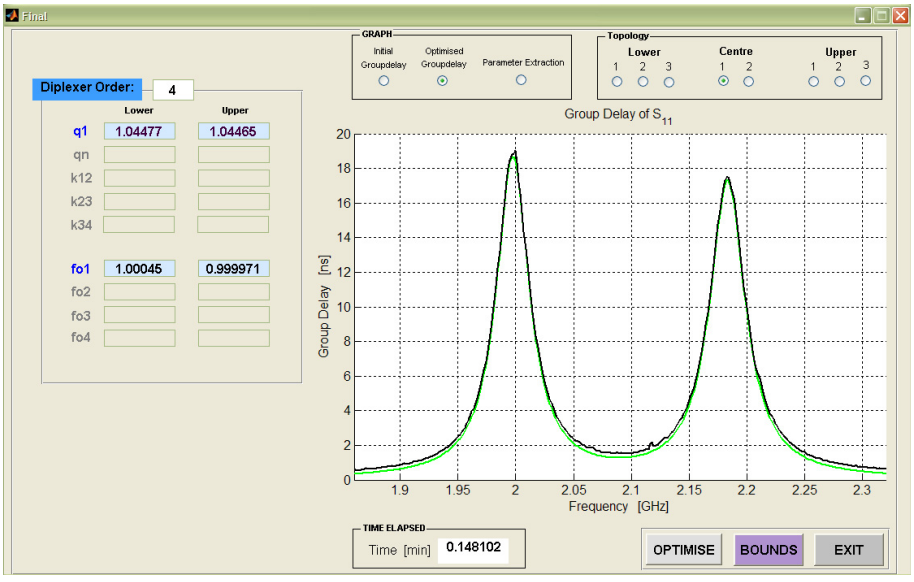


(b) The extracted values of the multipliers after curve-fitting is completed (last iteration for Section 4)

Figure A.4: Screenshots from MATLAB application

The iterative process of adjusting the tuning screws, importing measured s-parameters to MATLAB and extracting the optimised multipliers from the MATLAB application are applied until the deviation of extracted multipliers are within 1% of the ideal value of 1. The final optimised extracted multipliers for k, q and frequency, are given in Table A-I. Note that both the multipliers for $q_{1_{lower}}$ and $q_{1_{upper}}$ deviate the furthest of the multipliers from the ideal value of 1. As a tuning screw would have very little effect on the loaded quality factor, no tuning screws were added to enable their tuning.

Table A-I: Comparison of the final optimised extracted multipliers for k, q and frequency (Section 4) against ideal values equal to one.

| | **Curvefit Extracted Parameters** | **Ideal** |
|---|---|---|
| $\mathbf{q}_{1_{lower}}$ | 1.04477 | 1 |
| $\mathbf{q}_{1_{upper}}$ | 1.04465 | 1 |
| $\mathbf{f}_{01_{lower}}$ | 1.00045 | 1 |
| $\mathbf{f}_{01_{upper}}$ | 0.999971 | 1 |

## A.2 Tuning of Section 5

Next, Section 5, are tuned. Tuning screws 3 and 12 are short-circuited at the inner conductor of coaxial resonator. This is graphically illustrated in Fig. A.5. The tuning screws 6 and 9, to enable $k_{12_{lower}}$ and $k_{12_{upper}}$, are added. The iterative process as mentioned above, are again applied. Final obtained extracted values for the multipliers for Section 5 are given in Table A-II.

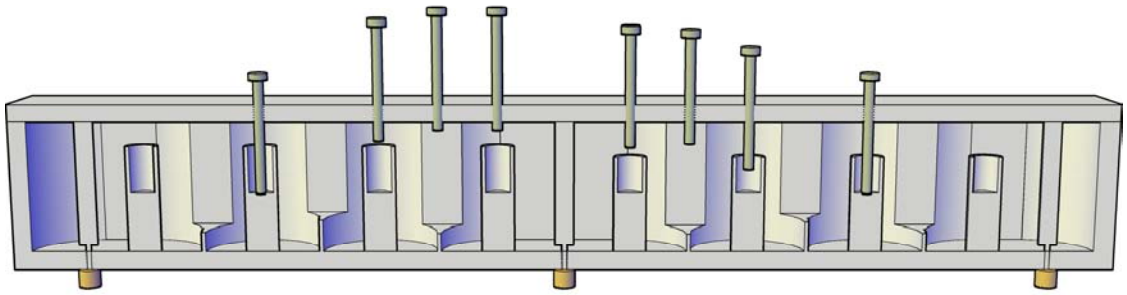

Figure A.5: Diplexer tuning of Section 5

Table A-II: Comparison of the final optimised extracted multipliers for k, q and frequency (Section 5) against ideal values equal to one.

| | **Curvefit** | **Ideal** |
|---|---|---|
| $\mathbf{q}_{1_{lower}}$ | 1.0375 | 1 |
| $\mathbf{q}_{1_{upper}}$ | 1.0499 | 1 |
| $\mathbf{k}_{12_{lower}}$ | 1.03627 | 1 |
| $\mathbf{k}_{12_{upper}}$ | 1.02277 | 1 |
| $\mathbf{f}_{01_{lower}}$ | 1.0005 | 1 |
| $\mathbf{f}_{01_{upper}}$ | 0.999932 | 1 |
| $\mathbf{f}_{02_{lower}}$ | 1.00006 | 1 |
| $\mathbf{f}_{02_{upper}}$ | 1.00061 | 1 |

## A.3 Tuning of Section 1

After the Sections 4-5 are tuned, Section 1-3 will be tuned. The tuning screws as adjusted from the previous tunings are to be left untouched. An additional tuning screws (tuning screw 1 and 3) are added to the diplexer. This is graphically illustrated in Fig. A.6. The tuning screw 3 is short-circuited to the inner conductor of the coaxial resonator. Tuning screw 1 enables the tuning of $f_{04_{lower}}$. Once again the iterative process of tuning by means of the MATLAB application, is performed. The final extracted multipliers for Section 1, are shown in Table A-III.

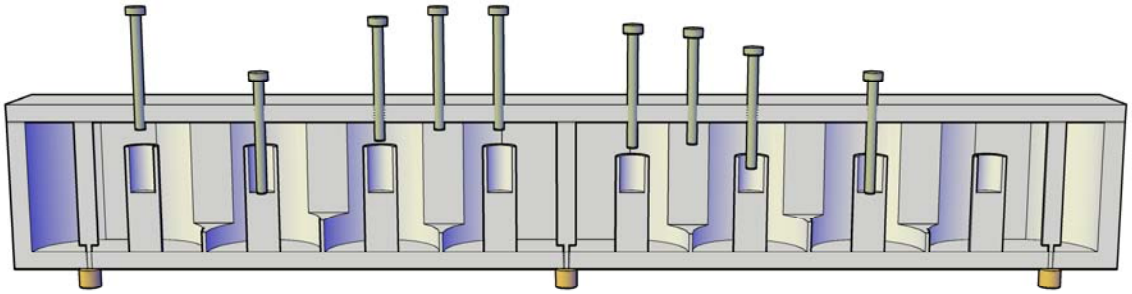

Figure A.6: Diplexer tuning of Section 1

Table A-III: Comparison of the final optimised extracted multipliers for k, q and frequency (Section 1) against ideal values equal to one.

| | **Curvefit** | **Ideal** |
|---|---|---|
| $\mathbf{q}_{1_{lower}}$ | 1.09056 | 1 |
| $\mathbf{f}_{01_{lower}}$ | 0.999501 | 1 |

## A.4 Tuning of Section 2

For the tuning of Section 2, tuning screw 2 is added to enable the tuning of $k_{34_{lower}}$. Tuning screw 1 is adjusted to enable the tuning of $f_{04_{lower}}$, tuning screw 2 to enable $k_{34_{lower}}$ and tuning screw 3 to enable the tuning of $f_{03_{lower}}$. Tuning screw 5 is short-circuited. This is illustrated in Fig. A.7. The final extracted multipliers for Section 2, are shown in Table A-IV.

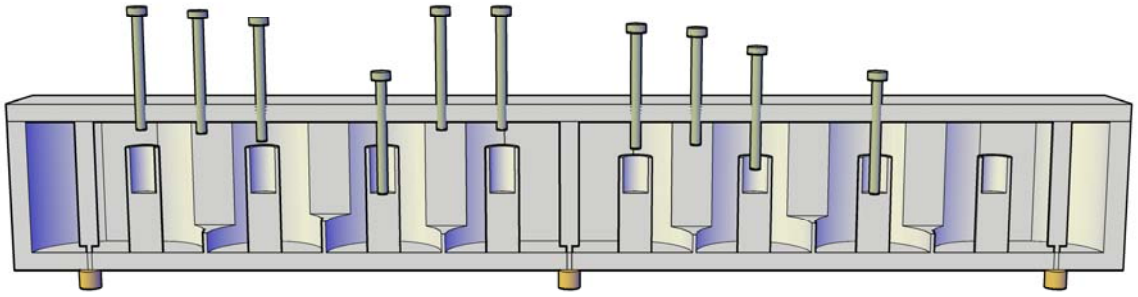

Figure A.7: Diplexer tuning of lower frequency band, part 2

Table A-IV: Comparison of the final optimised extracted multipliers for k, q and frequency (Section 2) against ideal values equal to one.

| | **Curvefit** | **Ideal** |
|---|---|---|
| $\mathbf{q}_{1_{lower}}$ | 1.08 | 1 |
| $\mathbf{k}_{12_{lower}}$ | 1.0266 | 1 |
| $\mathbf{f}_{01_{lower}}$ | 1.00018 | 1 |
| $\mathbf{f}_{02_{lower}}$ | 1.0003 | 1 |

## A.5 Tuning of Section 3

For the tuning of Section 3, tuning screw 4 is added to enable the tuning of $k_{23_{lower}}$. Tuning screw 1 is adjusted to enable the tuning of $f_{04_{lower}}$, tuning screw 2 is kept unadjusted from the previous Section, tuning screw 3 is adjusted to enable the tuning of $f_{03_{lower}}$ and tuning screw 4 is adjusted to enable $k_{23_{lower}}$. Tuning screw 7 is short-circuited. This is illustrated in Fig. A.7. The final extracted multipliers for Section 2, are shown in Table A-IV.

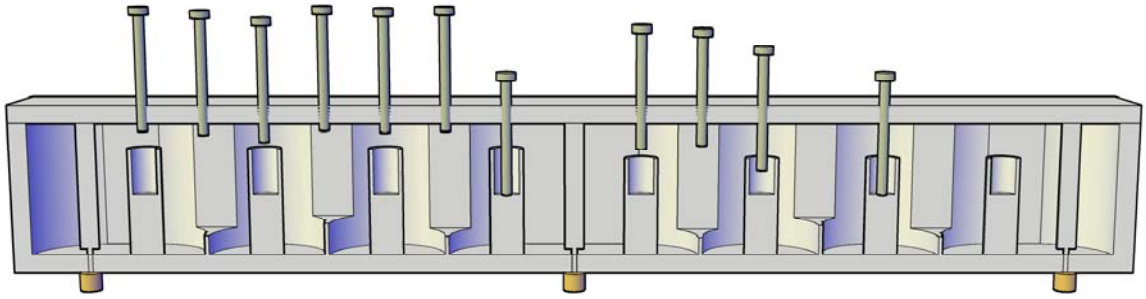

Figure A.8: Diplexer tuning of lower frequency band, part 3

Table A-V: Comparison of the final optimised extracted multipliers for k, q and frequency (Section 3) against ideal values equal to one.

| | **Curvefit** | **Ideal** |
|---|---|---|
| $\mathbf{q}_{1_{lower}}$ | 1.07863 | 1 |
| $\mathbf{k}_{12_{lower}}$ | 1.02584 | 1 |
| $\mathbf{k}_{23_{lower}}$ | 1.04348 | 1 |
| $\mathbf{f}_{01_{lower}}$ | 1.0002 | 1 |
| $\mathbf{f}_{02_{lower}}$ | 0.999259 | 1 |
| $\mathbf{f}_{03_{lower}}$ | 1.00084 | 1 |

## A.6 Tuning of Section 6

The same procedure as applied to Section 1-3, is also applied to Sections 6-8. The tuning of Section 6, is illustrated in Fig. A.9. The final extracted multipliers for Section 6, are shown in Table A-VI.

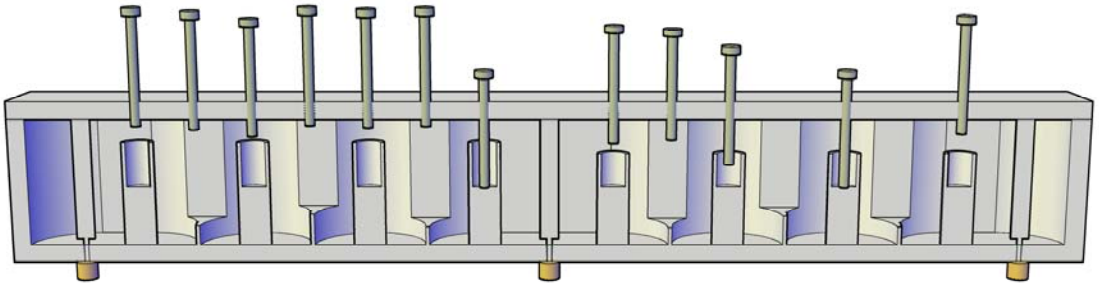

Figure A.9: Diplexer tuning of upper frequency band, part 6

Table A-VI: Comparison of final optimised extracted parameters k, q and frequency against ideal values for Section 6.

| | **Curvefit** | **Ideal** |
|---|---|---|
| $\mathbf{q}_{1_{upper}}$ | 1.03841 | 1 |
| $\mathbf{f}_{01_{upper}}$ | 0.999903 | 1 |

## A.7 Tuning of Section 7

The tuning of Section 7, is illustrated in Fig. A.10. The final extracted multipliers for Section 7, are shown in Table A-VII.

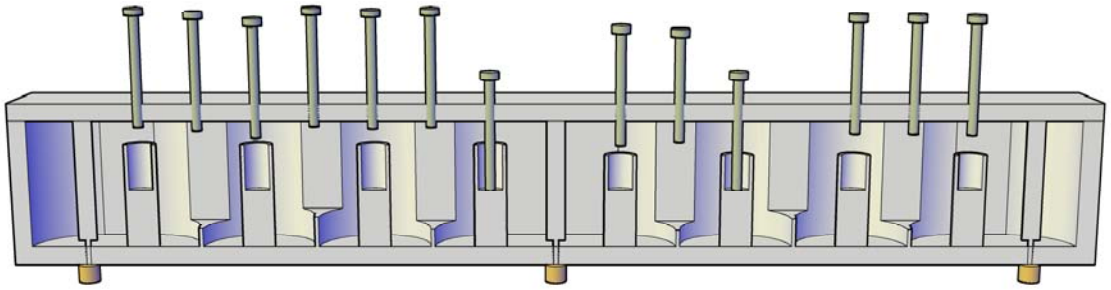

Figure A.10: Diplexer tuning of upper frequency band, part 7

Table A-VII: Comparison of final optimised extracted parameters k, q and frequency against ideal values for Section 7.

| | **Curvefit** | **Ideal** |
|---|---|---|
| $\mathbf{q}_{1_{upper}}$ | 1.03864 | 1 |
| $\mathbf{k}_{12_{upper}}$ | 1.00194 | 1 |
| $\mathbf{f}_{01_{upper}}$ | 0.999929 | 1 |
| $\mathbf{f}_{02_{upper}}$ | 1.00008 | 1 |

## A.8 Tuning of Section 8

The tuning of Section 8, is illustrated in Fig. A.11. The final extracted multipliers for Section 6, are shown in Table A-VIII.

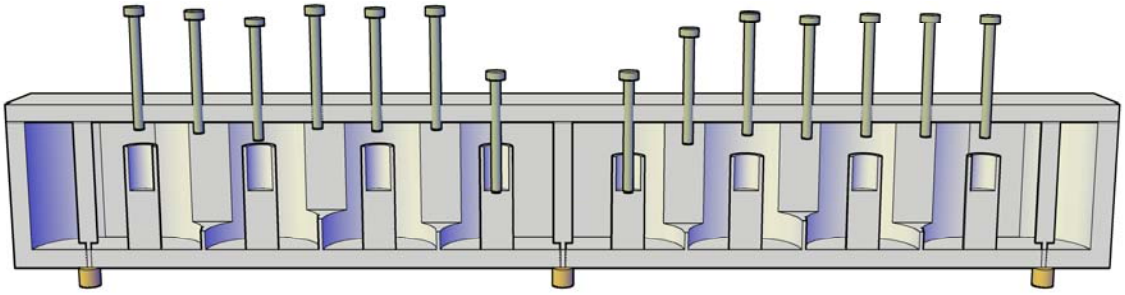

Figure A.11: Diplexer tuning of upper frequency band, part 8

Table A-VIII: Comparison of final optimised extracted parameters k, q and frequency against ideal values for Section 8.

| | **Curvefit** | **Ideal** |
|---|---|---|
| $\mathbf{q}_{1_{upper}}$ | 1.03 | 1 |
| $\mathbf{k}_{12_{upper}}$ | 1.00848 | 1 |
| $\mathbf{k}_{23_{upper}}$ | 1.03 | 1 |
| $\mathbf{f}_{01_{upper}}$ | 0.99973 | 1 |
| $\mathbf{f}_{02_{upper}}$ | 0.999609 | 1 |
| $\mathbf{f}_{03_{upper}}$ | 1.00013 | 1 |

## A.9 Final Tuned Diplexer

The final tuned diplexer is shown in Fig. A.12.

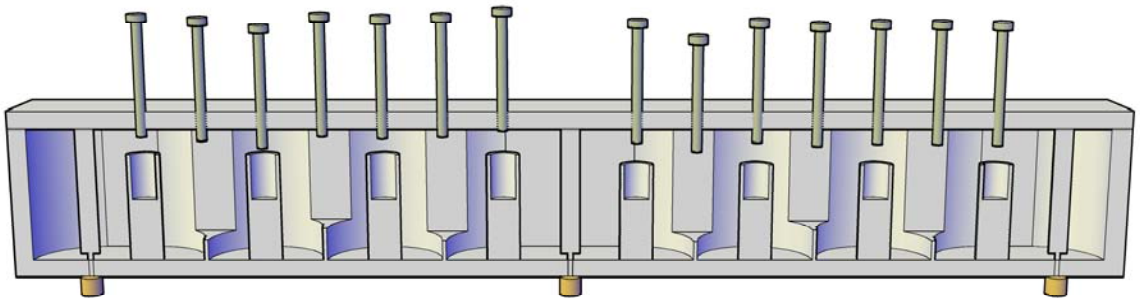

Figure A.12: Final tuning of diplexer

# Appendix B

# Derivation of Equations for Configuration 3

The transfer matrix of an ideal impedance inverter is given by Eq. B.1.

$$\begin{bmatrix} A & B \\ C & D \end{bmatrix} = \begin{bmatrix} 0 & \pm \jmath K \\ \pm \frac{\jmath}{K} & 0 \end{bmatrix} \tag{B.1}$$

For the sake of convenience, the inverter model used for *Configuration* 3, is shown in Fig. B.1. The inverter model consist of a shunt inductance $\jmath X$ at the centre of a short length of transmission line of electrical length $-\theta$ [28].

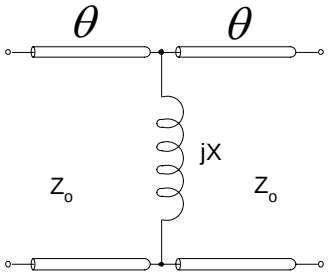


Figure B.1: Inverter model (*Configuration* 3)

The transfer function of *Configuration* 3 is given by Eq. B.2 [28].

$$\begin{bmatrix} A & B \\ C & D \end{bmatrix} = \begin{bmatrix} \cos\theta - \frac{\sin\theta}{\frac{2X}{Z_o}} & -\jmath\left(\sin\theta + \frac{\cos\theta - 1}{\frac{2X}{Z_o}}\right) Z_o \\ \frac{-\jmath}{Z_o}\left(\sin\theta + \frac{\cos\theta + 1}{\frac{2X}{Z_o}}\right) & \cos\theta - \frac{\sin\theta}{\frac{2X}{Z_o}} \end{bmatrix} \tag{B.2}$$

The condition for the inverter model (*Configuration 3*) to represent the ideal impedance inverter as given in Eq. B.1 is that of A = 0. Hence

$$\theta = \tan^{-1}\frac{2X}{Z_o} \tag{B.3}$$

Similarly, B = $\pm\ \jmath$ K and C = $\pm\ \frac{\jmath}{K}$. Theses relations are shown in Eq. B.4 and Eq. B.5.

$$B = -\jmath\left(\sin\theta + \frac{\cos\theta - 1}{\frac{2X}{Z_o}}\right) Z_o \tag{B.4}$$

$$C = -\frac{\jmath}{Z_o}\left(\sin\theta + \frac{\cos\theta + 1}{\frac{2X}{Z_o}}\right) \tag{B.5}$$

The following trigonometric identities are given in Eq. B.6.

$$\begin{aligned} \cos^2 A &= \frac{1}{2}\left[1 + \cos 2A\right] \\ \sin^2 A &= \frac{1}{2}\left[1 - \cos 2A\right] \end{aligned} \tag{B.6}$$

Using above trigonometric identities, Eq. B.4 and Eq. B.5 can be written as in Eq. B.7 and Eq. B.8.

$$\pm \jmath K = -\jmath Z_o \left[\sin\phi - \frac{Z_o}{X}\left(\sin^2\frac{\theta}{2}\right)\right] \tag{B.7}$$

$$\pm \frac{\jmath}{K} = -\frac{\jmath}{Z_o}\left[\sin\phi + \frac{Z_o}{X}\left(\cos^2\frac{\theta}{2}\right)\right] \tag{B.8}$$

By simplification of Eq. B.7 and Eq. B.8, Eq. B.9 and Eq. B.10 are obtained.

$$\mp \frac{K}{Z_o} = \sin\theta - \frac{Z_o}{X}\sin^2\frac{\theta}{2} \tag{B.9}$$

$$\mp \frac{Z_o}{K} = \sin\theta + \frac{Z_o}{X}\cos^2\frac{\theta}{2} \tag{B.10}$$

Subtracting Eq. B.10 from Eq. B.9 yields Eq. B.11.

$$\begin{aligned} \mp \frac{K}{Z_o} \pm \frac{Z_o}{K} &= \frac{Z_o}{X}\left(\cos^2\frac{\theta}{2} + \sin^2\frac{\theta}{2}\right) \\ \frac{X}{Z_o} &= \frac{Z_o}{X} \\ &= \frac{\frac{K}{Z_o}}{1-\left(\frac{K}{Z_o}\right)^2} \end{aligned} \tag{B.11}$$

The following trigonometric identities are given in Eq. B.12.

$$\begin{aligned}\tan(2\phi) &= \frac{\tan\phi + \tan\phi}{1-\tan^2\phi} \\ &= 2\frac{\tan\phi}{1-\tan^2\phi} \\ \tan\phi &= \frac{2\tan\frac{\phi}{2}}{1-\tan^2\frac{\phi}{2}}\end{aligned}$$

By applying the trigonometric identities as given in Eq. B.12 to Eq. B.11, yields Eq. B.12.

$$\begin{aligned}\frac{1}{2}\tan\theta &= \frac{\frac{K}{Z_o}}{1-\left(\frac{K}{Z_o}\right)^2} \\ \tan\theta &= \frac{\frac{2K}{Z_o}}{1-\left(\frac{K}{Z_o}\right)^2} \\ \frac{2\tan\frac{\theta}{2}}{1-\tan^2\frac{\theta}{2}} &= \frac{2\frac{K}{Z_o}}{1-\left(\frac{K}{Z_o}\right)^2} \\ \tan\frac{\theta}{2} &= \frac{K}{Z_o} \\ K &= Z_o\tan\frac{\theta}{2}\end{aligned} \tag{B.12}$$